



<https://theses.gla.ac.uk/>

Theses Digitisation:

<https://www.gla.ac.uk/myglasgow/research/enlighten/theses/digitisation/>

This is a digitised version of the original print thesis.

Copyright and moral rights for this work are retained by the author

A copy can be downloaded for personal non-commercial research or study, without prior permission or charge

This work cannot be reproduced or quoted extensively from without first obtaining permission in writing from the author

The content must not be changed in any way or sold commercially in any format or medium without the formal permission of the author

When referring to this work, full bibliographic details including the author, title, awarding institution and date of the thesis must be given

Enlighten: Theses

<https://theses.gla.ac.uk/>
research-enlighten@glasgow.ac.uk

LOW-DIMENSIONAL CHARACTERIZATION AND
CONTROL OF NON-LINEAR WAKE FLOWS

By

Eric A. Gillies B.Eng.

DISSERTATION

SUBMITTED TO THE FACULTY OF ENGINEERING

UNIVERSITY OF GLASGOW

FOR THE DEGREE OF

DOCTOR OF PHILOSOPHY

June 1995

© Copyright 1995 by Eric A. Gillies

ProQuest Number: 10390507

All rights reserved

INFORMATION TO ALL USERS

The quality of this reproduction is dependent upon the quality of the copy submitted.

In the unlikely event that the author did not send a complete manuscript and there are missing pages, these will be noted. Also, if material had to be removed, a note will indicate the deletion.



ProQuest 10390507

Published by ProQuest LLC (2017). Copyright of the Dissertation is held by the Author.

All rights reserved.

This work is protected against unauthorized copying under Title 17, United States Code
Microform Edition © ProQuest LLC.

ProQuest LLC.
789 East Eisenhower Parkway
P.O. Box 1346
Ann Arbor, MI 48106 – 1346

Thesis
10177
Copy 2



Abstract

Many wake flows exhibit self-excited flow oscillations which are sustained by the flow itself and are not caused by amplification of external noise. The archetypal example of a self-excited wake flow is the low Reynolds number flow past a circular cylinder. This flow exhibits self-sustained periodic vortex shedding above a critical Reynolds number. A linear stability analysis of wake flows of this kind shows the presence of a significant region of local absolute instability which admits a temporally growing global mode of oscillation. In general, wake flows may possess multiple global modes, the most unstable of which is the observed oscillation of the wake. Active, closed-loop control of such wake flows is of interest within the present study. In single sensor control schemes, flow oscillations may be suppressed at the sensor location but are in general exacerbated elsewhere by the destabilization of further global modes. For complete suppression of the flow oscillations resulting from global flow instability, all of the possible global modes must be attenuated. In general, complete suppression of all possible global modes requires the use of multiple sensors within the control scheme. As the response of the flow to external control forcing is non-linear, then the most efficient control strategy is also non-linear.

The present work describes a general control strategy for non-linear self-excited wakes. Representation of the self-excited flow field by a finite set of characteristic features, which correspond to the large scale wake components, allows for the efficient design of a closed-loop control algorithm. Experimentally, wake flows are seen to be dominated by a finite number of large scale spatial structures and low-dimensional

mathematical models of such flows are often adequate. Characterization of the large scale spatial structures of a wake flow can be performed with proper orthogonal decomposition, which selects an orthogonal set of spatial modes that are maximized in terms of retained energy. The low energy modes are neglected and the resulting finite orthogonal basis is used as a finite, low-dimensional representation of the wake flow field. A finite representation of the flow field, afforded by the modes, circumvents the need for a complex control algorithm involving a large number of spatially distributed flow field measurements. An appropriate control strategy is then to provide an external control input to the wake such that the future state of the wake corresponds to a desired set of mode amplitudes. Empirical prediction of the response of the wake to external control is furnished by a non-linear neural network. Empirical modelling of the wake response avoids the need for explicit representation of the control-wake interaction. Additionally, the neural network structure of the control-wake interaction model allows for the design of a robust non-linear control algorithm. Furthermore, rearrangement of the mode extraction process into a neural network format provides continuity within the modelling and control scheme. Successful control of a simplified wake flow, which models some of the stability features and spatial complexity of a cylinder wake flow, illustrates the utility of the control scheme.

Acknowledgements

The author would like to thank Dr John Anderson for his valuable supervision and encouragement during the period of research and would also like to acknowledge Dr Richard Green for discussions about the bluff body wake problem. The author would also like to express thanks to Mr Eric Gillies BSc BA who proof read the manuscript.

The author is indebted to family and friends who gave encouragement throughout the period of research. The work was funded on a grant from the Science and Engineering Research Council.

Declaration

No portion of the work in this thesis has been submitted in support of an application for another degree or qualification of this or any other institute of learning. The work is original in content except where indicated.

Contents

| | |
|--|-----------|
| Abstract | ii |
| Acknowledgements | iv |
| Declaration | v |
| 1 Introduction | 1 |
| 1.1 Self-excited Oscillations in Fluid Wakes | 1 |
| 1.2 Response of Self-excited Wakes to External Control | 8 |
| 1.3 Low-Dimensional Control of Self-excited Fluid Wakes | 14 |
| 1.3.1 The Dynamics of Large Scale Spatial Structures in Dissipative Fluid Flows | 18 |
| 1.3.2 Control of Large Scale Spatial Structures with Neural Networks | 23 |
| 1.4 Outline of the Dissertation | 24 |
| 2 Characterization of Dissipative Fluid Flows | 27 |
| 2.1 Introduction | 27 |
| 2.2 Geometric Characteristics of the Navier- Stokes Equations | 28 |
| 2.3 The Method of Proper Orthogonal Decomposition | 33 |

| | | |
|----------|---|-----------|
| 2.3.1 | The Method of Snapshots | 35 |
| 2.3.2 | Reconstruction of the Velocity Field | 37 |
| 2.4 | Low-dimensional Description of Non-stationary Flow | 38 |
| 2.5 | Sub-optimal Decomposition of Non-stationary Flow | 44 |
| 2.6 | Utility of the POD Modes | 51 |
| 2.7 | Summary | 53 |
| 3 | Control of Large Scale Wake Structures | 56 |
| 3.1 | Introduction | 56 |
| 3.2 | Prediction of the Flow Dynamics | 57 |
| 3.2.1 | Galerkin Methods | 57 |
| 3.2.2 | Empirical Modelling of the Flow Dynamics | 60 |
| 3.3 | Neural Network Emulation of the Flow Dynamics | 61 |
| 3.4 | Neural Network Non-linear Control | 71 |
| 3.5 | Neural Estimation of the POD modes | 74 |
| 3.6 | Summary | 80 |
| 4 | A Prototype Wake Control Problem | 82 |
| 4.1 | Introduction | 82 |
| 4.2 | Numerical Solution of the Laminar Cylinder Wake | 84 |
| 4.3 | Simulation of a Forced Cylinder Flow | 95 |
| 4.3.1 | Generation of a Prototype Cylinder Flow | 95 |
| 4.3.2 | Validity of the Prototype Flow Model | 103 |
| 4.4 | Control of the Prototype Cylinder Wake | 125 |
| 4.4.1 | Controller Mode Extraction | 125 |

| | | |
|----------|---|------------|
| 4.4.2 | Non-linear Prediction of the Prototype Flow Response | 131 |
| 4.4.3 | Non-linear Adaptive Control of the Prototype Flow | 139 |
| 4.5 | Summary | 141 |
| 5 | Conclusions and Future Work | 149 |
| 5.1 | Conclusions | 149 |
| 5.2 | Recommendations for Future Work | 152 |
| A | Identification of the Prototype Wake Model | 154 |
| A.1 | Galerkin Approximation of the Navier-Stokes Equations | 154 |
| A.2 | Least Squares Identification of the Reduced Order Model | 157 |
| | Bibliography | 163 |

List of Figures

| | | |
|-----|---|----|
| 1.1 | Linear Decay of Oscillations in a Sub-critical Cylinder Wake | 4 |
| 1.2 | Sketch of the Cylinder Wake | 5 |
| 1.3 | Strouhal number versus Reynolds number for Cylinder Wakes | 6 |
| 1.4 | Temporal Growth of Global Mode: Landau Equation | 7 |
| 1.5 | Region of Lock-in | 12 |
| 1.6 | Gain Window Observed in Cylinder Flow | 15 |
| 1.7 | Attempted Single Sensor Control of Multiple Global Modes of Circular Cylinder | 16 |
| | | |
| 2.1 | Unforced and forced phase portraits of the B-S system | 41 |
| 2.2 | Twisting and folding of B-S attractor by periodic forcing | 42 |
| 2.3 | Stretching and bundling of trajectories by periodic forcing | 43 |
| 2.4 | Superiority of concatenation approach | 48 |
| 2.5 | Eigenset similarity with variation in the number of considered time-series | 55 |
| | | |
| 3.1 | Sketch of the Galerkin Projection | 59 |
| 3.2 | Structure of Neuron Model | 62 |
| 3.3 | The Multi-layer Perceptron | 64 |
| 3.4 | Neural Emulator: One-Step Predictor | 68 |
| 3.5 | Error Surface for Single Non-linear Neuron | 70 |
| 3.6 | Neural Control Scheme | 73 |

| | | |
|------|---|-----|
| 3.7 | Mode Extraction Network | 78 |
| 3.8 | Non-linear Control of Fluid Flow | 80 |
| 4.1 | Problem domain | 84 |
| 4.2 | Computational grid | 87 |
| 4.3 | Close-up of computational grid around cylinder | 87 |
| 4.4 | Transient velocity during growth of oscillations | 88 |
| 4.5 | Horizontal velocity vectors during shedding | 89 |
| 4.6 | Vertical velocity vectors during shedding | 89 |
| 4.7 | Velocity limit cycle during shedding | 90 |
| 4.8 | Power spectral density of velocity signal | 91 |
| 4.9 | Typical flow velocity vectors | 93 |
| 4.10 | Typical flow streamlines | 93 |
| 4.11 | Artificial dissipation of wake: streamlines | 94 |
| 4.12 | Eigenvalues of the POD modes | 99 |
| 4.13 | Eigenvectors of the reduced correlation matrix, used to construct first four POD modes | 100 |
| 4.14 | Spatial structure of the first four POD modes of the cylinder wake: shown are contours of velocity magnitude | 101 |
| 4.15 | Contours of force contribution | 104 |
| 4.16 | Temporal growth of unforced prototype modes | 106 |
| 4.17 | Temporal growth of unforced prototype velocities at point a and point b | 107 |
| 4.18 | Simulated flow fields during growth of oscillations | 108 |
| 4.19 | Comparison between CFD flow and prototype model: mode ampli- tudes on limit cycle | 110 |
| 4.20 | Comparison between CFD flow and prototype model: projections of limit cycle | 111 |

| | | |
|------|--|-----|
| 4.21 | Comparison between CFD flow and prototype model: projections of limit cycle | 112 |
| 4.22 | Comparison between CFD flow and prototype model: velocity at point a | 113 |
| 4.23 | Comparison between CFD flow and prototype model: velocity at point b | 114 |
| 4.24 | Typical section of prototype velocity field error from model | 115 |
| 4.25 | Frequency content of limit cycle prototype model oscillations | 115 |
| 4.26 | Example of prototype forcing entrainment region | 119 |
| 4.27 | Experimental forcing entrainment region | 119 |
| 4.28 | Time history and frequency content of velocity signal in prototype model wake during lock-in. Dashed line is natural shedding frequency. | 120 |
| 4.29 | Prototype phase portraits of velocity signals during lock-in | 121 |
| 4.30 | Time history and frequency content of velocity signal in prototype model wake during non-lock-in oscillations | 122 |
| 4.31 | Prototype phase portraits of velocity signals during non lock-in | 123 |
| 4.32 | Examples of different spatial structure that occur periodically in beating oscillations of the prototype | 124 |
| 4.33 | Typical noise corrupted velocity field | 126 |
| 4.34 | First controller mode: contour of velocity magnitudes | 128 |
| 4.35 | First controller mode: surface of velocity magnitudes | 129 |
| 4.36 | Second controller mode: contour of velocity magnitudes | 129 |
| 4.37 | Second controller mode: surface of velocity magnitudes | 130 |
| 4.38 | Time history of controller mode amplitudes for low, medium and high noise levels | 133 |
| 4.39 | Points a,b and c used for single point measurements of the prototype flow | 133 |

| | | |
|------|--|-----|
| 4.40 | Comparison between single and mode amplitude measurements of the prototype wake | 134 |
| 4.41 | Control input for emulator training | 135 |
| 4.42 | Neural emulator training error and adaptive learning rate | 136 |
| 4.43 | Neural emulator prediction of first controller mode amplitude response | 137 |
| 4.44 | Neural emulator prediction of second controller mode amplitude response | 138 |
| 4.45 | Prototype flow response during a control run: control switched on after six limit cycle oscillations | 142 |
| 4.46 | Control input during a control run: control switched on after six limit cycle oscillations | 143 |
| 4.47 | Control system error during a control run: control switched on after six limit cycle oscillations | 144 |
| 4.48 | Close-up of non-linear controller history | 145 |
| 4.49 | Phase portraits of prototype flow during a control run | 146 |
| 4.50 | Velocity vectors of prototype flow after successful suppression of oscillations | 147 |
| 4.51 | Linear adaptive control strategy | 148 |

Chapter 1

Introduction

1.1 Self-excited Oscillations in Fluid Wakes

Many wake flows exhibit flow oscillations which persist purely as a result of flow instability and which are not due to the influence of external forcing, noise, or internal pressure feedback. This class of fluid flows exhibits *self-excited oscillations*. Whether or not a particular wake flow can exhibit self-excited oscillations is dependent on the nature of the flow instability. Instability of a fluid flow is termed *absolute* if any arbitrary disturbance grows exponentially in time at a fixed streamwise location and therefore contaminates the flow both upstream and downstream of the source; whereas the instability is termed *convective* if disturbances are selectively amplified but ultimately swept away from their source, leaving the flow undisturbed after the source of excitation is removed [1].

The type of flow instability is usually ascertained within linear theory where the stability, with respect to infinitesimal perturbations, of a fictitious parallel wake flow is considered. The fictitious parallel wake has a velocity profile independent of streamwise location but equal to the local mean velocity profile of the actual non-parallel wake flow at a fixed, but arbitrary, streamwise location [2][1]. The stability characteristics of the linearized wake are representative of the stability features of

the actual wake as long as the mean velocity profile of the actual non-parallel wake varies only slowly in the streamwise direction [3][4]. Linear global modes are time-harmonic solutions of the linearized flow equations around a non-parallel basic flow and are of the form,

$$\hat{v}(x, y) \exp(-i\omega_G t) \quad (1.1)$$

where ω_G is the complex global frequency. The two types of instability are distinguished by the temporal growth rate, $\text{Im}(\omega_G)$, of the global mode which dominates the long term response of the flow at the disturbance location[5]. The flow is locally convectively unstable if $\text{Im}(\omega_G) < 0$ and locally absolutely unstable if $\text{Im}(\omega_G) > 0$. Flows of the absolutely unstable class therefore admit a temporally growing global mode, which grows exponentially after an initial disturbance, whereas the global modes of a convectively unstable flow are damped and are only amplified by continual external perturbation [4].

Convectively unstable flows, such as laminar boundary layers, linearly amplify external disturbances of a certain amplitude and frequency content but do not, in general, admit self-excited oscillations. This type of fluid flow is *globally stable*, with respect to infinitesimal perturbations, because the flow returns to its original undisturbed state in the absence or cessation of external perturbation. Although convectively unstable flows are globally stable, global flow oscillations can exist in a convectively unstable flow if internal pressure feedback is present: for example, in the flow over a cavity which is locally convectively unstable everywhere, self-excited oscillations can exist due to the intrinsic feedback of pressure waves reflected from the downstream edge of the cavity.

Global instability is a necessary condition for self-excited oscillations in the absence of feedback. Local *absolute* instability over a finite streamwise interval is a necessary condition for global instability [6]. The flow oscillations resulting from absolute instability continue irrespective of the presence of further infinitesimal external perturbation [1]. Kármán vortex shedding is the typical non-linear saturated

mode of oscillations in self-excited wake flows: the archetypal flow that exhibits Kármán vortex shedding, resulting from absolute instability, is the low Reynolds number flow past a circular cylinder [2].

Below some critical value of a flow parameter, such as the Reynolds number, a wake flow typically displays linear behaviour resulting from convective instability. As the relevant flow parameter is raised, the flow may become absolutely unstable over a small spatial region, but remain globally stable. External perturbation of the flow results in oscillations of the flow, favouring the, as yet, damped global modes. However, the oscillations decay linearly and perturbations are swept downstream after the cessation of external forcing. An example of linear behaviour of a wake flow is shown by the low Reynolds number flow past a circular cylinder. Below a critical Reynolds number ($Re_c \simeq 47$) the flow past a circular cylinder is dominated by two large vortices of opposite rotation situated immediately behind the cylinder. These vortices grow in strength and elongate in the flow direction as the Reynolds number is raised; however, the flow is steady below the critical Reynolds number [2]. Any perturbation of the flow below the critical Reynolds number is swept downstream from its source and does not affect the future, long-term, behaviour of the wake. Perturbation of the sub-critical wake can cause the wake to oscillate: the vortices behind the cylinder are alternately shed into the wake and form a 'vortex street'. However, no matter what the amplitude or frequency content of the external perturbation, the wake oscillations linearly decay and the flow resumes its steady state when the external perturbation is removed [7]. The linear decay of flow oscillations resulting from external excitation of a subcritical cylinder wake (at $Re = 46.8$) is shown in figure 1.1.

As the relevant flow parameter in the wake (Reynolds number in the cylinder case) is raised above the critical value the region of absolute instability increases and there is a stable (supercritical) Hopf bifurcation from a steady to a periodic state [3][1]. Typically, this bifurcation is observed by spontaneous, self-excited,

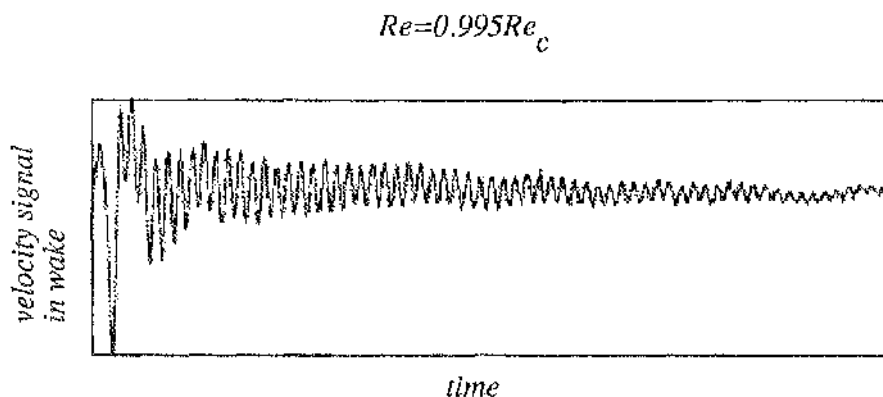


(figure adapted from [7])

Figure 1.1: Linear Decay of Oscillations in a Sub-critical Cylinder Wake

asymmetric vortex shedding forming a Kármán vortex street in the wake [2]. This bifurcation is exemplified by the periodic vortex shedding behind a circular cylinder at Reynolds numbers above $Re_c \simeq 47$. The qualitative features and dynamics of the cylinder wake are typical of self-excited flows in general [5] [8] (for example, a similar bifurcation to flow oscillations is seen at a critical velocity ratio in a mixing layer [1]).

Wake flows exhibiting self-excited oscillations are often dominated by large scale spatial structures: in the cylinder example, the mean flow during shedding consists of two large vortices behind the cylinder (which are slightly smaller than those prior to shedding) and the fluctuating wake is formed by the downstream movement of the large vortices that are alternately shed by the cylinder. The resulting laminar, periodic vortex street persists up to a Reynolds number of around 250, beyond which aperiodicity, three-dimensionality and turbulence (with its associated smaller scales) may be observed. For the cylinder, the period of oscillations is characterized by the Strouhal number, $St = \frac{vD}{V}$, which is a continuous function of the Reynolds number [2]. The spatial structure of the Kármán vortex street is, very roughly, characterized by a ratio of the cross-stream distance, h , between the vortex cores

to the downstream distance, l . The natural, stable arrangement of a vortex street has $\frac{h}{l} = 0.281$ [9]. Figure 1.2 shows a sketch of a cylinder wake during vortex shedding [9]. The dependence of Strouhal number on Reynolds number is shown in figure 1.3 [2].

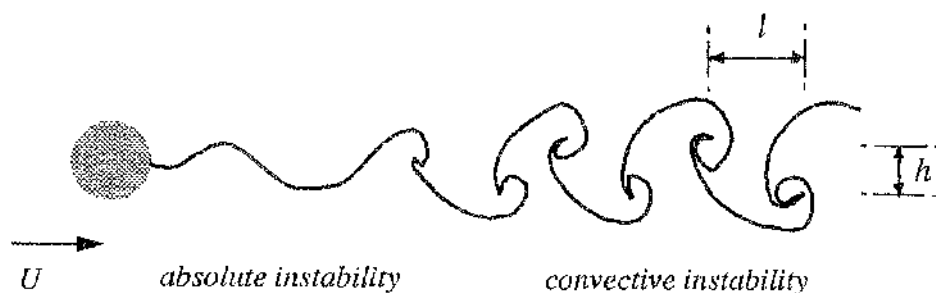


Figure 1.2: Sketch of the Cylinder Wake

Examination of circular cylinder wakes after an impulsive change in the Reynolds number from a subcritical to a supercritical value shows a typical growth of oscillations seen in globally unstable wake flows. The wake oscillations grow exponentially in the initial, linear stages and eventually form a non-linear limit cycle [1]. The characteristic amplitude, r , and frequency, θ , of natural oscillations are accurately modelled by a Landau equation [10]

$$\dot{r} = \alpha(r - r^3) \quad (1.2a)$$

$$\dot{\theta} = -1 - \delta r^2 \quad (1.2b)$$

In the Landau model, the parameter $\alpha(> 0)$ is a measure of the instability of the fixed point ($r = 0$) of the mean flow, and $\delta(> 0)$ is a measure of how the frequency changes with amplitude. A typical growth of self-excited oscillations is shown, for a low Reynolds number cylinder wake, in figure 1.4 [11].

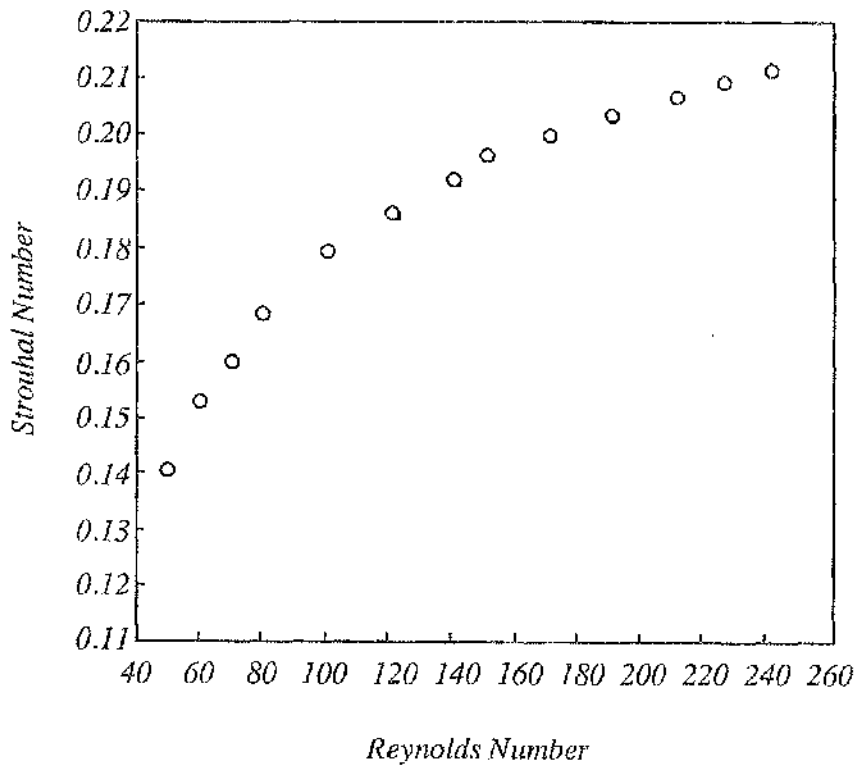
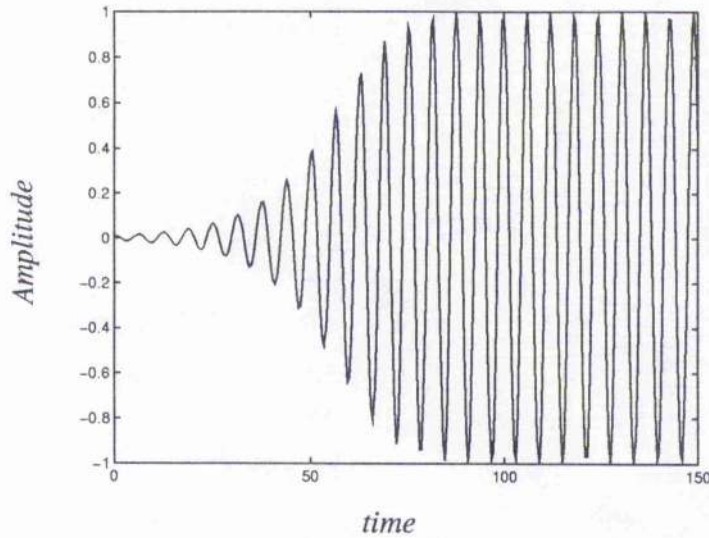


(figure adapted from [2])

Figure 1.3: Strouhal number versus Reynolds number for Cylinder Wakes



Oscillation resulting from Landau equation model of $Re = 100$ cylinder wake. $\alpha = 0.075$ and $\delta = 0.023$ [11]

Figure 1.4: Temporal Growth of Global Mode: Landau Equation

In the cylinder example, and in absolutely unstable wakes in general, the Hopf bifurcation of the wake is the result of amplification of a particular globally unstable mode: the critical global, vortex shedding, mode grows exponentially in time at a rate proportional to $\text{Im}(\omega_G)$, followed by non-linear saturation (towards the Kármán vortex street) and limit cycle oscillations [1]. A linear stability analysis of the time-average flow (calculated during the shedding process) shows the presence of a significantly large region of absolute instability in the near wake of the cylinder [2]. The region of absolute instability extends about five cylinder diameters downstream of the body. If the mean flow velocity profile at a streamwise location behind the cylinder is taken as a constant inflow condition for a flow *without the presence of the cylinder* then an identical vortex street is formed. This observation is confirmed via numerical simulation of the cylinder wake [2][1]— illustrating that the flow oscillations are sustained purely by the instability of the large scale mean flow itself. *Therefore, the global flow oscillations are not strongly dependent on the*

small scale localised movements of the cylinder separation points [1]. The instability of the mean flow (during shedding) acts as a 'wave maker' for the flow oscillations but the flow fluctuations in the absolutely unstable region are smaller than the oscillations downstream [3][1]. The concept of absolute instability is, however, based on a locally parallel flow, which is a fictitious concept—the transition of the flow to absolute instability is therefore not directly observable in experiment, and the stability analysis only explains the global oscillations with prior knowledge of the mean flow during shedding [1]. The mean flow, during shedding, evolves spatially; hence, each location in the wake may, after a local stability analysis, reveal a different global mode [5]. An increase in the flow Reynolds number can increase the number of possible marginally stable global modes, which often have closely spaced frequencies [4]. The natural vortex shedding mode is the most unstable of the global modes [1] (the von Kármán mode always becomes unstable before other modes in wake flows [1]).

Global, self-excited, wake oscillations are therefore seen to be a result of a significant region of local absolute instability of the mean wake flow. The local absolute instability is characterized by the exponential temporal growth of the most unstable global mode. The typical saturated global mode is observed by a non-linear limit cycle and von Kármán vortex shedding in the wake. However, the wake may, in general, possess multiple global modes [1].

1.2 Response of Self-excited Wakes to External Control

The response of the two classes of flow instability to external control forcing is qualitatively different and hence stabilization of a flow is dependent on the nature of the flow instability [4].

For convectively unstable flows, a linear stability analysis reveals the receptivity of the flow to external forcing at various frequencies—out of phase, sinusoidal forcing at the same frequency as the dominant Fourier component of the instability wave can, in theory, stabilize a convectively unstable flow. Linear control laws have, for example, found success in delaying boundary layer transition (in numerical investigations [12], [13], [14] and in experiments [15],[16], [17]). In these schemes, a controlled input is superimposed on the growing disturbance (a Tollmein-Schlichting wave) so that they destructively interfere. Even when global flow oscillations are present in a convectively unstable flow (periodic cavity flow for example) the oscillations are the result of linear amplification or feedback of internal pressure waves—therefore the global flow oscillations at each point in the wake are related by a phase shift and are thus controllable with single sensor, linear feedback.

Control of global flow oscillations that are the result of absolute instability is more difficult. Strategies for control of global flow oscillations can be separated into flow modifiers (where the region of absolute instability is removed by favourable alteration of the mean flow) and control strategies which actively stabilize the unstable modes of the flow. Flow oscillations are preventable if the mean flow is modified so as to become convectively unstable—this passive control is achieved by addition of another body to the flow (for example, a splitter plate or secondary cylinder placed behind the main cylinder) [18][1]. Passive control is, however, severely limited in its applicability [19]. Active control of flow oscillations, where the oscillations are suppressed by time-dependent control forcing of the flow (rather than modification of the mean flow) requires the attenuation of all global modes of the flow [1]. The response of absolutely unstable wakes to external forcing is therefore important when considering an active control scheme.

According to linear theory, an absolutely unstable flow is unresponsive to external forcing: in its initial stages the global (vortex shedding) mode grows exponentially in time and therefore overwhelms any infinitesimal external forcing, which is only

periodic in time [2]. However, the observed result of the absolute instability is the non-linear limit cycle and, while linear stability concepts are useful for explaining the presence of globally unstable modes and self-excited oscillations, linear theory is not appropriate when considering the effects of any finite amplitude external forcing of the non-linear flow [2]. Linear theory is applicable only to *infinitesimal* forcing. Experiments and simulations affirm that the behaviour of an absolutely unstable fluid flow *is* responsive to external control inputs if the amplitude of the control input is above a certain threshold value [2][20]. The response of the absolutely unstable cylinder flow to forcing is characteristic of the response of more general absolutely unstable wakes [1]. Several different forcing techniques affect the behaviour of the cylinder flow. The wake response to forcing is similar whether acoustic excitation of the wake [9], longitudinal or lateral vibration of the cylinder [9], rotation of the cylinder [21], alternate blowing and suction at the separation points [7] or (for low Reynolds numbers) vibrating wires in the wake [2] are used. All of these methods have been proposed for vortex shedding suppression schemes—active control schemes involving rotation of the cylinder [21] or alternate asymmetric suction/blowing [22] have met with some success. Open loop control of a cylinder wake by means of an oscillating aerofoil placed in the near wake has also been used to alter the position and strength of large scale vortex structures in the wake [19].

The response of the cylinder flow, and absolutely unstable wake flows in general, to periodic forcing above the threshold amplitude has the characteristics of a non-linear oscillator with forced oscillations [9][23]. The response of a circular cylinder wake, forced by acoustic excitation, can be characterized by two qualitatively different regimes which are dependent on the frequency content of the applied forcing [2][9]. The first regime is termed a ‘non-lock-in’ state. The flow structures and temporal behaviour of the non-lock-in state are independent of the relationship between the frequency of the applied forcing, f_a , and the natural shedding frequency,

f_o . In this state, the flow is characterized, both spatially and temporally, by a non-linear beat. The shedding frequency can be shifted by up to 25% from the natural value during the beating phenomenon [9].

The second classification of flow response is termed a 'lock-in' state, and occurs when the shedding frequency shifts to an integer ratio of the applied frequency. The lock-in state exhibits wake structures that are dependent on the ratio of the applied and natural shedding frequencies, and which are also dependent on the amplitude of the forcing. The lock-in states are delimited by regions of entrainment, similar to the Arnold's tongues shown by forced non-linear oscillators [23][11]. A sketch of a typical entrainment region is shown in figure 1.5 [23]. A specific class of lock-in state occurs when the shedding frequency changes to half of the applied forcing frequency. This type of lock-in state is called synchronization. The wake types exhibited by the circular cylinder flow during synchronization show a full range of h/l values, from $0 < h/l < \infty$, and therefore display considerable variation. The resultant wake type, dependent on the frequency ratio f_a/f_o and the forcing amplitude A_f , exhibits hysteresis [9]. Three different spatial modes of interaction between a cylinder vortex street and an oscillating aerofoil have been observed experimentally [19]. Alternatively, twelve different spatial shedding modes have been observed during large amplitude acoustic excitation [9].

The response of a self-excited wake flow to external control forcing is therefore a non-linear interaction between the global mode oscillations and the external forcing. The global flow oscillations may also be the result of multiple global modes—this spatial complexity of the flow has important consequences for flow control. At values of the relevant flow parameter (Reynolds number in the cylinder wake example) just above the critical value for self-excited oscillations, there is typically only one globally unstable mode, often resulting in Kármán vortex shedding [1]—therefore the flow behaviour at each point in the wake is related to every other by a simple phase shift [20]. Linear feedback control of such flows is therefore, theoretically,

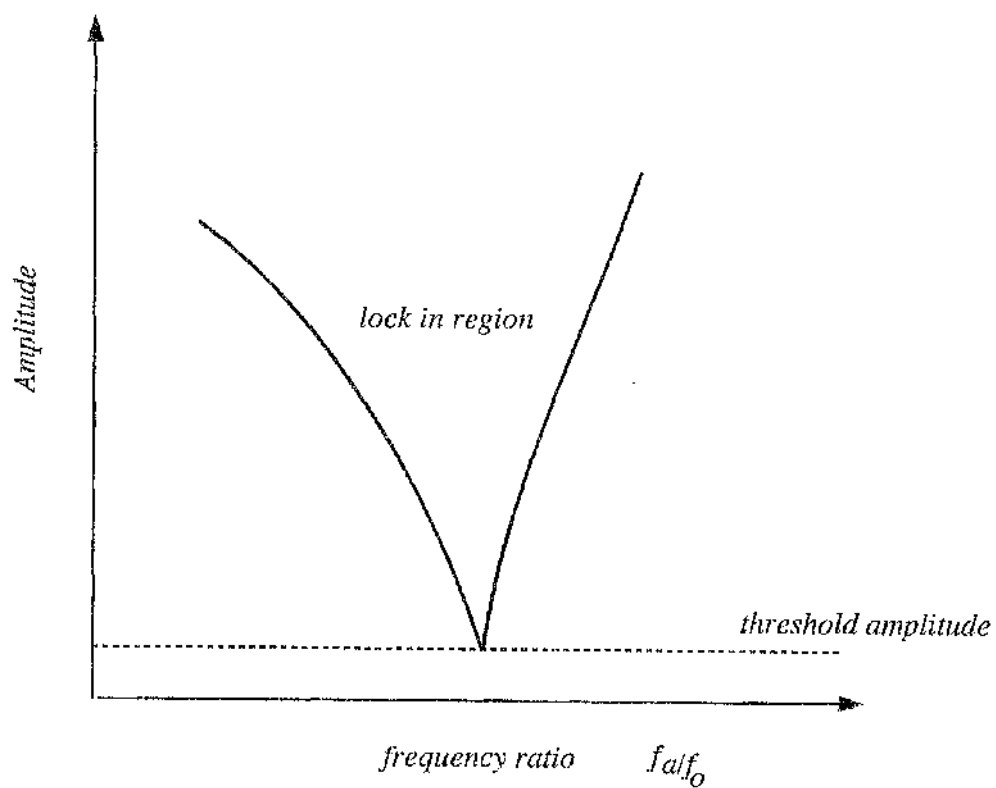


Figure 1.5: Region of Lock-in

possible by means of a *single* sensor/actuator feedback loop. Indeed, single sensor control of such low Reynolds number cylinder wakes has been observed experimentally [20][24][7]. At higher values of the relevant flow parameter, however, other global modes are present. Nevertheless, at only slightly supercritical parameter values (eg. Reynolds numbers no more than $\sim 20\%$ larger than Re_c in the cylinder example) there often exists a ‘gain window’ between the threshold amplitudes for the global modes, such that forcing with an amplitude large enough to suppress the most unstable mode is still not large enough to destabilize the next global mode [20][7]. Complete suppression or control of the wake is therefore still feasible using a single sensor at these slightly supercritical parameter values, even although there may exist multiple global modes [20]. Further beyond the critical value, however, the ‘gain window’ shrinks so that the forcing amplitude necessary to control the most unstable mode merely destabilizes the next most unstable mode [7][4]. Oscillations may be suppressed at the sensor location [24] but are, in general, exacerbated elsewhere [7] — the self-excited wake behaves like a set of spatially coupled local oscillators [25]. *Points in the wake are therefore not merely connected via a phase shift and so multiple, spatially distributed sensors are needed for control of the flow.* A sketch of the gain window for an absolutely unstable cylinder wake is shown in figure 1.6 [7]. The diagram represents the change in wake oscillations amplitude as the control amplitude is raised [7]. As the control amplitude increases, the high frequency component (in this case corresponding to the natural shedding mode) is suppressed. As the amplitude is further increased, there is a range where no flow oscillations are present, but the growth of low frequency oscillations (corresponding to the next global mode) is seen at even higher amplitudes. The destabilization of further global modes is also illustrated in figure 1.7 [20], which shows attempted single sensor control of the $Re = 80$ flow around a cylinder. The natural shedding mode, corresponding to the most unstable global mode can be suppressed via single sensor feedback. Once the natural shedding oscillations are suppressed, however, the

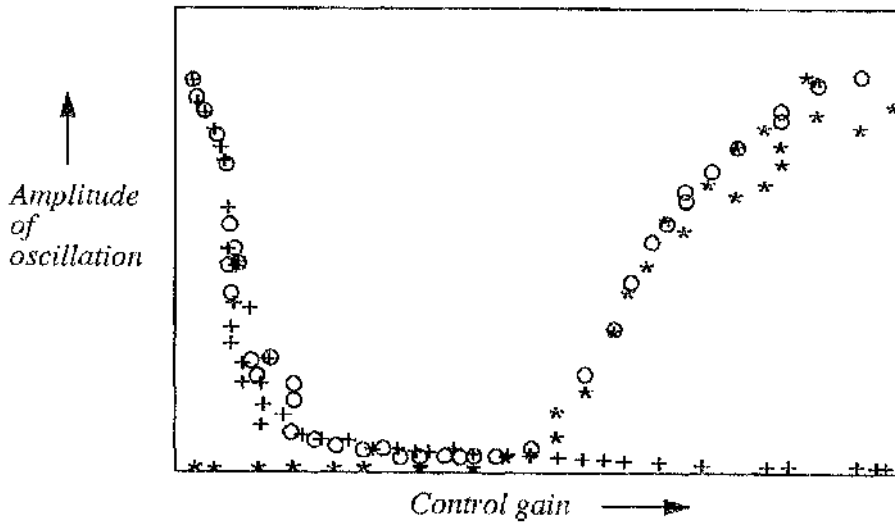
wake oscillations resume with a different growth rate, and attain different amplitude and frequency from the natural shedding mode; these new oscillations correspond to the excitation of the next global mode. The wake structure is also different as a result.

1.3 Low-Dimensional Control of Self-excited Fluid Wakes

When considering control of wake oscillations, it is important to distinguish between flows where the oscillations are due to intrinsic feedback or extrinsic noise and flows where the oscillations are due to global instability of the flow. Globally unstable flows contain a region of absolute instability and, because of the nature of the flow, are not, in general, controllable with single sensor linear control methods. In general, an absolutely unstable flow is characterized by a Hopf bifurcation from a steady to a periodic state at some critical value of a flow parameter. The amplitude and frequency of the natural oscillations are accurately modelled by a Landau equation and the Kármán vortex street is the typical natural, saturated mode of oscillation. The oscillations in the wake exist purely as a result of the absolute instability of the mean flow.

The self-excited oscillations of an absolutely unstable wake flow are responsive to external forcing only above a certain threshold amplitude; the response of the flow to excitation is characteristic of a non-linear oscillator with forced oscillations. It is typical for a globally unstable flow to contain multiple global modes; the most unstable mode results in the observed natural oscillations of the wake. In general, single sensor, linear feedback is able to suppress a single global mode, but it is likely to excite the next most unstable mode, thus defeating its purpose. A linear stability analysis of the mean flow may reveal many global modes at each streamwise location in the wake and, often, the global modes have closely spaced frequencies. The

Experimental results



Response at single control sensor as control gain is increased, for Re 52.8.

- - total signal
- + - high frequency range component
- * - low frequency range component

schematic

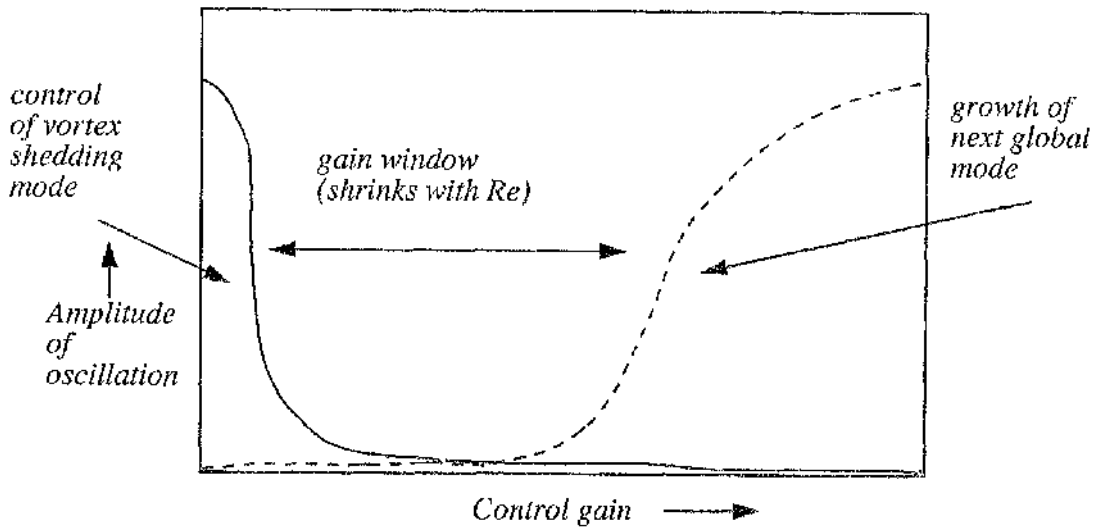
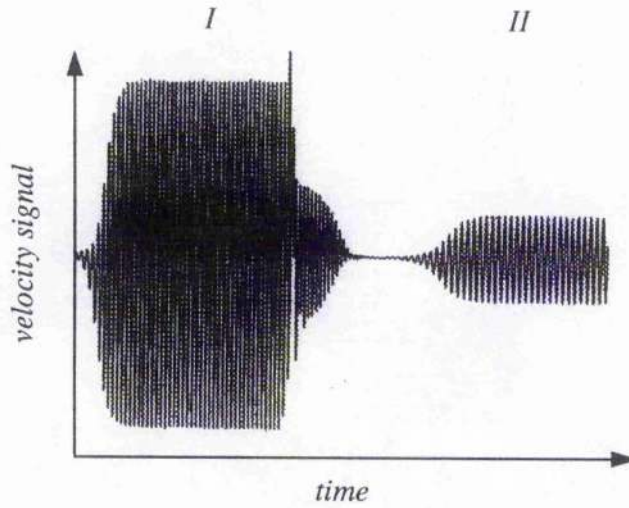
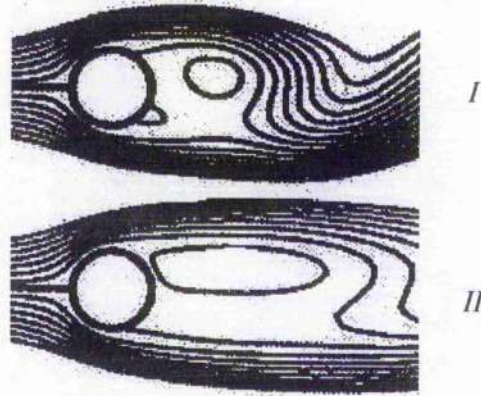


(figure adapted from [7])

Figure 1.6: Gain Window Observed in Cylinder Flow



Time history of u -velocity component at sensor location during an attempted control run. Signal shows evidence of global modes I and II. $Re=1.7Re_c$



Typical wake structure during modes I and II.

(figure adapted from [20])

Figure 1.7: Attempted Single Sensor Control of Multiple Global Modes of Circular Cylinder

presence of multiple global modes thus necessitates the use of multiple control sensors at various streamwise locations for the suppression of all possible modes [19][4]. The spatio-temporal response of the wake is non-linear— therefore the most efficient control strategy is also non-linear. A linear control strategy, based on a linear model of the flow dynamics is consequently less accurate [26]. A multiple-sensor, non-linear control is therefore, in general, the best strategy to adopt for the complete suppression of self-excited wake oscillations caused by global instability.

If the absolutely unstable region is to be adequately represented with multiple control sensors, then many flow variables (for example velocity or pressure) at many points throughout the unstable region are needed within the feedback or control algorithm. The resulting control algorithm involves many variables and will therefore be complicated and computationally slow. If, however, the complex spatio-temporal information, needed for non-linear feedback stabilization of multiple global modes, is characterized by a relatively small number of quantities— given by a low-dimensional description of the flow features and their response to external forcing —then it is reasonable to assert that the feedback control algorithm can be made simpler and computationally feasible. Typically, flows exhibiting self-excited oscillations as a result of global instability are dominated by the dynamics of large scale spatial structures— the dynamics of small scale spatial structures are relatively unimportant in the evolution of the flow. Often, the large scale structures of a dissipative fluid flow can be represented by a finite set of spatial features. A control strategy that is restricted to measurement and control of just a finite number of large scale spatial structures in the fluid wake flow is potentially simpler than a control scheme which attempts to control both the large and small scales of the flow. A control strategy restricted to large scale spatial structures is, however, able to control the most important features of the wake oscillations. It has been shown experimentally that a self-excited fluid wake can be altered in a desired manner by the direct control of just large scale structures in the wake [19].

A non-linear dynamical model for the large scale wake structures and their response to control forcing is helpful for the design of a control algorithm. However, analytical determination of such a model by classical means is difficult. Neural networks can be used to provide empirical relationships between sets of input-output data and can therefore be used to predict the response of the large scale structures to control forcing. Emulation of the large scale flow dynamics with neural networks also allows straightforward design of a non-linear neural network controller for stabilization of the large scale flow variations.

1.3.1 The Dynamics of Large Scale Spatial Structures in Dissipative Fluid Flows

Experimental, self-excited wake flows are dominated by large scale spatial structures [19][9]— solutions of mathematical models of such wakes are also dominated by large scale spatial components [27]. The continuum model of the macroscopic characteristics of fluid flow is well established; the Navier-Stokes equations for viscous, incompressible flow are an example of one such model. The phase space of a partial differential equation, such as the Navier-Stokes equations, is infinite-dimensional. Even an approximate numerical solution of the discretized Navier-Stokes equations will have a phase space of very high dimension. However, experimental evidence often shows that viscous fluid flows can have relatively simple asymptotic dynamics (sometimes, for example, characterized by limit cycle behaviour which, even in an infinite phase space, is representable by dynamics in a two-dimensional space). Intuitively, simple dynamical systems of finite-dimension should be able to describe the simple fluid phenomena observed in many experiments. Dynamical systems theory provides a mathematical framework for this approach.

Dissipation of energy through viscous effects is significant for many fluid systems.

Typically, the solutions of dissipative systems converge to a finite-dimensional, attracting set in phase space [27]. Hence, the asymptotic dynamics of many infinite dimensional *dissipative* systems are often finite-dimensional and can be modelled by a finite number of ordinary differential equations [27]. Certain dissipative systems possess an *inertial manifold*, which is a finite-dimensional subset of the system's phase space, towards which global solutions of the system are attracted exponentially fast [28]. The inertial manifold contains the global attractor for the system and sometimes exists for a range of parameter values [29]. An important feature of the inertial manifold is its invariance; once the solution of the system is on the manifold 'surface' it remains there. Therefore, most of the salient dynamics of the system take place on the finite-dimension manifold, and can be described by a *finite*, rather than infinite, system. Only a small transient part of the dynamics is not described by the manifold geometry.

Typically, partial differential equation systems which possess an inertial manifold have solutions composed of widely differing spatial scales. Specifically, an inertial manifold exists only if there is a large gap between the wavelengths of the large scale components and those of the small scale components [28]. The number of large scale components, which contribute most of the solution, is often very much smaller than the number of small scale components, which have little gross effect on the solution. A large number of degrees of freedom are therefore taken up by the relatively unimportant small scales of the solution.

The infinite phase space of the partial differential equation can be decomposed into two orthogonal sub-spaces: a finite sub-space spanning the large scale components and a complementary, infinite space spanning the small scale components [30]. A projection of the partial differential equation onto these sub-spaces yields two coupled ordinary differential equations in the two different scales. The equation of the inertial manifold provides either an approximate or an exact functional relationship

between the small scale solution and the large scale solution, allowing the asymptotic dynamics of the partial differential equation to be described completely by an ordinary differential equation set that is a function only of the finite-dimensional large scale components [30]. This finite equation set is the *inertial form* of the partial differential equation [27]. For fluid systems, the large scale components can be identified with large scale spatial vortex structures, and the small scale components with small eddies.

It has been shown [28] that the two-dimensional, incompressible Navier-Stokes equations *do* possess an inertial manifold for certain boundary conditions. Also, the simple dynamics observed in many fluid experiments suggest, from a physical point of view, that a low-dimensional description of certain fluid flows is adequate. For example, the temporal behaviour of large scale spatial structures in the Kármán vortex street can be modelled by a simple non-linear oscillator equation. The dynamics of the large scale spatial structures in the vortex street are relatively insensitive to perturbation on a small spatial scale. The existence of an inertial manifold justifies the search for low-dimensional approximations of many viscous fluid flows.

The existence of inertial manifolds and global attractors for non-autonomous fluid systems with time-dependent forcing is of interest in a control context. A valid low-dimensional description of a wake flow in the presence of a control input is helpful for the design of a control algorithm. An inertial form of the Navier-Stokes equations exists for cases of time-dependent forcing, as long as some restrictions are placed on the type and character of the forcing [28]. Specifically, the inertial manifold approach is valid for *periodic* forcing or for forcing that enters a *compact set* within a finite time. Otherwise a global attractor for the system might not exist. There is therefore some justification for the use of low-dimensional models to describe the forced or controlled behaviour of fluid systems. Further justification, for the use of low-dimensional models as descriptions of forced wake flows, comes from physical evidence.

The case of periodic forcing is most applicable to an inertial manifold approach [28] and there is a wealth of experimental evidence which supports the observation that periodically forced wakes are low-dimensional and dominated by large scale structures. As discussed in section 1.2, relatively simple dynamical behaviour is displayed by the periodically forced circular cylinder vortex street. It has been estimated that there are only twelve qualitatively different types of wake structures in evidence in an acoustically forced circular cylinder wake [9] and only three basic modes of interaction are observed behind a cylinder with an oscillating aerofoil in its wake [19]. Several low-dimensional models have been employed, with some success, to predict the temporal dynamics of forced cylinder wakes. The dynamical features of the forced sine circle map [23] have been compared with the response of a periodically forced cylinder wake; and a simple cubic equation with empirically derived coefficients (from an unforced but transient wake), with an *ad hoc* additive sinusoidal forcing term in the equation, is capable of producing temporal shedding responses that agree qualitatively with experiment [11]. Characterization of the spatial features of harmonically forced flows by orthogonal decomposition also shows that a low-dimensional description is often adequate [31]. It also seems that, for some flows, the resulting spatial characterization *does not significantly differ* from one derived for anharmonic forcing, which suggests that a low-dimensional description may be valid for more general types of forcing [31].

The determination of an exact inertial form of a complex fluid system is very difficult. However, a similar representation of the large scale (and hence most important) dynamics can be derived empirically with the method of Proper Orthogonal Decomposition (POD) [32], [33]. Proper orthogonal decomposition is an *unbiased* approach for the selection of coherent spatial structures from a flow field. The method was developed in the context of statistical pattern recognition, and has been used as a method for the selection of large scale coherent structures from turbulent fluid flows [32]. The method proceeds with the calculation of the eigenvectors of the flow

field correlation matrix. Each eigenvector can be recognized as a ‘direction’ in phase space in which the velocity field has a statistical maximum. The eigenvectors, or modes, thus constitute a linear, orthogonal subspace that encapsulates the region of phase space in which the velocity field is statistically likely to be found—which is the global attractor (if one exists). Proper orthogonal decomposition is to be preferred over other characterization methods because it is linearly optimal; that is, it captures a larger amount of kinetic energy than any other linear expansion for a given number of modes. The linear, orthogonal sub-space spanned by the modes is similar to the finite sub-space of an inertial manifold, but the empirical decomposition method makes no attempt at direct parameterization of the attractor. Proper orthogonal decomposition has been successful in low-dimensional characterization of spatial patterns (for example, the characterization of human faces [34]), detection of coherent structures in turbulent flows [35] [36] [37], and also in the spatial and temporal characterization of boundary layer transition [38]. It has also been used in the low-dimensional modelling of complex geometry flows such as the grooved channel and circular cylinder wake [39], and wakes of thick aerofoils [40], and also forced wake flows such as the periodically forced mixing layer [31]. Although the method is significantly different from the inertial manifold approach, it is similar in character, and it provides a useful tool for the spatial and temporal characterization of fluid flows. Laminar wakes can be characterized by much smaller sets of features than turbulent wakes [39]—the POD modes of a turbulent flow have a more widespread energy distribution. The characterization of turbulent wake flows by low-dimensional sets of POD modes is still feasible [36], but the dimensions of the resulting characterizations are likely to be much larger than those for laminar wakes.

1.3.2 Control of Large Scale Spatial Structures with Neural Networks

The flow field of a self-excited wake flow can be approximated by the large scale spatial structures in the flow. The large scale structures of the flow can often be characterized by a finite and relatively small number of orthogonal spatial modes with corresponding time-dependent amplitudes, developed using proper orthogonal decomposition [33]. The fluctuating wake velocity field is approximated by a finite, linear combination of the POD modes. A control strategy which manipulates the flow such that the mode amplitudes reach a desired state is able to control the large scale structures in the flow, which are responsible for most of the flow kinetic energy. The control algorithm can be made computationally feasible because it operates with a finite, low-dimensional representation of the velocity field.

In order to devise a non-linear control algorithm, a model for the evolution of the mode amplitudes in response to an external control is helpful [14]. Classically, evolution equations for the unforced, autonomous POD mode amplitudes are determined with a Galerkin approximation of the Navier-Stokes equations [33]. The POD modes satisfy the flow boundary conditions and so the effect of a control input (which may involve boundary or interior control) is to modify the form of the low-dimensional model describing the evolution of the mode amplitudes. However, while the analytical form of the low dimensional flow model is known for autonomous flows, the structure of the low-dimensional model for controlled flows depends intimately on the nature of the control process which, itself, may be difficult to model.

Nevertheless, the notional existence of a low-dimensional flow model in the presence of a control is appealing. Neural networks have been applied to non-linear control problems where analytical representation of the system has proved difficult or impractical [41][26][14]. For the flow control problem, a neural network can be trained to estimate empirically the response of the mode amplitudes to an applied

control, and an adjoining network trained to control the flow. The advantages of this approach are that it avoids the need for explicit representation of the low-dimensional flow model, and that, because the dynamics are estimated empirically, any dynamical effects of the neglected small scales of the flow are not ignored (the Galerkin process completely ignores the dynamical effects of the small spatial scales). Also, the neural network approach allows design of a non-linear control algorithm without recourse to complicated analytical non-linear control theory [14].

One type of neural network is the multi-layer perceptron [42]. The basic processing unit of the multi-layer perceptron is the neuron, which was originally posed as a mathematical model for biological brain cells. The multi-layer perceptron can be used to approximate any non-linear algebraic mapping between a set of inputs and a set of outputs. The network *learns* to approximate an unknown function between two sets of input and output data by application of a training algorithm which alters the strengths of the connections between the neurons of the network. One such training algorithm is *error backpropagation*, in which the inter-neuron connection strengths are updated by a function of the local error gradient. Once a neural network is trained to emulate the non-linear response of the flow (described by a finite number of mode amplitudes) then the difference between the desired state of mode amplitudes and the actual mode amplitudes can be backpropagated through the emulator to train another neural network to provide a control input to the flow. The controller network is trained in such a way that the control system error diminishes at each time step. This type of non-linear control strategy is robust to external perturbation and any un-modelled disturbances in the flow [26].

1.4 Outline of the Dissertation

The aim of the present study is to develop a generic control strategy for self-excited wake flows that is computationally fast, by virtue of a low-dimensional description of

the flow dynamics, but also addresses the potentially non-linear, spatially distributed nature of the flow.

The dissertation makes no *explicit* use of the mathematics of absolute instability theory, nor does it make *explicit* use of analytical methods for the derivation of an inertial manifold of the Navier-Stokes equations. However, the *qualitative* flow behaviour resulting from absolute instability is used to suggest the character and type of feedback that is to be employed. Also, the concepts of inertial manifolds, and their existence for forced flows, are exploited to suggest that a low-dimensional description of the flow dynamics is possible. Both theoretical and experimental evidence is employed to support this view. It is the combination of the *qualitative* results of stability theory, together with the characterization of the flow by a low-dimensional model into a control scheme that is the main contribution of the dissertation.

Chapter Two begins with the premise that multiple sensors are needed for the stabilization of multiple global modes present in an oscillating wake flow. A control algorithm can be made computationally feasible if the complex spatial information (recorded by the multiple, spatially distributed, sensors) is characterized by a low-dimensional set of spatial modes. The characterization of spatial systems, governed by partial differential equations, by low-dimensional systems is addressed with reference to exact and approximate inertial manifolds. It is shown that the method of proper orthogonal decomposition furnishes a readily identifiable coordinate basis with which to represent the flow. Truncation of this basis allows low-dimensional characterization of the spatial features of the wake flow. The validity of low-dimensional approximations for wake flows with time-dependent forcing (as would be present during flow control) is also addressed. Some remarks are made as to the possible changes in manifold geometry that occur as a result of time-dependent forcing. The extension of the classical proper orthogonal decomposition to non-stationary flows with time-dependent control inputs is discussed.

An efficient, robust, non-linear control strategy for the stabilization of the POD

modes can be designed if the dynamical behaviour of the POD modes of the flow can be predicted. The development of such a control strategy is presented in Chapter Three. In contrast to classical, Galerkin methods of estimating the mode dynamics, an empirical method is presented. It is shown that an empirical prediction of the mode amplitude response, after application of a control input, can be achieved using a non-linear neural network. The advantages of empirical prediction of the mode dynamics are discussed. It is also shown how the neural network emulation of the mode amplitude response forms the core of an adaptive non-linear neural network control strategy. Finally, the chapter presents a method for estimation of the POD modes and amplitudes via another neural network, so that the characterization, dynamic modelling, and control strategy are all constructed using the same framework.

Control of a prototype absolutely unstable flow is used as an example of success of the control strategy. The prototype flow is a simple model which retains the salient stability features of a circular cylinder wake. The results of the prototype model are presented in Chapter Four. The prototype flow shows qualitative agreement with both the temporal and some of the spatial features of actual forced and unforced cylinder wakes. The validity of the prototype model, with regard to testing the control strategy, is also discussed. The construction of the controller is presented and its performance is discussed in comparison to linear control strategies and single point feedback.

Chapter 2

Characterization of Dissipative Fluid Flows

2.1 Introduction

Some of the difficulties of attempting active control of an absolutely unstable fluid flow were outlined in the first chapter. Absolutely unstable flows are both spatially and temporally complex and active control of the flow by feedback of an *isolated* flow measurement is often unsuccessful. The flow oscillations at the measured point may be suppressed by the control, but oscillations are often exacerbated elsewhere by the excitation of other global modes of oscillation. Stabilization of an absolutely unstable flow requires attenuation of all unstable or destabilized global modes. Multiple, spatially distributed measurements— contained in, say, ‘pictures’ or ‘snapshots’ of the flow field which comprise the values of important flow variables at a distribution of points in space— are needed to suppress completely all of the global modes of an absolutely unstable flow [1][4].

While the initial absolute instability is a linear concept, the initial exponential growth of the global mode saturates to a large amplitude *non-linear* limit-cycle[1].

The initial linear instability is often unobservable in experiment, and the only observable result of the instability is the non-linear limit cycle [1]. As the response of the observed limit cycle to a control input is non-linear[2] then the most appropriate control algorithm is also non-linear. Linear control algorithms based on linear models of the flow dynamics are consequently less accurate than non-linear schemes. If the control algorithm makes explicit use of all of the information contained in a high resolution 'picture' of the flow field then it will be very complicated and computationally slow[14]. The incorporation of so many quantities into a non-linear control algorithm is a significant task. (For example, a digitized image of only one scalar flow variable recorded at 256×256 points in $x - y$ space contains 2^{16} quantities.) It would therefore be helpful if the large dimension set of information contained in 'pictures' of the flow field could be characterized by a smaller set of quantities without losing a significant amount of information. Some of the theoretical and experimental evidence that demonstrates the plausibility of such a low-dimensional description or characterization of the spatio-temporal features of certain fluid flows was discussed, with reference to the concept of inertial manifolds, in the first chapter.

2.2 Geometric Characteristics of the Navier-Stokes Equations

Dissipative partial differential equation models of fluid flow such as the Navier-Stokes equations often have solutions composed of widely differing spatial scales. Often, most of the flow kinetic energy is contained within a relatively small number of large scale components; whereas the small spatial scales, which take up many (perhaps infinite) degrees of freedom, contain very little energy. An inertial manifold is a feature of certain dissipative partial differential equations that have solutions composed of large and small scales. An inertial manifold is a finite-dimensional attracting, invariant sub-set of phase space that attracts all solutions of the partial differential

equation exponentially [30], and hence contains the global attractor. The equation of an inertial manifold provides a functional relationship between the large and small scale components; it allows the partial differential equation system to be written in terms of a finite number of large scale components described by an ordinary differential equation system. The concept of reducing the dimension of a system with an inertial manifold is shown below with reference to a symbolic representation of the Navier-Stokes equations for fluid flow. The unforced (statistically stationary) case is considered first (adapted from [30] and [28]). The existence of inertial forms or low-dimensional approximations for forced, non-stationary flows, relevant to wake control, is explained in a later section.

The two-dimensional Navier-Stokes equations for a *viscous*, incompressible fluid in a region Ω are, for each $t > 0$,

$$\frac{\partial \mathbf{u}(\mathbf{x}, t)}{\partial t} = -(\mathbf{u}(\mathbf{x}, t) \cdot \nabla) \mathbf{u}(\mathbf{x}, t) - \nabla \Pi(\mathbf{x}, t) + \nu \nabla^2 \mathbf{u}(\mathbf{x}, t) \quad (2.1a)$$

with

$$\nabla \cdot \mathbf{u}(\mathbf{x}, t) = 0 \quad (2.1b)$$

and initial condition,

$$\mathbf{u}(\mathbf{x}, 0) = \mathbf{u}_0(\mathbf{x}) \quad (2.1c)$$

supplemented with periodic or Dirichlet boundary conditions on the boundary $\partial\Omega$ [27]. The kinematic viscosity ν is greater than zero and the dissipative term is $-\nu \nabla^2 \mathbf{u}$. $\nabla \Pi$ is the pressure term and $(\mathbf{u} \cdot \nabla) \mathbf{u}$ is the convection term.

The partial differential equation (2.1) can be represented, by classical methods [27], as a symbolic evolutionary equation in an infinite Hilbert space H .

$$\frac{d\mathbf{u}}{dt} + \nu A\mathbf{u} + B(\mathbf{u}, \mathbf{u}) = 0 \quad (2.2)$$

where A denotes the dissipation operator, restricted to divergence-free periodic vector fields, such that

$$A\mathbf{u} = -P\nabla^2 \mathbf{u} \quad (2.3)$$

where P denotes the orthogonal projection in $L^2(\Omega) \times L^2(\Omega)$ onto the Hilbert space, H , with a well defined inner product (\mathbf{u}, \mathbf{u}) and norm $|\mathbf{u}|$. B denotes the operator

$$B(\mathbf{u}, \mathbf{v}) = P((\mathbf{u} \cdot \nabla)\mathbf{v}) \quad (2.4)$$

The orthogonal projection on to the *first* m eigenvectors, $\{\psi_1, \psi_2, \dots, \psi_m\}$ of the linear dissipation operator A is denoted by P_m . The subspace spanned by this projection is $H_m = P_m H = \text{span}\{\psi_1, \psi_2, \dots, \psi_m\}$. The complementary projection, is $Q_m = I - P_m$, where I is the identity operator. The large scale component of the solution is represented by $\mathbf{p} = P_m \mathbf{u}$ (taking up m degrees of freedom) and the small scale component by $\mathbf{q} = Q_m \mathbf{u}$ (describing the evolution of \mathbf{u} on the complementary, infinite subspace). The total solution is

$$\mathbf{u} = \mathbf{p} + \mathbf{q} \quad (2.5)$$

and the evolutionary equation can be re-written in terms of the two spatial scales.

$$\frac{d\mathbf{p}}{dt} + \nu A\mathbf{p} + P_m B(\mathbf{p} + \mathbf{q}, \mathbf{p} + \mathbf{q}) = 0 \quad (2.6)$$

$$\frac{d\mathbf{q}}{dt} + \nu A\mathbf{q} + Q_m B(\mathbf{p} + \mathbf{q}, \mathbf{p} + \mathbf{q}) = 0 \quad (2.7)$$

The inertial manifold equation provides an algebraic relationship between the small and large scales of the solution such that $\mathbf{q} = \phi(\mathbf{p})$ and the total solution can be expressed as $\mathbf{u} = \mathbf{p} + \phi(\mathbf{p})$. The *inertial form* of the original evolutionary equation portrays the dynamics of the system *on the manifold*, and is

$$\frac{d\mathbf{p}}{dt} + \nu A\mathbf{p} + P_m B(\mathbf{p} + \phi(\mathbf{p}), \mathbf{p} + \phi(\mathbf{p})) = 0 \quad (2.8)$$

The asymptotic dynamics of the fluid that are restricted to the manifold are completely determined by the m -dimensional ordinary differential equation (2.8)[28]. In practice, the salient dynamics of the system are always restricted to the manifold—only a small transient part is not [28].

The issue of whether an inertial manifold exists for a particular flow is complex—the existence of inertial manifolds has been dealt with explicitly only for a few simple cases [29]. However, a useful rule is that an inertial manifold can exist if the gap between λ_m (the largest eigenvalue of $A|_{P_m H}$) and λ_{m+1} (the smallest eigenvalue of $A|_{Q_m H}$) is large enough—corresponding to a large enough gap in the wavelengths of large and small spatial structures in the flow [28]. There are good physical reasons for expecting an inertial form of the flow equations to exist for absolutely unstable wakes. Flows of this type are *dominated* by the oscillations of *large scale* spatial structures (for example the Kármán vortex street is a large spatial structure) which are relatively insensitive to perturbations on a small spatial scale. The oscillations of a vortex street are known to grow from an initial absolutely unstable state, corresponding to the mean flow, that is also dominated by significantly large scale spatial structure (the twin vortices of the mean flow behind a cylinder during shedding is an example). It can therefore be expected that small spatial scales, while important for structures in the boundary layer on the cylinder, are relatively unimportant (that is, they have little energy) in a representation of the dynamics of the flow [40]. A two-dimensional wake flow with a finite number of vortices or flow structures with non-vanishing strength can be represented by a finite dimension system [43]. If a wake flow is periodic or quasiperiodic with n distinct fundamental frequencies (excluding harmonics) then its velocity field is spanned by n phase angles — the flow is thus effectively n -dimensional [43].

The analytical determination of the manifold equation is also generally difficult and is only straightforward for a few systems where the dimension, m , of the manifold is very low. The use of exact inertial forms as simplifications of the flow equations is conceptually appealing but usually of little practical use; the dimension of the inertial manifold for even moderately complex flows can be very large ($O(10^9)$ for some flows) [29]. Given that the determination of an exact inertial manifold is difficult, *approximate inertial manifolds* (which have been shown to exist even when

an exact inertial manifold is not formally known to exist) are often of use [28]. If an inertial manifold attracts all solutions asymptotically to a finite-dimensional hyperplane, then an approximate inertial manifold can be thought of as attracting all solutions to a thin strip, or neighbourhood, that contains the global attractor. Manifolds of this type are functions whose graph, $M_{app} = \text{graph}(\phi_{app})$, in phase space approximates the global attractor. They are simple and are more practical than exact inertial manifolds as devices for the construction of an approximate inertial form to reflect the dynamics of the partial differential equation system. The crudest approximation is a flat space ($\phi_{app} = 0$) so that the solution of the flow is approximated only by the large scale components (this approximation is equivalent to a standard Galerkin scheme [28]). However, if the small spatial scales are approximated by an appropriate non-trivial function of the large spatial scales, then the dynamics are better approximated than by assuming $\phi_{app} = 0$. An approximate relation for parts of \mathbf{q} is determined from the approximate solution of (2.7) [27], hence,

$$\mathbf{q} \simeq \phi_{app}(\mathbf{p}) = (\nu A)^{-1}[-Q_m B(\mathbf{p}, \mathbf{p})] \quad (2.9)$$

which assumes that $|\dot{\mathbf{q}}|$ is small enough to neglect in equation (2.7) [28] [27].

The dynamical behaviour of a fluid flow may change markedly with parameter variations such as Reynolds number. An absolutely unstable flow, like the cylinder wake, can evolve through disparate stages of laminar, turbulent, periodic and aperiodic oscillations. The transitions between types of qualitatively different dynamical behaviour correspond to regions of high curvature or twists in the inertial manifold or global attractor. An attempt to parameterize these regions of the inertial manifold will result in a manifold or attractor of very high dimension. It is therefore more practical to search for a suitable coordinate basis that encapsulates, or approximates, only a *local* region of the inertial manifold [29].

2.3 The Method of Proper Orthogonal Decomposition

Low-dimensional characterization of absolutely unstable, dissipative fluid wake flows is inspired by the existence of exact or approximate inertial manifolds, even when the direct parameterization of such manifolds is difficult or not available. When an exact or approximate inertial form of the flow equations is known, the solution to the flow equations can either be exactly or approximately stated as an algebraic function of the history of the large scale spatial structures. In seeking to encapsulate a local region of the inertial manifold, it therefore appropriate to search for some *readily* identifiable coordinate basis that spans the large scale components of the solution (at, say, a particular Reynolds number). Such a basis is furnished by Proper Orthogonal Decomposition; a method which, without bias, selects an orthogonal set of spatial modes that are optimal in terms of retained *kinetic energy*. The high energy modes may be identified with the large scale spatial structures appearing in the flow [36] [39]. The method determines the smallest linear sub-space that is sufficient to describe the observed flow phenomena, but makes no assumptions on the non-linearity of the problem of interest.

Proper orthogonal decomposition was originally developed in the context of pattern recognition and has been used successfully as a method for determining a low-dimensional description of human faces [34]. The method has also been used to identify large scale coherent structure in turbulent flows [33], such as jet flow and boundary layer transition, and has also been used successfully to characterize coherent structures occurring in laminar wakes or flows around complex geometries [39]. The method as presented here (adapted from [32]), from first principles, highlights the absence of bias in the POD representation.

An efficient method for characterizing an unsteady flow field concentrates on departures from the mean[34]. A velocity field, measured at discrete spatial points,

may be represented as a concatenated vector of local Cartesian velocity components formed from the sum of a mean (time average) flow and a fluctuating part. For a two dimensional flow, which is measured at P discrete spatial points, the velocity field vector is of the form,

$$\mathbf{V}(t) = \overline{\mathbf{V}} + \mathbf{V}'(t) \quad (2.10)$$

where $\overline{\mathbf{V}}$ is the time average flow and,

$$\mathbf{V}'(t) = \begin{bmatrix} \mathbf{v}(x_1, y_1, t) \\ \mathbf{v}(x_2, y_2, t) \\ \vdots \\ \mathbf{v}(x_P, y_P, t) \end{bmatrix} \quad (2.11a)$$

is the fluctuating velocity field, and

$$\mathbf{v}(x_i, y_i, t) = \begin{bmatrix} v_x(x_i, y_i, t) \\ v_y(x_i, y_i, t) \end{bmatrix} \quad (2.11b)$$

is the local fluctuating velocity vector at a point i . It is required to characterize the fluctuating flow by a fixed vector $\boldsymbol{\psi}$ that has a 'direction', in phase space, as close as possible to the fluctuating velocity field vector in the sense that the projection

$$(\boldsymbol{\psi} \cdot \mathbf{V}'(t)) = \boldsymbol{\psi}^T \mathbf{V}'(t) \quad (2.12)$$

is maximized[32]. So that the magnitude of $\boldsymbol{\psi}$ has no effect on the maximization, $\boldsymbol{\psi}$ is subject to the constraint that $\boldsymbol{\psi} \cdot \boldsymbol{\psi} = 1$. To characterize a flow from an ensemble of velocity field realizations it is necessary to find a vector which is best correlated with every member of the ensemble[32][35]. Because $E\{\mathbf{V}'(t)\} = 0$, the best statistical measure over which to maximize (2.12) is the mean square

$$E\{(\boldsymbol{\psi} \cdot \mathbf{V}'(t))^2\} = \lambda \geq 0 \quad (2.13)$$

Maximization of (2.13) produces the best correlated vector to the ensemble of velocity field realizations in a mean square sense[33].

$$E\{(\boldsymbol{\psi}^T \mathbf{V}'(t))(\mathbf{V}'(t)^T \boldsymbol{\psi})\} = \lambda \quad (2.14)$$

$$\boldsymbol{\psi}^T \mathbf{R} \boldsymbol{\psi} = \lambda \quad (2.15)$$

where \mathbf{R} is the time average, spatial correlation matrix of the velocity field,

$$\mathbf{R} = E\{\mathbf{V}'(t)\mathbf{V}'(t)^T\} \quad (2.16)$$

It is readily shown that extremal $\boldsymbol{\psi}$ correspond to eigensolutions of the algebraic eigenproblem[33][34]

$$\mathbf{R}\boldsymbol{\psi} = \lambda\boldsymbol{\psi} \quad (2.17)$$

The matrix eigenproblem defined by (2.17) yields an *orthonormal* set of vectors that characterizes the spatial structure of the flow. The eigenvectors, or modes, can be recognized as 'directions' in \mathfrak{R}^{2P} along which the variance of the discretized velocity field has local maxima.

Solution of the eigenproblem (2.17) is a difficult task if the number of spatial measurement points, P , is large—the problem is of order $(2 \times P)^2$ for flows comprising two space variables. The effective order of the problem can be reduced, however, using the method of 'snapshots'[33].

2.3.1 The Method of Snapshots

For a sufficient number of time-sampled fluctuating velocity fields, or *snapshots*, $\mathbf{V}'(t_k), k = 1, \dots, M$, the time average correlation matrix is approximated by

$$\mathbf{R} \approx \frac{1}{M} \sum_{k=1}^M \mathbf{V}'(t_k)\mathbf{V}'(t_k)^T \quad (2.18)$$

The approximate correlation is symmetric and non-negative and the number of snapshots, M , is typically less than the dimension of \mathbf{R} . Consequently, \mathbf{R} is singular [34] and only has M non-zero eigenvalues [34][36] [33]. The eigenvectors are of the form[33]

$$\boldsymbol{\psi} = \sum_{k=1}^M A_k \mathbf{V}'(t_k) \quad (2.19)$$

where the amplitude

$$A_k = (\boldsymbol{\psi} \cdot \mathbf{V}'(t_k)) \quad (2.20)$$

Substitution of relation (2.19) into the eigenproblem (2.17) results in the reduced eigenproblem,

$$\mathbf{C}\mathbf{A} = \lambda\mathbf{A} \quad (2.21)$$

where

$$C_{kl} = \frac{1}{M}(\mathbf{V}'(t_k) \cdot \mathbf{V}'(t_l)) \quad k, l = 1, \dots, M \quad (2.22)$$

and

$$\mathbf{A} = (A_1, A_2, \dots, A_M)^T \quad (2.23)$$

The eigenvectors of the matrix \mathbf{C} are M -dimensional, and are used to form the eigenvectors of the correlation matrix \mathbf{R} via relation (2.19). The method of snapshots makes numerical calculation of the eigenvectors of \mathbf{R} easier if $M \ll 2P$.

For periodic flow, care must be taken to ensure that the snapshots are selected from an exact multiple of the flow period. Otherwise the correlation will change depending on the first and last points considered. Analysis of more than one period of oscillation represents a surplus of information. If a non-integer number of periods is analysed, then the structures or modes developed will be biased to one particular phase of the flow. The extension of the POD to true non-stationary flow is presented in a later section.

The construction of the eigenvectors, or modes, that characterize the flow does not rely directly on the spatial resolution of the velocity field; the number of measured points only features in the calculation of the inner product of (2.22). As long as the spatial resolution is sufficient to capture the significant features of the flow, an increase in the spatial resolution does not change the number of modes to any significant degree. The spatial resolution affects only the 'smoothness' of the modes[36].

2.3.2 Reconstruction of the Velocity Field

At any time, the velocity field can be reconstructed approximately from a *linear* combination of the mean flow and a finite number of modes.

$$\mathbf{V}(t) \approx \bar{\mathbf{V}} + \sum_{i=1}^M A_i(t) \boldsymbol{\psi}_i \quad (2.24)$$

where the modal amplitude

$$A_i(t) = (\boldsymbol{\psi}_i \cdot \mathbf{V}'(t)) \quad (2.25)$$

The k 'th eigenvalue can be written (from the maximization problem (2.13)) as

$$\lambda_k = E\{(\boldsymbol{\psi}_k \cdot \mathbf{V}'(t))^2\} \quad (2.26)$$

and for the approximate correlation of (2.18),

$$\lambda_k = \frac{1}{M} \sum_{i=1}^M (\boldsymbol{\psi}_k \cdot \mathbf{V}'(t_i))^2 \quad (2.27)$$

The eigenvalue has units of the square of velocity, and is proportional to the mean kinetic energy of each corresponding mode. The sum of the eigenvectors is therefore proportional to the mean energy of the fluctuating velocity field[32]. The convergence of the decomposition is optimally fast since the coefficients $A_i(t)$ of the expansion are maximized in a mean square sense. If the eigenvalues are arranged so that $\lambda_M < \lambda_{M-1} < \dots < \lambda_2 < \lambda_1$, and the velocity field is reconstructed using only the modes corresponding to the N largest eigenvalues, then the proper orthogonal decomposition captures more of the flow kinetic energy for a given N than any other expansion[31].

A truncated approximation, where $N < M$ modes are retained, acts as a noise filter: noise, and its associated small scale and energy, is neglected along with the smaller POD modes [44]. In practice, for laminar wakes, only a few modes (compared to the number of snapshots) need to be retained for an adequate description of the velocity field; for turbulent flows the energy of the modes is more distributed and a greater proportion of modes needs to be retained.

2.4 Low-dimensional Description of

Non-stationary Flow

The effects of time dependent interior forcing (or an active control input) on the structure and form of either local attractors or approximate inertial manifolds are of interest within the context of flow control. Approximate or exact inertial forms exist for the Navier-Stokes equations with a *time-independent* forcing and suitable boundary conditions. Whether these manifolds continue to exist for time-forced (or controlled) flows is a more difficult question. Physical evidence supports the idea that at least periodically forced, absolutely unstable flows can be regarded as low-dimensional. For example, a relatively small number of characteristic spatial structures are observed in experimental periodically forced vortex streets [9] (for example, twelve spatial modes have been observed during large amplitude acoustic excitation of a cylinder wake [9]; alternatively, three spatial interaction modes have been observed behind a cylinder with an oscillating aerofoil in the near wake [19]). However, the theory of approximate inertial manifolds is not necessarily applicable to cases where the forcing is time-dependent. Systems of this kind might not possess a global attractor. For an approximate inertial manifold to exist, the time derivative of the small spatial scales, $|\dot{\mathbf{q}}|$, has to be small enough compared to all other terms in the evolution equation for \mathbf{q} . This can be true only if the forcing is not too oscillatory in time, and if $f(t)$ is uniformly bounded in time ($t > 0, |f(t)| < \infty, f(\infty) < \infty$) or if $f(t)$ is periodic. Given these restrictions on the forcing function, it is sometimes possible to obtain a global attractor for the system such that the solution of the flow, $\mathbf{u}(t)$, approaches a thin neighbourhood of the manifold [28]

$$M(t) =: \text{graph} \phi(\mathbf{p}(t), Q_m f(t)) \quad (2.28)$$

Periodic or nearly periodic forcing is a reasonable condition for the control of periodic flow oscillations occurring in absolutely unstable flows. Also, only very small forces

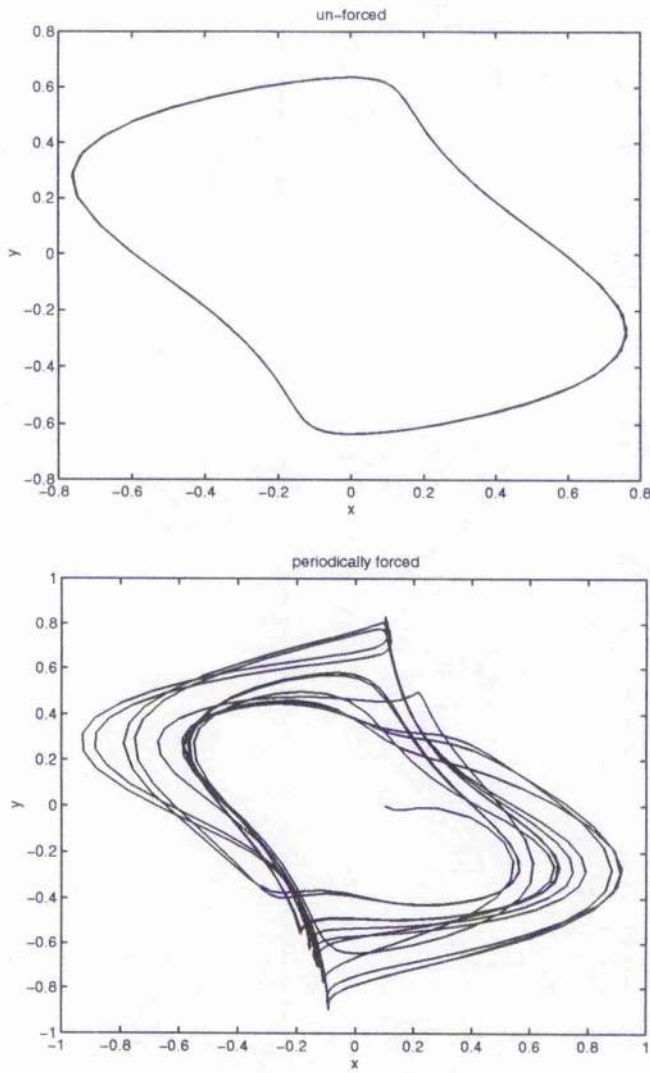
are likely to be needed for control of an initially linear absolute instability (with an exponential growth rate) and the physics of a control actuator assure that the control is uniformly bounded [24]— the use of approximate inertial manifolds for absolutely unstable wake flows with time-dependent forcing is therefore encouraging.

Many absolutely unstable flows, such as wake flows, have characteristics similar to those of non-linear oscillators. For example, the growth of temporal oscillations resulting from vortex shedding behind a circular cylinder have been modelled by the Landau equation and by equations of the Van der Pol type [10]. The oscillations in the spatial structures of the wake are seen to be reflected in the temporal response of the wake[9] and the variation in spatial structures has been modelled successfully by low-dimensional equations similar to those which model the temporal response [43][39]. The circular cylinder example provides a useful prototype for other absolutely unstable flows. The dynamics of the *forced* cylinder wake are also readily compared to some of the features of non-linear dynamical systems[23]. The behaviour of forced non-linear oscillators, determined from the theory of non-linear dynamical systems, may therefore provide some insight into the possible effects of forcing on the structure of attractors or approximate inertial manifolds of certain forced, absolutely unstable fluid flows. For the cylinder case, the amplitude of flow oscillations is a measure of the coupling between the imposed forcing frequency and the natural shedding frequency; forcing causes lock-in and non-lock-in states when applied above a certain threshold amplitude. A useful simplification of forced oscillators with two competing frequencies is the forced sine-circle map

$$\theta_{n+1} = \theta_n + \frac{K}{2\pi} \sin 2\pi\theta_n + \Omega \quad (2.29)$$

The sinusoidal term represents the effect of periodic forcing with amplitude K and the ratio of the two competing frequencies is represented by Ω . Indeed, the response of the forced cylinder wake has been shown, experimentally, to be very similar to the forced sine-circle map [23]. For values of $K > 1$ the circle map is *folded onto itself* and

chaotic behaviour may result. Very complex or chaotic behaviour is observed in the cylinder wake during forcing at some amplitudes [23]. Also, it has long been observed that the transient response of absolutely unstable fluid flows, before the flow settles on one of the two competing frequencies, can be very complex or seemingly chaotic. The associated changes in structure of the attractor of a continuous time non-linear oscillator undergoing periodic forcing, which exhibits similar behaviour to the circle map and the periodically forced cylinder flow, is suggested by an examination of the Birkhoff-Shaw attractor (adapted from [45]). This attractor is an analogue to the Van der Pol equations and has similar topology to the forced sine circle map for $K > 1$ [45]. The attractor of this system has an interesting topology that is significantly affected by the periodic forcing term. Although the Birkhoff-Shaw attractor is an example of chaotic response (and, as such, is an extreme example of the effects of forcing), this observation may suggest how the attractors for some fluid systems may change with forcing, and what implications this may have for low-dimensional characterization. When the forcing function of the B-S system is omitted (made zero), the attractor can be represented as a two dimensional limit-cycle in the $x - y$ plane. However, when the forcing is as presented in figure 2.1 the solution of the system is more complex and seemingly disordered or erratic. The regular structure of the attractor is now *not visible* from an examination of the $x - y$ plane alone, suggesting that this is no longer a complete phase space. Both views are shown in figure 2.1. The attractor of the forced phase space can be viewed using a three dimensional phase space in which the third axis is the angle, ϕ , in the forcing cycle. A sketch of the structure of the resulting attractor in three dimensional phase space, (x, y, ϕ) , is shown in figure 2.2 [45]. The figure shows that the periodic forcing introduces significant changes in the structure of the attractor (if no forcing were present the attractor would be exactly cylindrical in (x, y, ϕ) space). Folding and twisting of the attractor surface is introduced. The equations in figure 2.1 are repeated exactly at $\phi = \phi_0 + 2\pi$. Hence the three dimensional object



The Birkhoff Shaw attractor has similar topology to the forced sine circle map, which has similarities to the periodically forced circular cylinder wake,

$$\dot{x} = 0.7y + 10x(0.1 - y^2)$$

$$\dot{y} = x + f$$

The forcing term is

$$f = 0.25 \sin(1.57t) = 0.25 \sin(\phi)$$

Figure 2.1: Unforced and forced phase portraits of the B-S system

of 2.2 can alternatively have its two 'ends' at $\phi = 0$ and $\phi = 2\pi$ joined together and the attractor imagined as a torus whose surface is stretched and folded by the addition of forcing. If no forcing were present the attractor could be imagined as a

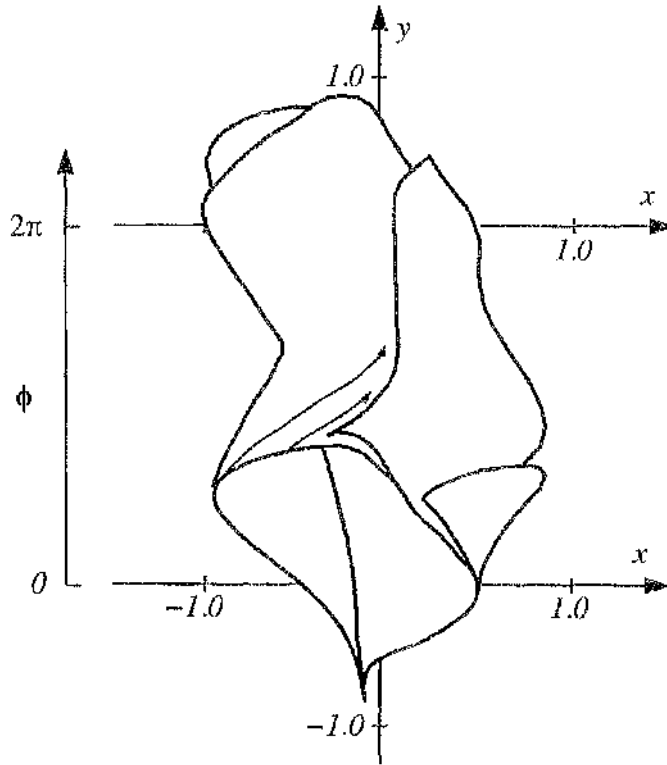


(figure adapted from [45])

Figure 2.2: Twisting and folding of B-S attractor by periodic forcing

smooth torus with no twists or folds. If the surface of the smooth, unforced torus was 'unwrapped' to form a plane with axes ϕ and θ (where θ is the angular position measured in a clockwise direction from the x axis), then trajectories starting at any particular initial condition could be traced out: each trajectory would be separate from every other and trajectories would remain a fixed 'distance' from each other. Because the surface of the torus is smooth there would be no crossing or bundling of trajectories. Unwrapped trajectories of the forced torus are shown in figure 2.3 [45]. Because of the stretching and folding of the object in figure 2.2, which is truly three

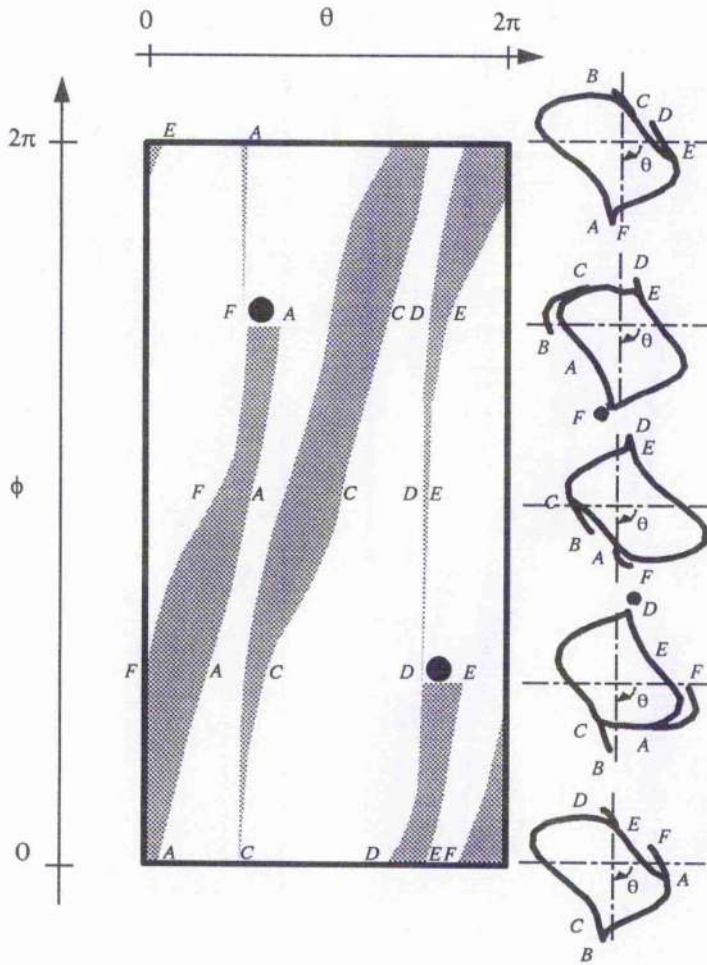


(figure adapted from [45])

Figure 2.3: Stretching and bundling of trajectories by periodic forcing

dimensional, the trajectories (in any projection) cannot be guaranteed not to cross. The stretching, bundling and apparent crossing of trajectories is shown in figure 2.3. The shaded areas are regions where the surface of the torus overlaps other regions. Repeated stretching and twisting and folding of the surface of the forced attractor causes mixing of the trajectories.

The above analogies from the theory of non-linear oscillators suggest that the effect of forcing on the limit cycle attractor for a globally unstable fluid wake is to stretch and twist the original attractor and that further dimensions in phase space are, in general, needed to view these twists. The regions of high curvature or twisting caused by forcing can be identified with fluid flow structures that appear abruptly, move or collide, or disappear. These spatial structures will therefore be statistically non-stationary and difficult to capture using orthogonal decomposition [29]. If the short lived structures are determined using the classical orthogonal decomposition, then, because each structure contributes little to the total flow energy averaged over all flow measurements, each short lived structure will have a small eigenvalue and be ignored in any truncated approximation of the velocity field [29]. It is therefore important to extend the orthogonal decomposition for non-stationary flows. Most fluid wakes are not deterministically chaotic, so a large collection of transients, in which a significant region of phase space is visited, is needed for the characterization ensemble.

2.5 Sub-optimal Decomposition of Non-stationary Flow

A time series of M ‘snapshots’ of the flow velocity field is used to form the correlation matrix in classical proper orthogonal decomposition. However, if the time series of interest is of a statistically non-stationary process (for example a flow subject to time-varying forcing) then statistical properties such as the correlation depend on

the first and final time points in the series. The variation in spatial features resulting from the non-stationary process is embodied in changes in the correlation that depend on the examined time series of snapshots. One approach to characterizing a non-stationary flow is to select structures (ie. examine the correlations) from velocity fields close to some pre-selected phase of the flow [36]. If various phases of the flow are examined as, say, structures are advected downstream, then a series of time-dependent modes can be constructed. In order, however, to keep the characterization simple, and hopefully use it within a control scheme, it is preferable to search for a *fixed* set of modes that will characterize the varying set of features found in a non-stationary flow. The spatial features occurring in non-stationary flows are approximated from an examination of the correlations of a set of transient time series [31] [44].

A snapshot of the fluctuating flow field, represented as a row vector, is

$$\phi^{ij} = [v^i(\mathbf{x}_1, t_j), v^i(\mathbf{x}_2, t_j), \dots, v^i(\mathbf{x}_P, t_j)] \quad (2.30a)$$

with the fluctuating local velocity vector,

$$\mathbf{v}^i(\mathbf{x}_k, t_j) = [v_x(x_k, y_k, t_j), v_y(x_k, y_k, t_j)] \quad (2.30b)$$

Here, i is the index pertaining to a particular snapshot time series, and j represents the time point within each series. Each snapshot has $2P$ elements (for two-dimensional flow, measured at P discrete points). The snapshots arranged into a time series of M time points form

$$\Phi^i = \begin{bmatrix} \phi^{i1} \\ \phi^{i2} \\ \vdots \\ \phi^{iM} \end{bmatrix} \quad (2.31)$$

Each time series Φ^i has zero mean, because the time average flow, for that particular time series, is subtracted prior to analysis. Only flows where the mean flow is

not significantly affected by forcing (and is therefore not modified) are considered: the same time average approximates the time average for each time series. If N disjoint snapshot time series are examined, then the matrices $\Phi^i, i = 1, \dots, N$ form a concatenated matrix,

$$\Delta = \begin{bmatrix} \Phi^1 \\ \Phi^2 \\ \vdots \\ \Phi^N \end{bmatrix} \quad (2.32)$$

The concatenated matrix of data contains all of the spatio-temporal information from the N different, M time point series of snapshots. (It should be noted that each series contains the same number of snapshots-- an intelligent choice of first and last points in the series might be, for example, the start and finish points of one period of a forcing cycle because no further information is gained from analysis of further forcing cycles. This is illustrated by the repeating structure of the twisted three-dimensional attractor depicted in figure 2.2.) To preserve as much information as possible (particularly phase dependent information), the data is *not* averaged over the N time series.

As in the classical POD approach, the correlation matrix for a single time series is formed from,

$$\mathbf{R} = \frac{1}{M} \Phi^T \Phi \quad (2.33)$$

If all of the N time series are to be analysed, then (without averaging the data) the correlation is formed in a similar way from the concatenated data matrix [31] [44],

$$\mathbf{R} = \frac{1}{M} \frac{1}{N} \Delta^T \Delta \quad (2.34)$$

Each element of the correlation formed from the concatenated data is of the form,

$$R_{kl} = \frac{1}{MN} \sum_{i=1}^N \sum_{j=1}^M \phi_k^{ij} \phi_l^{ij} \quad (2.35)$$

The correlation formed from the concatenated data matrix is thus the *average of the correlations from each distinct time series of snapshots* [31].

As before, an orthonormal set of modes that characterizes the flow is obtained by solution of the correlation matrix eigenproblem. However, the correlation \mathbf{R} is of dimension $(2P)^2$ (for two-dimensional flows measured at P points in space). If P is large, the solution of the eigenproblem is (numerically) difficult, but is made easier by adapting the method of ‘snapshots’.

The correlation developed from a concatenation of time series data is an average of the correlation matrices for each time series,

$$\mathbf{R} = \frac{1}{N}[\mathbf{R}^1 + \mathbf{R}^2 + \dots + \mathbf{R}^N] \quad (2.36)$$

Thus,

$$\mathbf{R} = \frac{1}{MN} [\phi^{11T} \phi^{11} + \dots + \phi^{1M^T} \phi^{1M} + \phi^{21^T} \phi^{21} + \dots + \phi^{N1^T} \phi^{N1} + \dots + \phi^{NM^T} \phi^{NM}] \quad (2.37)$$

For the purpose of exposition, the snapshots ϕ^{ij} are re-labelled,

$$\phi^{ij} = \varphi_k \quad (2.38a)$$

$$k = 1, \dots, K \quad k = j + (i - 1)M \quad (2.38b)$$

with $K = MN$. This allows the correlation to be re-expressed as

$$\mathbf{R} = \frac{1}{K} [\varphi_1^T \varphi_1 + \varphi_2^T \varphi_2 + \dots + \varphi_K^T \varphi_K] \quad (2.39)$$

The matrix \mathbf{R} is non-negative, symmetric and formed from K distinct snapshots, and is similar in form to the approximate correlation (2.18) and as such, its eigenvectors are of the form

$$\psi_k = \sum_{i=1}^K A_i^k \varphi_i \quad (2.40)$$

Substitution of (2.40) into the correlation matrix eigenproblem results in the system,

$$\mathbf{CA} = \lambda \mathbf{A} \quad (2.41)$$

$$C_{mn} = \frac{1}{K} (\varphi_m \cdot \varphi_n) \quad (2.42)$$

$$\mathbf{A} = (A_1, A_2, \dots, A_K) \quad (2.43)$$

The solution of this eigenproblem (which is of order $K = MN$) is used to form the eigenvectors using relation (2.40). The method is useful if $K \ll 2P$. The analysis

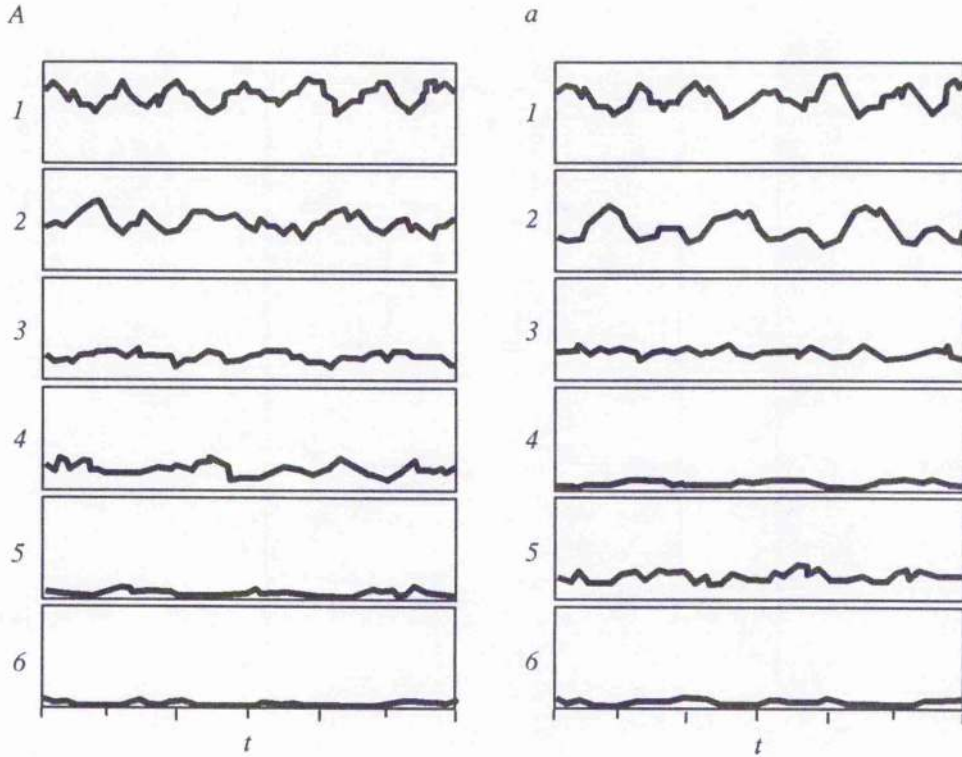


(figure adapted from [31])

Figure 2.4: Superiority of concatenation approach

of non-stationary flows therefore proceeds in the same way as the original method of snapshots. The only difference is that the non-stationary modes are sub-optimal; more of them are needed to characterize any given time series than would be needed by the classical POD [31]. Care must be exerted with the selection of time series and their sampling; however, the method of snapshots and the concatenation approach are essentially identical [31].

It is useful to compare the eigenvectors formed from the concatenation method with eigenvectors created from data averaged over all N time series (so that the

data consists of a single time series of snapshots). It can be expected that phase information will be lost in the averaging process and that the concatenation approach is to be preferred. In this respect, the results of [31] are illuminating. The modal coefficients (time varying amplitudes) of modes generated with data from a periodically forced, plane mixing layer are shown in figure 2.4 [31]. Two different sets of coefficient histories are shown. On the left, the first six coefficients calculated with concatenated data are presented (A_i 's in the figure). As expected, the modal amplitude coefficients decrease monotonically. This makes them useful in a truncated velocity field expansion like (2.24). Modes calculated using averaged data are shown on the right of figure 2.4 (a_i 's). Although these modal coefficients have a decreasing trend, coefficient a_5 is greater in amplitude, on average, than mode coefficient a_4 . This is undesirable if the modes are to be used in a truncated approximation of the velocity field as in (2.24). In general, it can be assumed that averaging of the data, over a selection of time series, causes a loss of information and that modes calculated from averaged data will be difficult to use in approximations of the velocity field.

It is also useful to consider how many different forcing regimes (and therefore how many separate, forced time series) are necessary for an adequate characterization of the flow. The number of required time series depends (obviously) on the behaviour of the flow of interest. The circular cylinder wake is an archetypal absolutely unstable flow, so the response of the cylinder wake to forcing gives a general indication of the number of different forcing regimes necessary for characterization of non-linear oscillating wakes. Experimentally, the periodically forced vortex street displays at least twelve qualitatively different arrangements of wake vortices [9]. Presumably, a time series representing at least one example of each of these qualitatively different wake arrangements would be necessary for a complete characterization. Modes considered from data deficient in one of the wake types would probably be unable to reconstruct the velocity fields for that particular forcing regime. In general, the number of examined time series will be proportional to the number of qualitatively

different wake types found under forcing. The number of time points considered within each series depends on the spatio-temporal complexity of each time series. Spatial characterization of a periodically forced mixing layer [31] shows that the degree of mode similarity, for varying numbers of time series and forcing regimes, does not differ too much for the flow— as long as snapshots from a full forcing period are examined. Figure 2.5 shows a measure of the mode-set similarity for a forced mixing layer [31]. The surface in the figure represents changes in the variable

$$C_1 = \frac{1}{I} \sum_{i=1}^I \frac{1}{(1 + |1 - p_{i,n}|)(1 + |1 - \psi_{i,n} \cdot \psi_{i,N}|)} \quad (2.44a)$$

$$p_{i,n} = \frac{A_{i,n}}{A_{i,N}} \quad (2.44b)$$

which represents the degree of similarity between the mode shapes and coefficients of the I most energetic modes when $n < N$ different time series of snapshots are considered. The figure shows that, at least for the forced mixing layer, only a small number of time series are needed to provide a considerable degree of eigenset similarity. The modes generated from a deficient data ensemble are not as good at characterizing the entire ensemble as a full data set, but they still provide a reasonable approximation. This observation is encouraging if the results are analogous to other flows (data from only a few transients are necessary for adequate characterization of the low Reynolds number cylinder wake [39]). It is also known that a reasonably small number (~ 64) of orthogonal Fourier modes that are scaled with Reynolds number can characterize the spatial features of a cylinder vortex street for a range of Reynolds numbers, capturing the initial onset of vortex shedding and changes in the vortex street structure with increasing Re [43]. It is therefore reasonable to assert that a finite representation of the wake by sub-optimal POD modes generated from a large enough non-stationary data ensemble is possible. The number of different forcing regimes and the temporal sampling necessary for adequate characterization is, however, dependent on the particular flow and can be resolved only by experimentation.

When considering the number of time-series required for complete characterization of the flow (rather than just one set of observed phenomena), the type of forcing is also of interest. As mentioned previously, an approximate inertial form of the periodically forced flow equations is valid [28]. A comparison between the effects of harmonic and an-harmonic forcing for a plane mixing layer [31] shows that the wake structures do not significantly differ between the two forcing regimes. Therefore, modes developed from one forcing regime are useful for other types of forcing, such as feedback [31] (the behaviour of forced cylinder wakes is also relatively insensitive to the exact character of forcing [7] [9]). For this statement to apply generally, more experimental evidence is required, but the similarity of the modes generated during two different forcing regimes of the mixing layer is encouraging.

2.6 Utility of the POD Modes

The POD basis represents a powerful tool for the characterization of a flow— each POD mode necessarily satisfies the flow boundary conditions and the incompressibility condition. The POD modes represent the smallest linear sub-space capable of representing, with an arbitrary degree of approximation, the *observed* phenomena. Care must therefore be taken to ensure that the observations of the flow that make up the characterization ensemble are representative of a region of the global attractor and the surrounding phase space. As most of the absolutely unstable flows of interest are not deterministically chaotic, then the characterization ensemble must be selected from a transient time series in order that a large enough region of the attractor and its surround is visited. If the characterization ensemble is formed from a large enough number of transients, then the POD modes will span the region of phase space where the solution of the flow is statistically most likely to be found. This region can be identified with a finite-dimensional ellipsoid that encapsulates the flow attractor.

High energy modes can be associated with large scale spatial structures— as the mode index increases the size of the spatial components of each structure diminishes [36] [39]. The space spanned by the largest POD modes is therefore analogous to the finite sub-space, spanned by the eigenvectors of the linear dissipation operator, that is used in the inertial manifold reduction — both sets of eigenvectors span the subspace representative of the large scale spatial structures in the flow. The modes of the POD approach can be truncated to any desired accuracy (or level of retained kinetic energy). In this case, ‘directions’ in phase space that are small enough are ignored and so the POD approximation is analogous to the flat manifold approximation where $\phi_{u,pp} = 0$. This model is simple, but often results in good practical models for the representation of certain flows [28]. If the flat approximation does not adequately represent the dynamics, then the POD approach, because of its similarity to the inertial manifold approach, can be modified so that the small spatial scales, represented by the low energy modes, are re-expressed as approximate algebraic functions of the large scales (the high energy POD modes) [37] [46]. If the orthogonal projection onto the span of the first m POD modes $\{\psi_i\}_{i=1}^m$ is denoted by P and the complementary projection is $Q = I - P$, then the original flow equation is of the form,

$$\dot{\mathbf{u}} = F(\mathbf{u}) \quad (2.45)$$

$$\mathbf{u}(t) = \mathbf{p}(t) + \mathbf{q}(t) \quad (2.46)$$

where

$$\dot{\mathbf{p}} = PF(\mathbf{p} + \mathbf{q}) \quad (2.47a)$$

$$\dot{\mathbf{q}} = QF(\mathbf{p} + \mathbf{q}) \quad (2.47b)$$

An approximate ‘inertial form’ of the equations is thus

$$\dot{\mathbf{p}} = PF(\mathbf{p} + \phi(\mathbf{p})) \quad (2.48)$$

The unknown function $\mathbf{q} = \phi(\mathbf{p})$ is approximated by a solution of

$$0 = QF(\mathbf{p} + \mathbf{q}) \quad (2.49)$$

Equation (2.49) assumes that $\dot{\mathbf{q}}$ can be ignored. This assumption is valid for unforced statistically stationary flows—the low energy modes correspond to small scale structures which typically have a faster time scale than the large scale structures [37]. The result of this faster time scale is that the large scale components are not influenced by variations in the small scales and hence $\dot{\mathbf{q}}$ can be ignored [37]. For time dependent forcing, however, $\dot{\mathbf{q}}$ cannot always be ignored. The value of $|\dot{\mathbf{q}}|$ can be assumed to be small if the forcing is not too oscillatory, and is periodic [28]. The POD basis can therefore be used in a similar fashion to the inertial manifold basis. The POD basis can, however, represent only the observed phenomena, but it is often more practical than the direct inertial manifold approach.

2.7 Summary

It can be said, in general, that any two-dimensional, dissipative wake flow, which has a finite number of flow structures or vortices, can be represented by a low-dimensional system. An inertial manifold is a property of many dissipative fluid wake flows—the inertial manifold allows representation of the flow dynamics by a finite ordinary differential equation set which is a function of only the large spatial scale components of the flow. This equation set is the inertial form of the governing partial differential flow equations. Approximate inertial forms have been shown to exist for flows where an exact inertial manifold is not known to exist or is difficult to represent explicitly. Inertial forms have also been shown to exist for non-stationary, forced flows (as long as the forcing is periodic and bounded and not too oscillatory). The effect of forcing is, typically, to cause curvature or twisting of the inertial manifold—often, extra dimensions are needed to view these twists and thus encapsulate the attractor for time forced flows. It can therefore be asserted that a low-dimensional description of the dynamics of a controlled fluid wake flow is valid. Experimental evidence of low-dimensional behaviour in periodically forced flows is

also encouraging.

Explicit representation of an inertial form of the flow equations is often difficult or not available. The crudest approximation of an inertial form is to neglect completely the small scale spatial structure. It therefore seems reasonable to attempt a low-dimensional description of the wake flow by characterization of the large scale spatial structures in the wake. Such a characterization is furnished by proper orthogonal decomposition. A non-stationary velocity field can be represented by a finite number of sub-optimal, orthogonal POD modes. A low-dimensional characterization of the large scale spatial structures is achieved by neglecting the POD modes which have small energy. The POD basis captures more flow energy, for a given number of retained POD modes, than any other linear expansion. The resulting sub-optimal modes satisfy the flow boundary conditions, incorporate the effect of a control (which may include boundary or interior control), and satisfy the incompressibility condition.

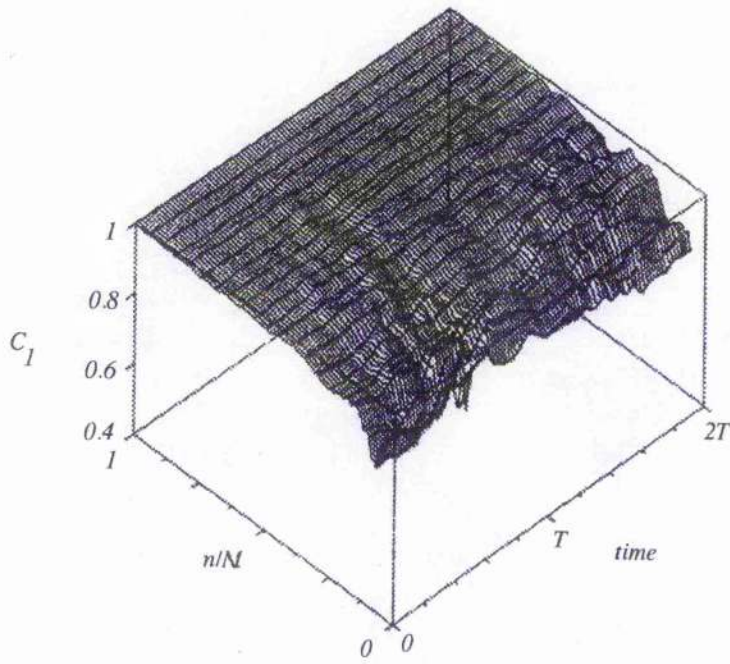


(figure adapted from [31])

Figure 2.5: Eigenset similarity with variation in the number of considered time-series

Chapter 3

Neural Control of Large Scale Wake Structures

3.1 Introduction

The success of an active, closed loop control strategy for control of an oscillating wake flow depends on whether the flow oscillations are observable. In general, flow oscillations are unobservable with a single sensor [7] and if a large number of global modes are present then multiple, spatially distributed, sensors (perhaps contained in a ‘picture’ of the flow field) are needed for control of the flow[4][19]. It is helpful if the large dimension set of information contained in a picture of the flow field is represented by a smaller set without significant loss of information— the control algorithm is thus made computationally feasible.

When large scale structures dominate the flow, the flow may be approximated by the sum of the mean (time-average) flow field and a finite number of spatial modes. The accuracy of the approximation increases as the number of retained modes in the expansion increases. The truncated approximation of the velocity field is,

$$\mathbf{V}_M = \bar{\mathbf{V}} + \sum_{i=1}^M A_i(t)\psi_i \quad (3.1)$$

Low energy modes are neglected in the truncated combination of modes.

The control problem is to provide the correct external, time-dependent control input to the flow so that the future state of the flow corresponds to a desired state. A prediction of the response of the fluid flow to an arbitrary control input is therefore helpful for the design of a control algorithm [41]. The controller is designed so that the prediction of the flow in response to an applied control input corresponds with some desired state. Controls that stabilize the unstable global modes of the flow are of interest—controls that modify the mean flow, and hence remove the region of absolute instability, are not considered because flow stabilization via modification of the mean flow can be achieved by adding extra bodies to the wake. The response of a velocity field, characterized by a finite number of modes, can be expressed as an evolution equation for the controlled mode amplitudes or as a discrete-time prediction of the future mode amplitudes given the present amplitudes and control input. This chapter presents a method for determining the response of the fluid to a control input and outlines a robust method for non-linear control of the wake flow.

3.2 Prediction of the Flow Dynamics

3.2.1 Galerkin Methods

A finite-dimensional dynamical model of the flow may be obtained from classical Galerkin approximation of the Navier-Stokes equations. The truncated expansion for the velocity field (3.1) is substituted into the Navier-Stokes equations, which are the governing partial differential equations of the flow. The Galerkin projection onto the truncated space is,

$$\left(\psi_k \cdot \left(\frac{\partial \mathbf{V}_M}{\partial t} - \mathbf{F}(\mathbf{V}_M) \right) \right) = 0 \quad k = 1, \dots, M \quad (3.2)$$

The modes are orthonormal and, by construction, incompressible and fixed in time (only the amplitudes are time dependent); and so the inner product results in a

system of M *autonomous* ordinary differential equations which approximate the evolution of the mode amplitudes. The evolution equations resulting from a linear Galerkin approximation are at most quadratic [33]; the coefficients in the equations derive from the various internal inner products in (3.3) [33][39] (a detailed formulation of these equations is presented in the appendix). The system of equations is represented, symbolically, as,

$$\frac{dA_k}{dt} = G_k(A_1, A_2, \dots, A_M) \quad k = 1, \dots, M \quad (3.3)$$

Together with an appropriate set of initial conditions, the equations (3.3) represent a succinct approximation of the dynamics of large scale structures in the unforced wake. The Galerkin procedure is presented pictorially in figure 3.1. The figure shows the projection of a solution, restricted to a curved manifold, onto the flat space spanned by two of the largest POD modes (ψ_n and ψ_l). The neglected mode represented by ψ_c contains the curvature of the manifold.

The standard Galerkin approximation assumes that the small scales of the flow, represented by the neglected POD modes ($\psi_{M+1}, \psi_{M+2}, \dots$), do not contribute to the dynamics of the large scale components, represented by the first M POD modes; the small scales are neglected in the finite truncation of the velocity field expansion (3.1) [27]. The Galerkin method is, therefore, analogous to a flat inertial manifold approximation where $\phi_{app} = 0$. The flat manifold approximation is inaccurate in regions of high curvature or twisting which are caused by time-dependent forcing of the flow. Therefore, the flow is approximated more accurately, and with fewer POD modes, if the small spatial scales are represented by appropriate non-trivial functions of the large scales. An approximate method for determining algebraic relationships between the largest POD modes and the smallest POD modes was outlined at the end of the third chapter (equations 2.45 – 2.49), from which a non-linear Galerkin method can be formed [37] [46].

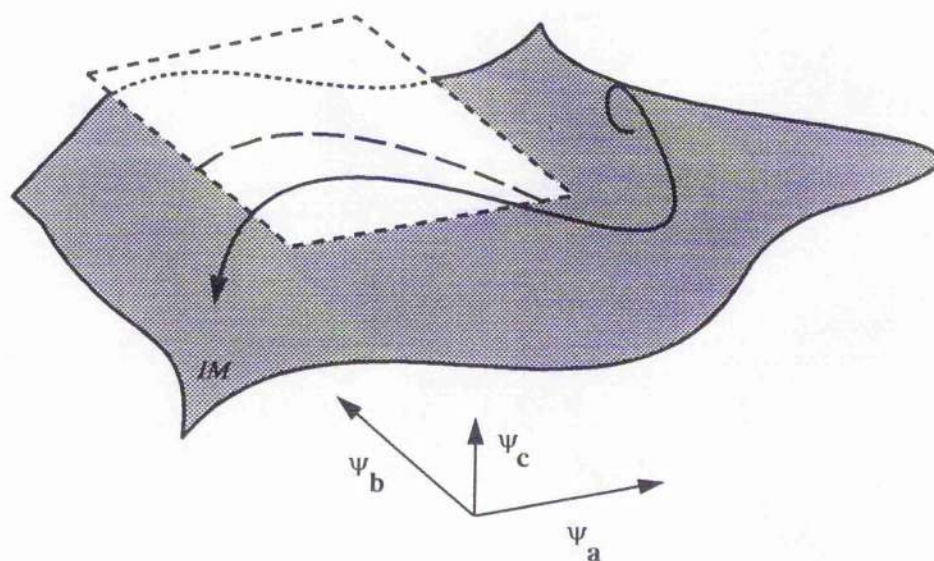


Figure 3.1: Sketch of the Galerkin Projection

However, explicit representation of a Galerkin approximation that incorporates a time-dependent, possibly multi-variable control is, in general, not possible. The general form of the evolution equation for the mode amplitudes in the presence of a control input is,

$$\frac{dA_k}{dt} = G_k^c(A_1, A_2, \dots, A_M, u_1(t), \dots, u_c(t)) \quad k = 1, \dots, M \quad (3.4)$$

The functional form of G_k^c depends implicitly on the nature of the external control input and is, in general, unknown. In particular, an analytic or approximate function which describes the spatial distribution of the effect of the control on the entire flow field is necessary so that the inner products of the Galerkin approximation can be calculated. Therefore, the Galerkin method is best suited to problems where only the qualitative response of the flow to excitation is of interest. In problems of this type, *ad hoc* control terms can be added to the autonomous equations [10][11]. The response of the model to excitation by these controls may be qualitatively correct but this method is of questionable use in the design of a control algorithm where quantitatively correct responses are needed.

3.2.2 Empirical Modelling of the Flow Dynamics

If the *observed* response of the fluid (and hence the observed mode amplitudes) to a real control input is recorded from a flow experiment, then the control-mode interaction may be estimated empirically. Empirical modelling of the response of the fluid to excitation is advantageous, because there is then *no need* to determine an exact or approximate spatio-temporal relationship that describes the interaction of the control input with every point in the flow field— all that is of interest in an empirical model is the temporal behaviour of the mode amplitudes in response to some easily defined measure of the control input (for example, values of the intensity and frequency of a vibrating source in the flow).

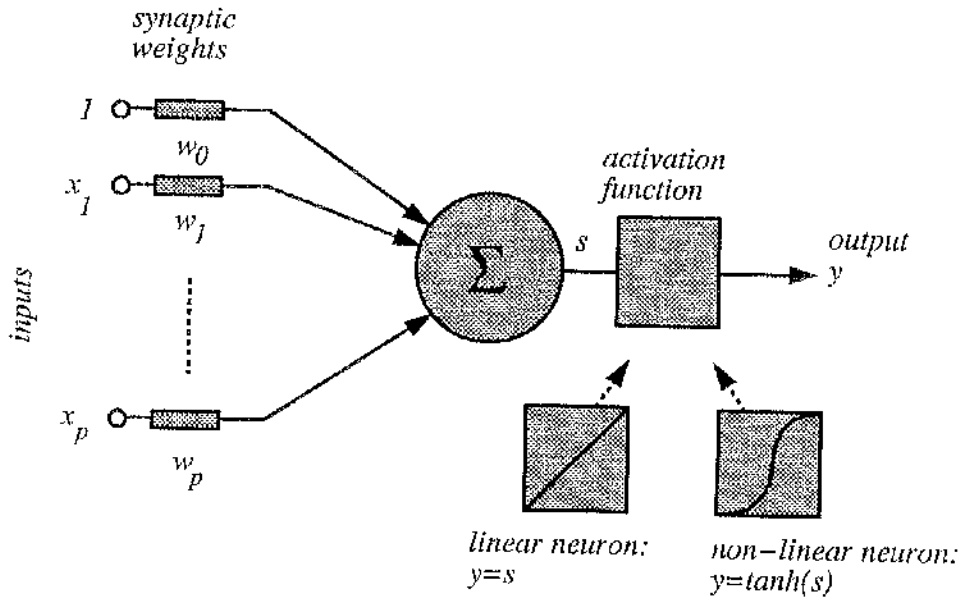
Also, it is a reasonable assumption that the small spatial scales play some part

in the dynamics of the large scales of the excited flow [28]; so any empirically derived function that approximates the *observed* dynamics of the flow, with reasonable accuracy, is more able to describe the salient dynamics than a linear Galerkin process (which completely neglects the dynamical effects of the small spatial scales). A non-linear, empirical model of the flow dynamics, estimated from *observation* of the behaviour of the large scale dynamics (the largest POD modes), is analogous to an inertial form of the flow governing equations restricted to a curved (non-linear) inertial manifold rather than the flat (linear) inertial manifold of the Galerkin scheme.

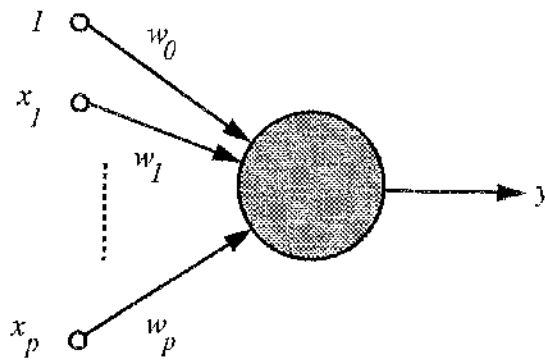
3.3 Neural Network Emulation of the Flow Dynamics

A neural network is a collection of simple processing units, or neurons, which can be constructed from weighted linear summations of inputs passed through differentiable, monotonically increasing, non-linear functions [42]. It has been shown, in a theorem due to Kolmogorov [47], that any continuous function (of any number of variables) can be computed using only linear summations and non-linear, monotonically increasing functions of one variable; a corollary is that a certain architecture of neural network can arbitrarily approximate *any* non-linear mapping that may exist between a set of input data and a set of output data [47][48]. Moreover, there exist training algorithms which recursively alter the connection weights of the network so that the network approximates the unknown functional input-output relationship by observation of an experiment. The construction of a single neuron, originally posed as a mathematical model for biological neurons or brain cells, is depicted in figure 3.2. The single neuron is, however, limited to computing simple logic functions and linear decision boundaries [47].

The neuron receives a number of inputs that are multiplied by synaptic weights which determine the connection strength of the particular input element. The



Structure of the neuron.



Symbol used to represent neurons.

Figure 3.2: Structure of Neuron Model

weighted inputs are added together with a weighted bias value and passed as an argument to an activation function. The activation function is often a sigmoidal or hyperbolic tangent function (or other step-like non linear functions), but it is sometimes pulse-like (a Gaussian bell), linear, or even a differential equation, depending on the application of interest [42]. An important property of the activation function is that it is differentiable. This property is necessary so that the neuron, as part of a network of neurons, can learn an input-output relationship via a training algorithm [42].

One type of network architecture is the multi-layer perceptron (MLP), which consists of up to three layers of neurons, or nodes, with feedforward connections between layers, but no feedback connections or lateral connections between neurons. The structure of a multi-layer perceptron is shown in figure 3.3. The network consists of a set of inputs, up to two hidden layers, and an output layer of neurons. The computational abilities of multi-layer networks are significant— a two layer MLP with an arbitrary number of nodes is capable of making arbitrarily close approximations to any non-linear function [47][48]. The number of required nodes, however, can become very large for some problems. It is economical to use three layer MLP's for approximation of some problems, as they perform much better than two layer networks— it is possible to compute any non-linear algebraic function of N variables with a three layer MLP with non-linear activation functions and $N(2N + 1)$ nodes [47]. There is no advantage gained by adding further layers to a three layer MLP. A common choice of activation function for the MLP is the hyperbolic tangent, which gives an asymmetric output ranging between plus and minus one [41]. A network with two layers of non-linear activation functions and a linear output layer is more versatile than the fully non-linear network, as its output range is not restricted [42].

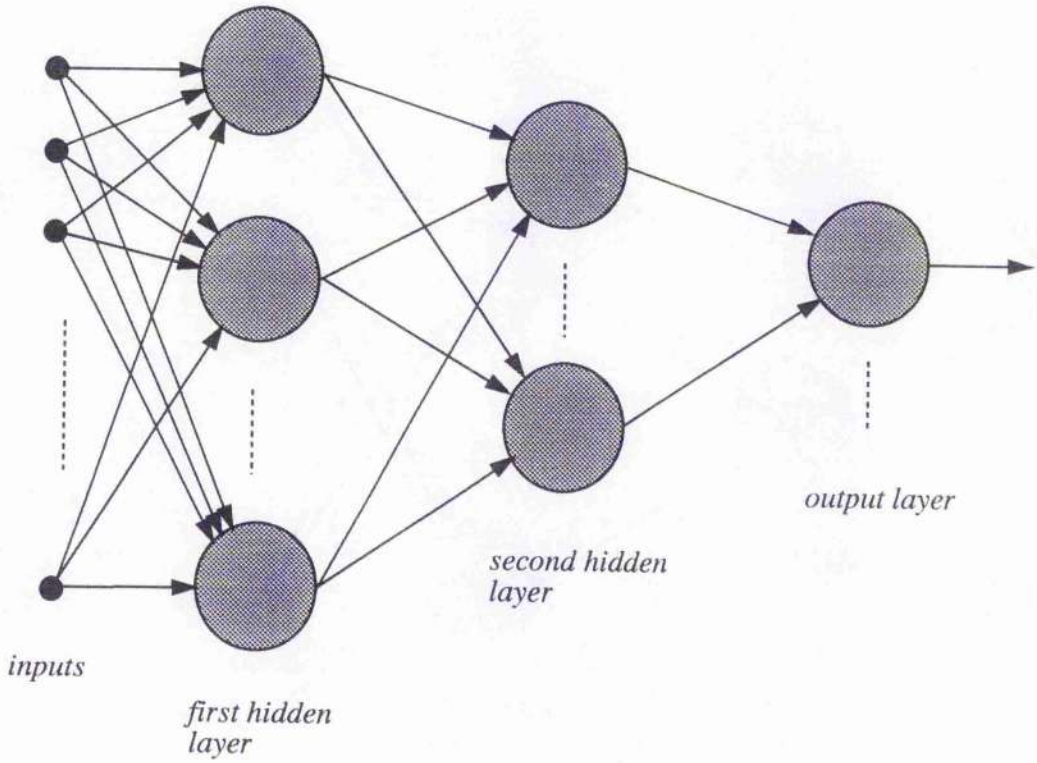


Figure 3.3: The Multi-layer Perceptron

It is possible to arrange a dynamic network which has neurons with differential or difference equations as activation functions. Dynamic networks involve feedback and lateral connections between nodes, and can be trained to emulate a differential equation and follow a trajectory. The training of such dynamic networks is, however, computationally intensive because of their inherent feedback [48]. The training of multi-layer perceptrons is much less intensive, but the multi-layer perceptron is a *static* network and can be trained to approximate only algebraic mappings. To emulate the mode amplitude evolution with a static network, the reduced-order flow model (3.4) is represented by an equivalent discrete-time process described by a non-linear regressive model of order p [48],

$$\mathbf{A}(n+1) = \Gamma(\mathbf{A}(n), \mathbf{A}(n-1), \dots, \mathbf{A}(n-p), \mathbf{u}(n), \dots, \mathbf{u}(n-p)) \quad (3.5)$$

where $\mathbf{A}(n) = (A_1(n), A_2(n), \dots, A_M(n))$ and the control parameters are $\mathbf{u}(n) = (u_1(n), u_2(n), \dots, u_c(n))$. The output of the static network, trained to approximate the mapping (3.5), is delayed and fed back to the network input, and the network output follows a discrete-time trajectory and behaves in a similar way to a dynamical system. However, small errors in the network approximation of the mapping (3.5) accumulate after each time-step, so that the discrete-time trajectory of the network output soon differs from that of the actual system (which is governed by a continuous-time differential equation). The relationship between present and past system states, and the future (one-step) state, is, however, predicted accurately if the network is continually supplied with the *actual* present and past system states. The neural emulator then has the form of a one-step predictor,

$$\hat{\mathbf{A}}(n+1) = \hat{\Gamma}(\mathbf{A}(n), \mathbf{A}(n-1), \dots, \mathbf{A}(n-p), \mathbf{u}(n), \dots, \mathbf{u}(n-p)) \quad (3.6)$$

which is trained to minimize the magnitude of the error vector

$$\mathbf{e} = (\mathbf{A}(n+1) - \hat{\mathbf{A}}(n+1)) \quad (3.7)$$

Error values do not accumulate, because there is no feedback in the static network, and so the network can be trained to provide a very accurate prediction of the future

fluid state. A multi-layer perceptron, used as a one-step predictor, to emulate the non-linear response of the fluid to a control input is shown schematically in figure 3.4. The network is trained by recursive adjustment of the synaptic weights or connection strengths by the *backpropagation algorithm*, which is an error gradient descent technique designed to minimize the mean squared error of the output [42] [48]. The local error gradient at each node of the network is computed by backpropagation of the network error from the output (where the error is the difference between the actual and the desired network response) back to the input. The weights are updated via the learning rule

$$\Delta w_{lji}(n) = \eta \times \delta_j(n) \times y_{l-1,i}(n) \quad (3.8)$$

where $w_{lji}(n)$ is the synaptic weight of the i 'th input to neuron j in layer l at the n 'th iteration, $y_{l-1,i}(n)$ is the input to the neuron, and η is the learning rate parameter. The learning rate is necessarily small for stability. Within each neuron j in layer l , the internal activity is

$$s_{lj}(n) = \sum_{i=0}^{P_{l-1}} w_{lji}(n) y_{l-1,i}(n) \quad (3.9)$$

where layer $l = 0$ is the input layer, and $y_{l-1,0}$ is a constant bias level ($= 1$). P_{l-1} is the number of inputs to layer l . The output of each neuron depends on the activation function used,

$$y_{lj} = \tanh(s_{lj}(n)) \quad (3.10a)$$

for non-linear neurons in the hidden layers, or

$$y_{lj} = s_{lj}(n) \quad (3.10b)$$

for linear neurons, which are sometimes used in the output layer. The entire network output is trained to predict the actual flow response to a control input. The network

input,

$$\begin{bmatrix} A_1(n) \\ A_2(n) \\ \vdots \\ A_M(n) \\ u_1(n) \\ \vdots \\ u_c(n) \end{bmatrix} \quad (3.11)$$

for a control input described by c parameters, together with as many past input values as desired, is fed forward through the network to the output, which approximates the future flow state,

$$y_{L,j}(n) = \hat{A}_j(n+1) \quad (3.12)$$

where L is the output layer of the network. The desired network outputs are the actual mode amplitudes at the next time step,

$$d_j(n) = A_j(n+1) \quad (3.13)$$

Hence the network error is

$$e_j(n) = (d_j(n) - y_{L,j}(n)) = (A_j(n+1) - \hat{A}_j(n+1)) \quad (3.14)$$

The local gradient of the error at each output node of the network is [42]

$$\delta_{L,j}(n) = e_j(n) f'(s_{L,j}(n)) \quad (3.15)$$

where $f'(s)$ is the derivative with respect to s of the output node activation function [41]. For a linear output node, the local error gradient is

$$\delta_{L,j}(n) = (d_j(n) - y_{L,j}(n)) \quad (3.16a)$$

and for a non-linear tanh output neuron, the local error gradient is [42]

$$\delta_{L,j}(n) = (d_j(n) - y_{L,j}(n))(1 - y_{L,j}^2(n)) \quad (3.16b)$$

The local error gradient at each hidden neuron is calculated from the sum of the error gradients of all of the neurons connected to its output [42],

$$\delta_{lj}(n) = \sum_k \delta_{l+1,k}(n)w_{l+1,k,j}(n)(1 - y_{lj}^2(n)) \quad (3.16c)$$

The network weights are updated iteratively, until some minimum error level is attained. The weights are updated with the relation,

$$w_{lji}(n + 1) = w_{lji}(n) + \eta\delta_{lj}(n)y_{l-1,i}(n) \quad (3.17a)$$

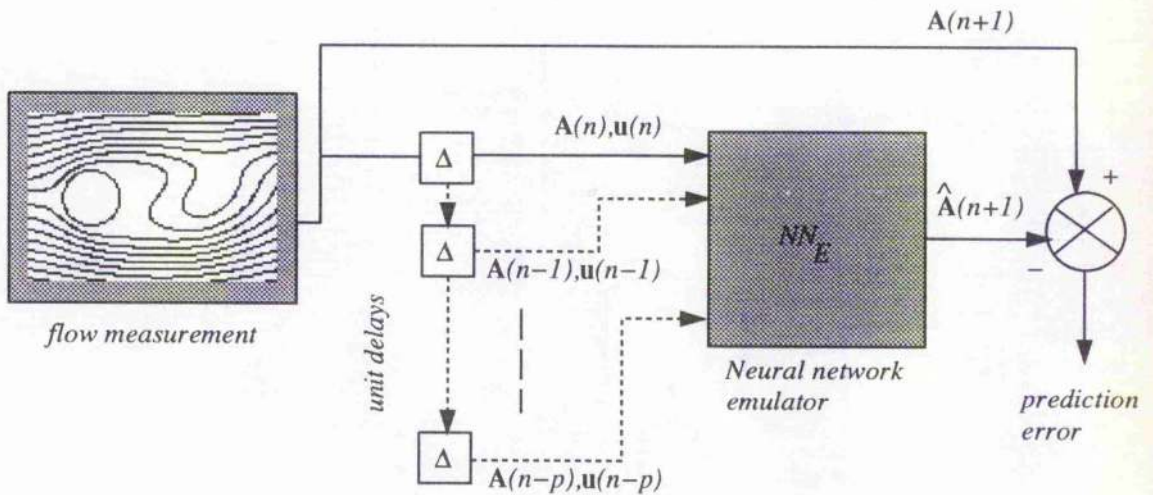


Figure 3.4: Neural Emulator: One-Step Predictor

Generalization is the ability of a neural network to extrapolate, or to provide reasonably accurate predictions, when faced with inputs which lie outwith the range of the training data. A network that achieves good generalization is able to estimate the unknown functional relationship hidden within the training data [42]. Usually, network generalization is tested by presenting the network with new data, different from the training data set, and examining the error (which should be small). The main issues involved in achieving good network generalization, and thus good estimation of the mode dynamics, involve the choice of network size and also the collection of suitable training data. The second issue is common to all methods of empirical

estimation. Transient data contains much more information than asymptotic data and is necessary for the complete resolution of the unknown function [10]. The data is, however, composed of measurements of a forced flow, and already contains many transients. As long as the forcing is adequate to excite all of the dynamics of interest, then the data ensemble will give a good representation of the underlying dynamics of the flow.

The choice of network size for approximation of a specific function is an inherently difficult task [48] which is not computable algorithmically. The size of network is important: if the network is too small, then it is unlikely to be able to form a good model of the flow response— alternatively, if the network is too large, it may be able to implement a complicated function that produces results consistent with the training data, but results in a poor approximation of the actual flow [42]. The smallest network that produces results consistent with the training data is usually the network which best approximates the underlying function hidden within the training data. If the network emulates this function accurately then the network can generalize. A number of synaptic weights of the order of the number of training samples has been suggested as an upper bound for the network size. However, the number of weights is usually much lower than this upper bound, so that the network weights do not just store or memorize the training samples [48].

The backpropagation method is a slow process, and many iterations through the training data may be necessary before the network achieves good generalization. The number of necessary training cycles to achieve an error goal is an NP-complete problem. If too many cycles are used, or if the required error criterion is too small, the network over-fits the training data and learns any noise or uncertainty in the experimental data. Over-fitting of the training data leads to poor generalization [48]. The backpropagation method is an error gradient search technique and is thus prone to entrapment in local minima, and slow progress on flat regions of the error surface. The difficulty of determining how long it takes to achieve a desired error criterion

with the backpropagation algorithm can be exposed by characterization of the error surface for a non-linear neuron [48]. Figure 3.5 shows a typical error surface for a single non-linear neuron using a tanh non-linearity and just one bias and one synaptic weight. The error surface was constructed by training the neuron to partition a set of integers into a positive subset and a negative subset. The error surface contains regions of very large gradient and regions that are very flat. The error surface for a MLP has similar characteristics, but is considerably more complex [48]. Increasing the learning rate to speed up training on flat regions of the error surface often leads to instability and violent oscillation of the synaptic weights. The learning rate is therefore kept small. Instead, progress along flat regions of the error surface is encouraged by addition of a ‘momentum’ term,

$$w_{lji}(n+1) = w_{lji}(n) + \eta \delta_{lj}(n) y_{l-1,i}(n) + \alpha(w_{lji}(n) - w_{lji}(n-1)) \quad (3.17b)$$

The momentum term sets the weight change as a weighted average of the previous weight changes, and as a result, helps progress on flat regions of the error surface [47].

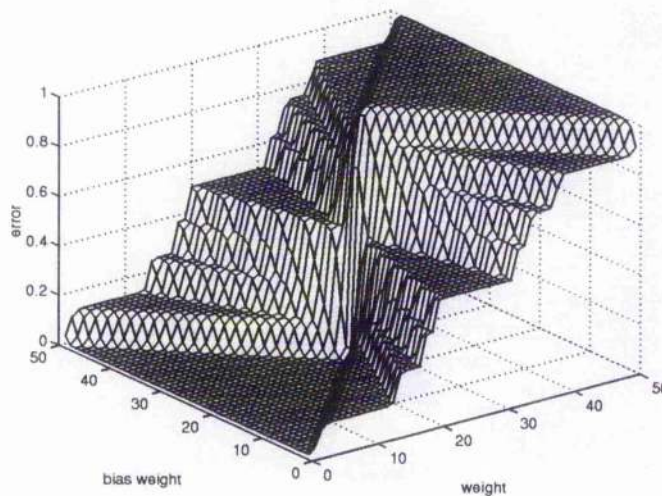


Figure 3.5: Error Surface for Single Non-linear Neuron

3.4 Neural Network Non-linear Control

The principal objective of the flow control strategy is to provide an external, time-dependent, non-linear control input to the flow, such that the future fluid state, described by a finite number of mode amplitudes, corresponds to some desired state. The neural emulator of the flow dynamics provides a prediction of the fluid state, given initial mode amplitude conditions and values for external control parameters. The predicted response of the fluid is used to design a controller, such that the predicted response to an applied control minimizes the control system error and the flow is driven towards a desired state.

If the neural emulator is fed an arbitrary control input, it will provide predicted values for the mode amplitudes at the next time-step [41].

$$\mathbf{u}(n), \mathbf{A}(n) \rightarrow \hat{\mathbf{A}}(n+1) \quad (3.18)$$

The difference between the predicted amplitudes, $\hat{\mathbf{A}}$, and the desired set of amplitudes, \mathbf{A}_d , for the control system is the *control system error vector*,

$$\mathbf{e}_{CS} = (\mathbf{A}_d(n+1) - \hat{\mathbf{A}}(n+1)) \quad (3.19)$$

This error does not, however, directly reveal the *error in the applied control*,

$$\mathbf{e}_u = (\mathbf{u}^g(n) - \mathbf{u}(n)) \quad (3.20)$$

where \mathbf{u}^g is the unknown control that would either provide a control system error of zero magnitude (the \mathbf{u}^g applied to $\mathbf{A}(n)$ such that $|(\mathbf{A}_d(n+1) - \hat{\mathbf{A}}(n+1))| = 0$), or the unknown control that would make the magnitude of the control system error less than the previous value (the \mathbf{u}^g applied to $\mathbf{A}(n)$ such that $|(\mathbf{A}_d(n+1) - \hat{\mathbf{A}}(n+1))| < |(\mathbf{A}_d(n) - \hat{\mathbf{A}}(n))|$). The error in the applied control, rather than the control system error, is necessary to adjust the control to provide the desired fluid response at the next time step [26][14].

The error in the applied control is, however, available by backpropagation of the control system error vector, through the emulator, to the control inputs because the

emulator is a neural network [26][14][41]. The control system error, backpropagated through the emulator with its weights held fixed, is used to train a controller neural network to apply a suitable control input to the flow [41]. The error gradient at a controller network output node is treated like an error gradient of an internal hidden node— as if the controller and emulator are one network [14]. The controller weights are updated by further backpropagation through the controller so that a better control input is provided at the next time step. The neural control process is shown, schematically, in figure 3.6. This type of control is very robust to external perturbations [26]— because the control algorithm (defined by the controller weights) is updated at each time step (so the control is adaptive). The control is a combination of either non-linear or linear feedback of the present mode amplitudes and a non-linear function of the control system error, depending on whether the controller network is non-linear or linear,

$$\mathbf{u}(n) = \mathbf{f}(\mathbf{A}(n)) + \mathbf{g}(\mathbf{A}(n) - \hat{\mathbf{A}}(n)) \quad (3.21)$$

where \mathbf{f} is a function of the controller network, and \mathbf{g} is a function of the emulator network. The neural control scheme, therefore provides a non-linear control that drives the fluid state towards a desired combination of mode amplitudes, without explicit modelling of the effect of the control on the flow field or recourse to complicated analytical non-linear control theory [14]. The controller does not require an inverse of the emulator mapping to exist and will drive the system state closer to the control goal irrespective of the existence of an inverse model of the flow dynamics.

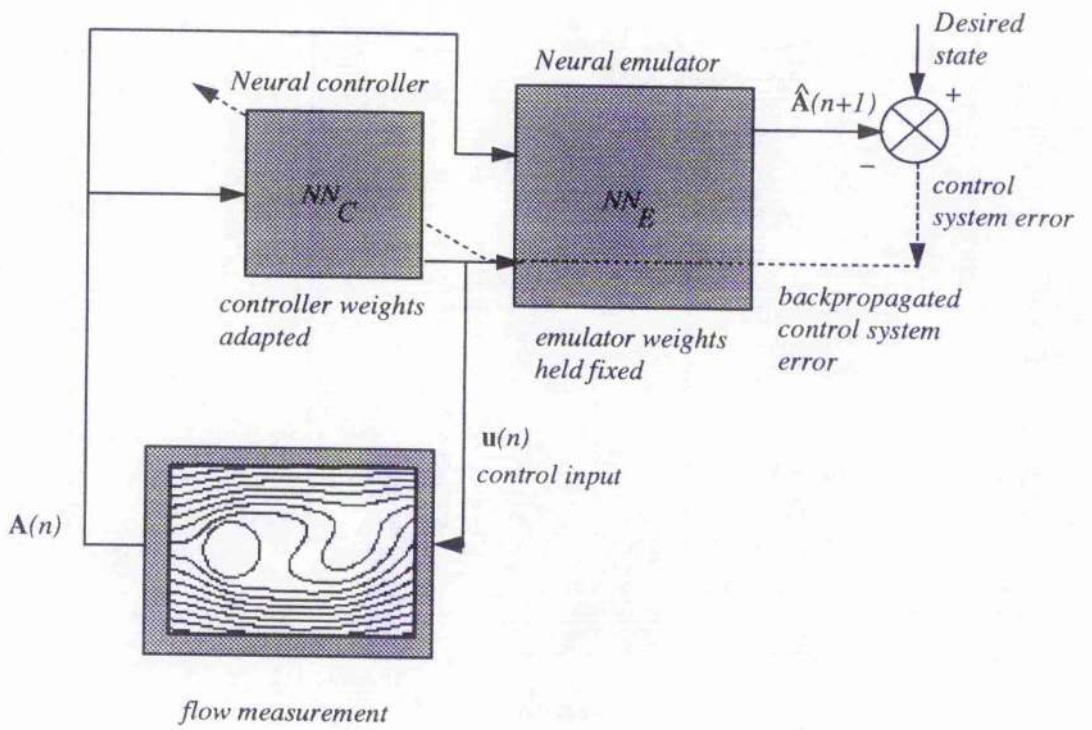


Figure 3.6: Neural Control Scheme

3.5 Neural Estimation of the POD modes

The emulation and subsequent control of the fluid flow is encapsulated within the empirical neural network framework. The extraction of the POD modes is also an empirical process, and can therefore be rearranged into a neural network format to provide continuity within the modelling and control scheme. Recursive estimation of the POD modes avoids the need for storage and calculation of a potentially large correlation matrix and also avoids the need for direct numerical calculation of the correlation eigenproblem. The POD method is a linear decomposition and can therefore be performed by a neural network consisting of only a single layer of linear neurons [47][42].

The neural network mode amplitude filter is used to extract significant patterns or features from a set of input data in a similar manner to that of proper orthogonal decomposition. The filter has no examples of mode structure available to adapt its synaptic weights; it must therefore be *self-organizing* and learn from its input environment [42]. Self-organizing networks are trained with a set of learning rules that operate locally— a change in a synaptic weight of a particular neuron only affects the immediate neighbourhood of that neuron. Repeated modification of the synaptic weights of the network by local rules can lead to global organization if the learning algorithms are constructed from a set of principles [42]

Principle 1. *Changes in the synaptic weights self-amplify.*

Principle 2. *The total sum of values of the synaptic weights is limited to some finite value. The weights therefore compete for a finite resource; growing synapses do so at the expense of others.*

Principle 3. *The growth of synapses encourages the growth of neighbouring synapses.*

The first principle, operating at a local level, ensures that the synaptic weight

is amplified by the coincidence of a strong input signal and strong post synaptic weight signal. Synaptic weights that are stimulated repeatedly by large input values therefore increase in value. This principle represents positive feedback of the external input [42]. The second principle is required to stabilize the network and represents negative feedback of the neuron output. For stability, the synaptic weights of the network must be limited to some finite value. There is therefore competition amongst the weights; increases in the strength of rapidly self-amplifying synapses are compensated by the reduction in strength of the smaller weights [42]. A single weight, by itself, is not efficient for activation of a neuron. Instead, a set of neighbouring synapses that are connected to a particular neuron are needed to successfully trigger a useful response. The growth of a particular synapse, via self-amplification, must also encourage the growth of the other synapses of the neuron despite the competition amongst synapses in the network. This local cooperation is stated in the third principle [42]. Requirements must also be made of the input data presented to the self-organizing network: there must be a redundancy of input signals or patterns [42]. Empirical estimation of spatial patterns with a self-organizing network will therefore necessitate a larger data ensemble than is necessary for the standard method of feature extraction—proper orthogonal decomposition. Apart from this requirement for a large input ensemble, a linear self-organizing network can be developed to extract the same features as proper orthogonal decomposition.

A single neuron that has its synaptic weights modified by an algorithm that follows the above three principles of self organization can learn the structure of the largest POD mode (this information is contained within the structure of the synaptic weights) and output the amplitude of the largest POD mode [42] [47]. The linear neuron output is,

$$a = \sum_{i=1}^P w_i v_i \quad (3.22)$$

The neuron input is the fluctuating flow field vector \mathbf{V}' at a discrete time n . There is the same number of synapses with weights $w_i, i = 1, \dots, P$ as the number of elements

in the flow field measurement. Using the first principle of self-organization, the synaptic weights self-amplify according to their input snapshot; $w_i(n)$ grows with the coincidence of a strong stimulus and strong output of the neuron, or alternatively, repeated $v_i(n)$.

$$w_i(n+1) = w_i(n) + \eta a(n)v_i(n) \quad i = 1, \dots, P \quad (3.23)$$

The amplification, or learning rate parameter, is η . Equation (3.23) represents continual amplification of the synaptic weights and is therefore unstable. Negative feedback of the output of the neuron is necessary, according to the second principle, for stability. Hence, the synaptic weight is normalized so that it can attain only a finite value [42] (this is equivalent to the restriction $\psi \cdot \psi = 1$ of the classical POD approach),

$$w_i(n+1) = \frac{w_i(n) + \eta a(n)v_i(n)}{\sqrt{\sum_{i=1}^P (w_i(n) + \eta a(n)v_i(n))^2}} \quad (3.24)$$

The expression for the normalized weight (3.24) can be re-expressed, for *very* small η as a power series expansion,

$$w_i(n+1) \simeq w_i(n) + \eta a(n)(v_i(n) - a(n)w_i(n)) \quad (3.25)$$

The algorithm accounts for both self-amplification of the weights, from repeated stimulation of the input, and negative feedback of the output [42]. In vector form (3.22) becomes

$$a = \mathbf{w}^T(n)\mathbf{V}'(n) = (\mathbf{w}(n) \cdot \mathbf{V}'(n)) \quad (3.26)$$

Equation (3.25) becomes

$$\mathbf{w}(n+1) = \mathbf{w}(n) + \eta(\mathbf{V}'(n)\mathbf{V}'^T(n)\mathbf{w}(n) - \mathbf{w}^T(n)\mathbf{V}'(n)\mathbf{V}'^T(n)\mathbf{w}(n)\mathbf{w}(n)) \quad (3.27)$$

Assuming that (3.27) converges to a steady solution $\mathbf{w}(n) \rightarrow \psi$ as $n \rightarrow \infty$, and also that the learning rate η is very small and that the correlation $\mathbf{R} = E\{\mathbf{V}'\mathbf{V}'^T\}$ has distinct eigenvalues, the expectation of expression (3.28) becomes, as n approaches infinity,

$$\mathbf{0} = \mathbf{R}\psi - (\psi^T\mathbf{R}\psi)\psi \quad (3.29)$$

or that the equilibrium condition $w \rightarrow \psi$ satisfies the eigenproblem

$$\mathbf{R}\psi = \lambda\psi \quad (3.30)$$

which is the same eigenproblem as in the POD mode calculation [42]. The only stable solution, ψ , is the eigenvector with largest eigenvalue, so the single neuron converges to the mode with largest energy.

A single layer of N neurons can be used, in the same way, to extract the N largest POD modes [42][47]. Each neuron, labelled i , in the layer is presented with an input vector from which the contribution to the flow field along the $(i-1)$ largest POD modes has been subtracted. Each neuron, i , thus converges to the i 'th largest POD mode. The first neuron converges to the largest POD mode, as in the single neuron case; the second neuron is presented with the same input vector minus the contribution of the first POD mode, and so converges to the second mode; and so on. The layer of linear neurons is shown in figure 3.7. The number of inputs, P , corresponds to the number of measured points times the number of values recorded at each point (for example two Cartesian velocities). The number of outputs, N , corresponds to the number of modes that are calculated and is less than P . The output of any particular neuron in the network is

$$a_j(n) = \sum_{i=1}^P w_{ji}(n)v_i(n) \quad (3.31)$$

The synaptic weights are labelled so that w_{ji} corresponds to the j 'th neuron connected to the i 'th input. The network is trained with the algorithm [42]

$$w_{ji}(n+1) = w_{ji}(n) + \eta \left(a_j(n)v_i(n) - a_j(n) \sum_{k=1}^j w_{ki}(n)a_k(n) \right) \quad (3.32)$$

The training algorithm can be expressed in a similar form to (3.27)

$$w_{ji}(n+1) = w_{ji}(n) + \eta a_j(n)(v_i'(n) - w_{ji}(n)a_j(n)) \quad (3.33)$$

where the modified input to each neuron is dependent on the position of the neuron in the layer;

$$v_i'(n) = v_i(n) - \sum_{k=1}^{j-1} w_{ki}(n)a_k(n) \quad (3.34)$$

The input to a neuron j is thus the flow field vector minus the contribution to the flow field along the directions of the $(j - 1)$ largest POD modes. Hence, as $n \rightarrow \infty$,

$$\mathbf{W}_j = (w_{j1}, w_{j2}, \dots, w_{jP})^T \rightarrow \psi_j \quad (3.35)$$

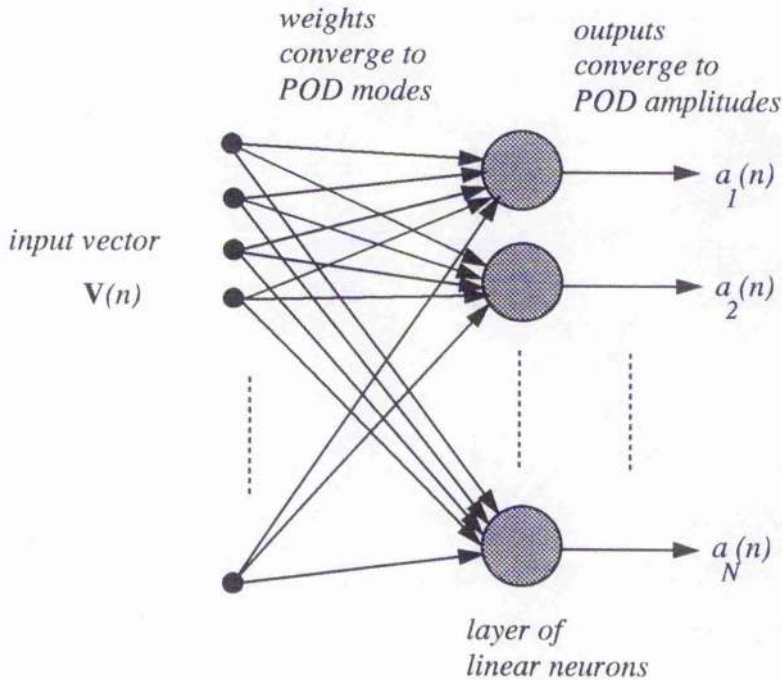


Figure 3.7: Mode Extraction Network

The convergence analysis of the self organizing algorithm for feature extraction is quite involved (a detailed exposition is presented in [42]). For convergence, the algorithm requires that the learning rate is very small and that *the input elements are drawn from a stationary stochastic process with zero mean*. The latter requirement seems in conflict with inputs measured from a flow subject to time-dependent forcing. However, if the process for selection of snapshots outlined in chapter two is followed then the network is presented with an ensemble that has a distinct, stationary, correlation having eigenvectors, which constitute sub-optimal modes, that can be used to reconstruct ensemble members [31]. Care must be taken to ensure that no

particular forcing regime, or phase of the flow, is favoured [36]. The input vectors to the network are drawn from N different time series of velocity fields, each of which exhibits a set of characteristic features caused by a control input. The mean flow for each of the N time series is similar to every other because of the restriction placed on the type of control (ie. the control does not modify the mean flow significantly). Each time series consists of M distinct snapshots of the velocity field taken at regular times within one period of a forcing cycle. The input vectors to the network are,

$$\mathbf{V}'_k = \mathbf{V}_k - \bar{\mathbf{V}} \quad (3.36)$$

with $k = j + (i - 1)M$, where the time series index, $i = 1, \dots, N$ and the time point (within each time series) index, $j = 1, \dots, M$. The input vectors thus have zero mean. Assuming that the network learning rate is very small, the network weights (upon application of algorithm (3.33)) converge [42] to,

$$\mathbf{R} = E\{\mathbf{V}'(t)\mathbf{V}'^T(t)\} \quad (3.37)$$

There are only $K = MN$ distinct input vectors (which are presented cyclically) to the network, so,

$$\mathbf{R} = \frac{1}{K}[\mathbf{V}'_1\mathbf{V}'_1{}^T + \mathbf{V}'_2\mathbf{V}'_2{}^T + \dots + \mathbf{V}'_K\mathbf{V}'_K{}^T] \quad (3.38)$$

which is identical to the concatenated approach [31] [44] detailed in Chapter Two. The network weights thus converge to the same set of sub-optimal modes as presented in Chapter Two. The network weights, or POD modes, satisfy the flow boundary conditions; incorporate the effect of a control (which may include boundary or interior control); and satisfy the incompressibility condition.

Once the self-organizing network has converged with the training ensemble, the learning rate can be set to zero. The network then acts as a linear filter that extracts the mode amplitudes from an examination of the flow field; performing the calculation,

$$a_k(t) = A_k(t) = (\boldsymbol{\psi} \cdot \mathbf{V}'(t)) \quad (3.39)$$

The mode amplitude filter, which has the structures of the POD modes contained in its weights, is implemented in the control scheme as shown in figure 3.8. The controller is fed a measurement of the flow field, from which it calculates the mode amplitudes, a control output and a predicted response. The control output is applied to the actual flow.

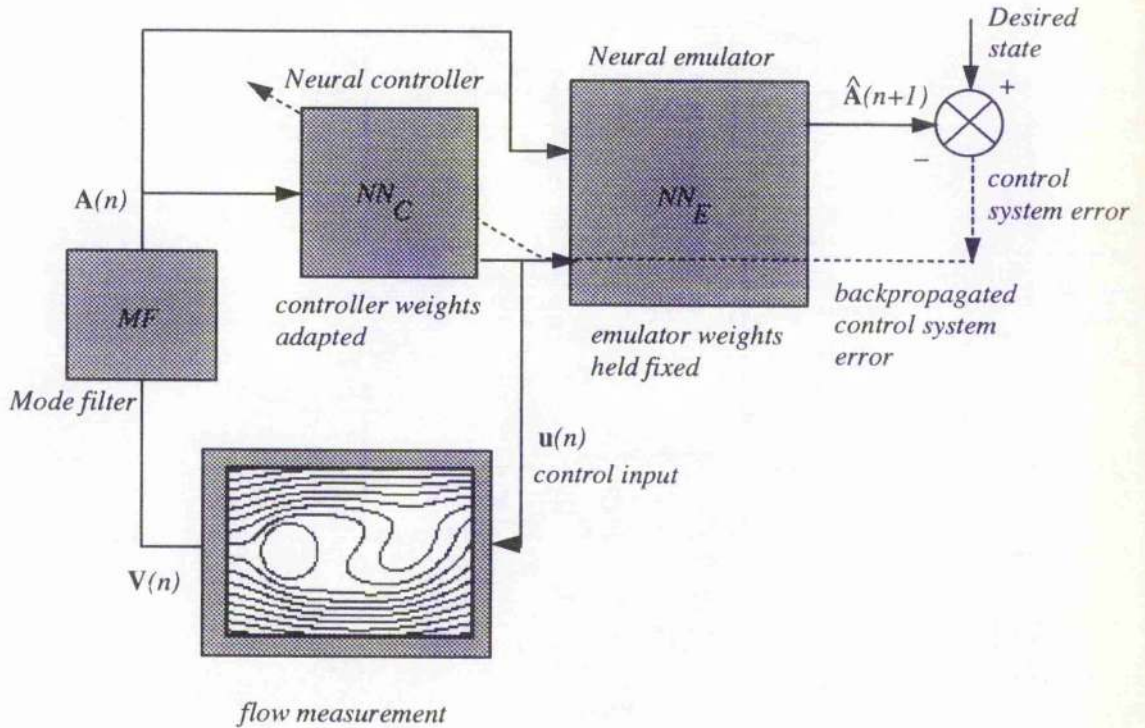


Figure 3.8: Non-linear Control of Fluid Flow

3.6 Summary

The empirical estimation of the wake flow POD mode dynamics has several advantages over other methods for the construction of a wake controller. Empirical estimation of the dynamics of the largest POD modes, and hence of the large scale spatial structures of the wake, automatically accounts for the influence of an external control and the small spatial scales; that is, a curved, non-linear inertial manifold, with a time dependent control is approximated. The empirical process is potentially

more accurate than a classical Galerkin approximation, where the rational addition of control inputs is difficult and where the small spatial scales are neglected—the Galerkin process represents approximation of an autonomous, flat, linear inertial manifold. The measurements of the flow field, which are input to the mode amplitude filter, do not necessarily have to be of velocity—other flow features, which are related to the velocity field, may be chosen if they are easier to measure. The empirical prediction of the flow dynamics allows the modes to take any form that signal the presence of wake oscillations—if however, the flow dynamics were predicted by a Galerkin projection then the modes would have to be constructed from the velocity field.

Neural network estimation of the POD modes and their amplitude response has an advantage over other empirical estimations because the neural network emulator is readily integrated into a robust non-linear control strategy.

Chapter 4

A Prototype Wake Control Problem

4.1 Introduction

To illustrate the utility of the low-dimensional characterization method, the unsteady velocity field of a low Reynolds number, two-dimensional cylinder wake is simulated. The cylinder flow is a useful prototype flow because of its relative geometric simplicity and the spatial and temporal complexity of the downstream vortex street that forms as a result of a near wake absolute instability [2][39]. The cylinder wake has many of the stability characteristics and corresponding flow features of much more complex flows. The cylinder flow is simulated numerically, so that the entire velocity field is available for analysis. The velocity fields at various points in time in a *wake transient* (during the unforced growth of oscillations) are used to form the characterization ensemble. To characterize non-stationary flow features that are the result of a control input and also to train a non-linear emulator of the mode dynamics it is necessary that the cylinder flow is forced by a time-varying control input. To obviate the large computational costs involved in forcing the high resolution numerical solution of the wake and avoid specification of a particular control

mechanism, the response of the flow is simulated by a prototype model. (*A priori*, it is not known what specific type of active control device will affect the flow enough to stabilize the modes). Simulation of the control strategy with a full numerical solution of the forced Navier-Stokes equations is preferable for accuracy but is computationally intensive. It is appropriate that *initial* testing of the control strategy is employed on a simpler prototype flow so that identification of important parameters in the controller proceeds quickly (most of the computational effort required for a full numerical solution concentrates on modelling the flow itself and identification of important parameters in the controller is not straightforward). The prototype flow is a low-dimensional form of the flow equations with an artificial control input. The low-dimensional prototype flow is based on a set of POD modes developed from the unforced numerical (CFD) simulation. The validity of the prototype model is discussed in subsection 4.3.2 (both with respect to unforced flows, where a quantitative comparison with the full numerical solution can be made, and with respect to forced flows, where only a qualitative comparison between the model and experiment can be made). The prototype captures the important stability features of the unforced flow and accurately represents the spatial and temporal characteristics of the unforced flow. The prototype also mimics some of the features of the forced cylinder wake, and it can be asserted that the prototype flow is a reasonable qualitative model of the forced and unforced cylinder wake. The prototype flow model can be integrated easily and is used to provide artificial, non-stationary velocity fields for characterization and subsequent control.

4.2 Numerical Solution of the Laminar Cylinder Wake

Wake

The governing equations for the two dimensional, laminar, viscous, incompressible cylinder wake are the Navier-Stokes equations

$$\frac{\partial \mathbf{u}}{\partial t} = -(\mathbf{u} \cdot \nabla) \mathbf{u} - \nabla \Pi + \nu \nabla^2 \mathbf{u} \quad (4.1a)$$

$$\nabla \cdot \mathbf{u} = 0 \quad (4.1b)$$

in Ω , subject to prescribed boundary conditions on $\partial\Omega$ and appropriate initial conditions.

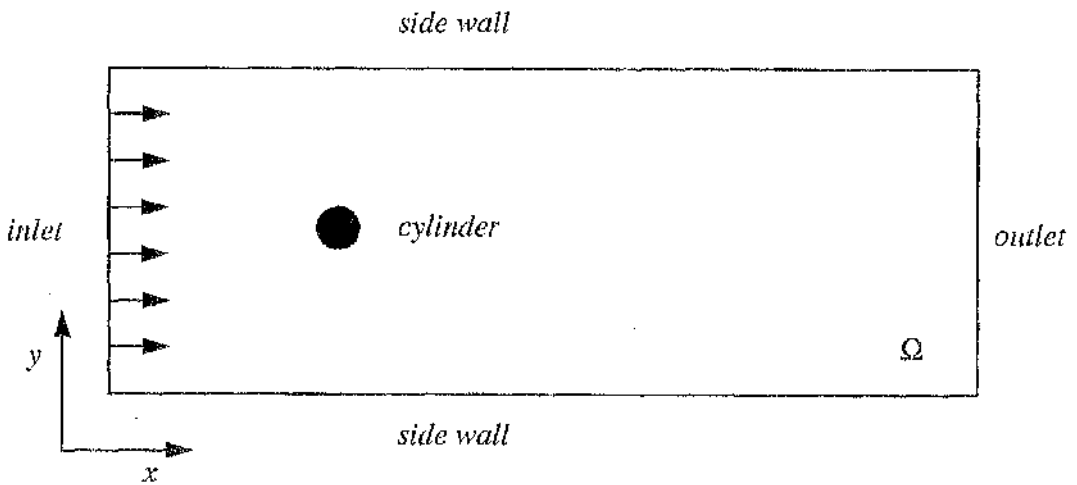


Figure 4.1: Problem domain

The governing equations are solved for a fluid occupying a region Ω , which is shown in figure 4.1, with boundary conditions as in table 4.1.

| | |
|-------|---|
| (i) | Uniform inlet velocity, $Re = 100$ |
| (ii) | No-slip condition at cylinder wall |
| (iii) | Potential flow at large y from cylinder |
| (iv) | Neumann outlet conditions |

Table 4.1: domain boundary conditions

Uniform inlet velocity at a Reynolds number of 100 ensures that the wake is within the laminar vortex shedding region ($47 < Re < 250$). The turbulent wake $Re > 250$ is more difficult to simulate. Walls are used at the sides of the computational domain rather than zero-velocity inlets to facilitate the introduction of external forcing of the wake (for example, acoustic sources placed astride the wake in a wind tunnel). To minimize the effects of the side walls on the flow, the side walls are placed far from the cylinder (5 cylinder diameters from the centre line). In addition, the side wall boundary conditions are set at zero vertical velocity with a horizontal velocity component equal to the inlet velocity. The resulting side boundary condition is not too dissimilar from a potential flow approximation in the far wake as the potential flow streamlines 5 cylinder diameters from the wake are almost straight. The last boundary condition in table 4.1 is added for numerical stability. Neumann outlet conditions impose zero normal gradients for all flow variables at the flow outlets. This type of boundary condition is responsible for significant artificial dissipation of the wake—vortex structures cease to exist prematurely, because of the outlet condition. The flow outlet is therefore placed at a large x , downstream of the cylinder.

The cylinder flow is simulated numerically, using the commercially available, control-volume, CFD package, FLUENT v4.10, running on an IBM RISC System 6000 320H workstation. The equations are reduced to their finite difference analogues by integration over each of the computational cells into which the domain is divided. A quadratic upwind scheme is used for interpolation between the grid points and to calculate the derivatives of the flow variables. This scheme minimizes the effects of numerical dissipation. The u and v momentum equations are each solved in turn using current values for pressure. The velocities obtained may not satisfy the local mass continuity equation, so a 'Poisson' type equation is derived from the continuity and linearized momentum equations. The pressure correction equation is then solved to obtain the necessary corrections to the pressure and velocity fields

such that continuity is achieved[49].

The finite difference grid is 35 cylinder diameters long by 10 cylinder diameters wide. These values are chosen so that the flow is not significantly affected by the Neumann boundary condition of (iv) in table 4.1, which causes artificial dissipation of the wake (even although a quadratic upwind scheme is used), and also so that the flow is not significantly affected by the wall restriction of (iii) in table 4.1. A body fitted grid is used, and grid points are clustered around the surface of the cylinder so that the boundary layer, which has a thickness proportional to $1/\sqrt{Re}$, is modelled accurately[49]. The absolutely unstable region (the near wake of the cylinder) also has a cluster of grid points. Three different meshes, with the same structure but different numbers of grid points, are used to determine the dependency of the flow solution on the grid. A coarse mesh comprising 3000 cells, an intermediate mesh comprising 5000 cells and a fine mesh comprising 6600 cells are studied. Two views of the fine mesh are shown in figures 4.2 and 4.3. An initial domain-wide boundary condition of potential flow is supplied at the beginning of calculations (the mean flow is the ideal initial condition for the examination of the growth of instability— however, the mean flow during shedding is not known prior to simulation). Viscosity is then added to the computational algorithm. An extremely small time-step is used, initially, for numerical stability in the initial transient phase of the solution. The initial time-step, after the introduction of viscosity and the no-slip condition on the cylinder surface, is 1×10^{-6} of the expected period of oscillation. After the separation bubble begins to form the time-step is increased in stages but care is taken to maintain convergence. Once vortex shedding begins, the time-step is further increased to a final value of 600 time-steps per oscillation of the flow. This final time-step value compares well with values used by other authors [2] [39]. The Strouhal number obtained using the coarse mesh is 0.132 which is much lower than that expected from experiment. The intermediate mesh yields a Strouhal number of 0.150 and the fine mesh yields a Strouhal number of 0.153. The

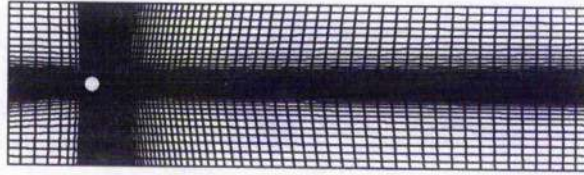


Figure 4.2: Computational grid

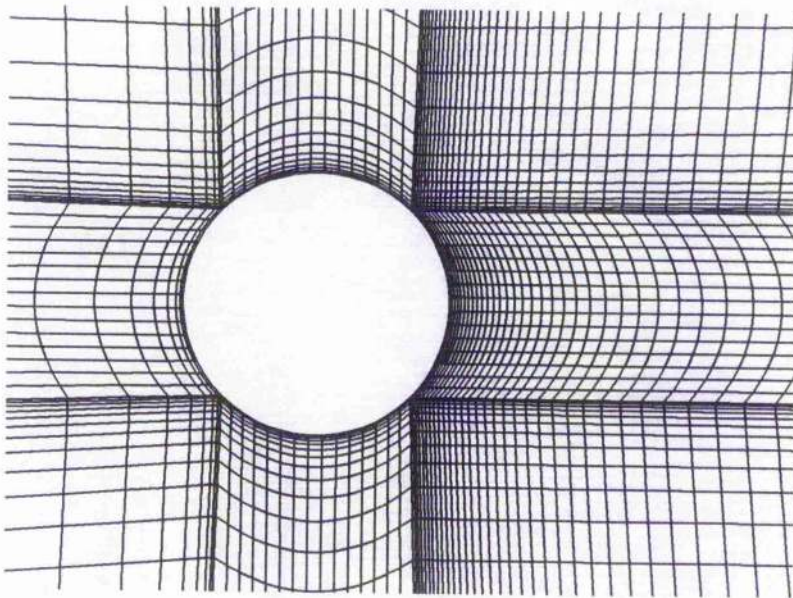


Figure 4.3: Close-up of computational grid around cylinder

Strouhal number of the fine mesh is within the range expected from experiment and further mesh refinement is considered unnecessary (there is only a small difference between the intermediate mesh solution and the fine mesh solution and any further refinement increases computing cost). Subsequently, the fine mesh, comprising 6600 cells is chosen for all further calculations. The transient velocity, observed during the growth of oscillations, at a point in the wake is shown in figure 4.4. After steady periodic oscillations begin, the flow is simulated for approximately fifteen flow cycles, in order to obtain estimates of the power spectral densities. Time histories of the non-dimensional velocity (u/U_{inlet} versus non-dimensional time t/T_{shed}) at a point in the wake during shedding are shown in figures 4.5 and 4.6.

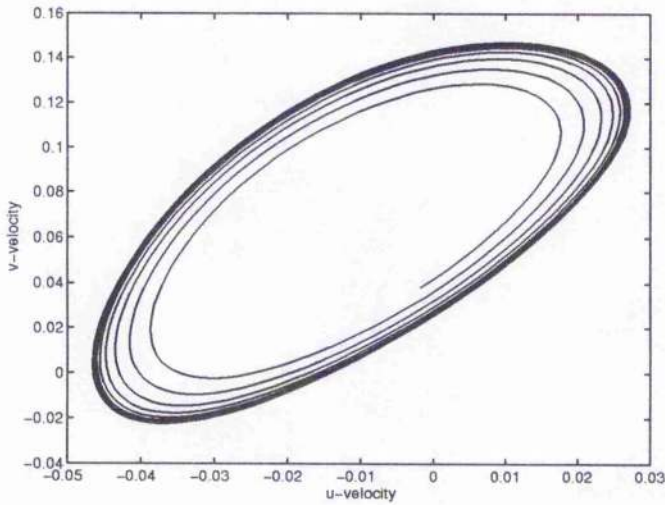


Figure 4.4: Transient velocity during growth of oscillations

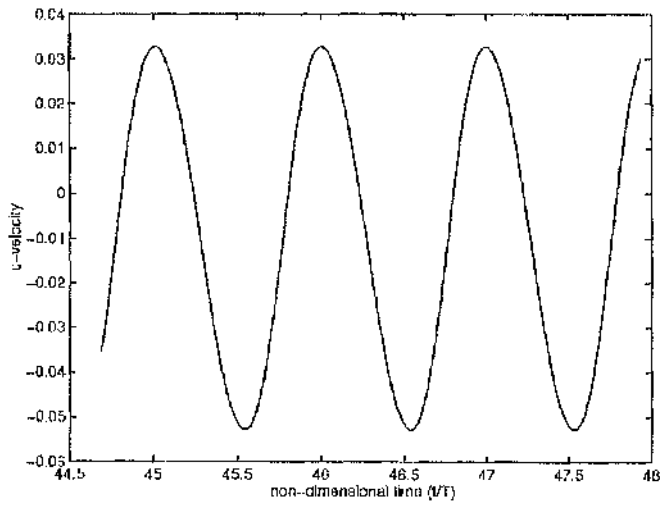


Figure 4.5: Horizontal velocity vectors during shedding

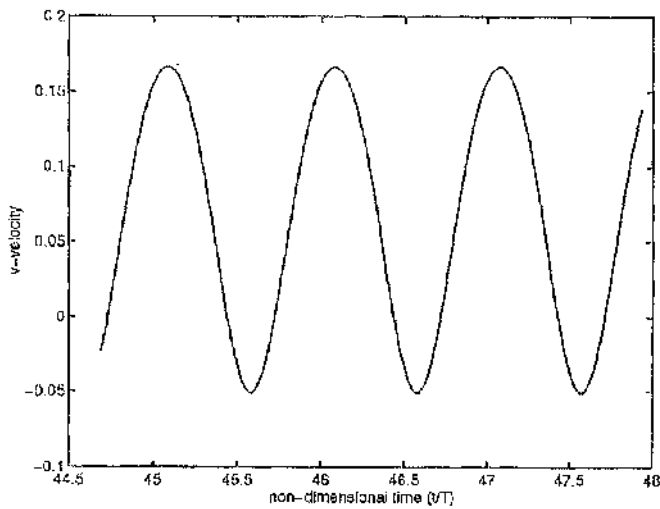


Figure 4.6: Vertical velocity vectors during shedding

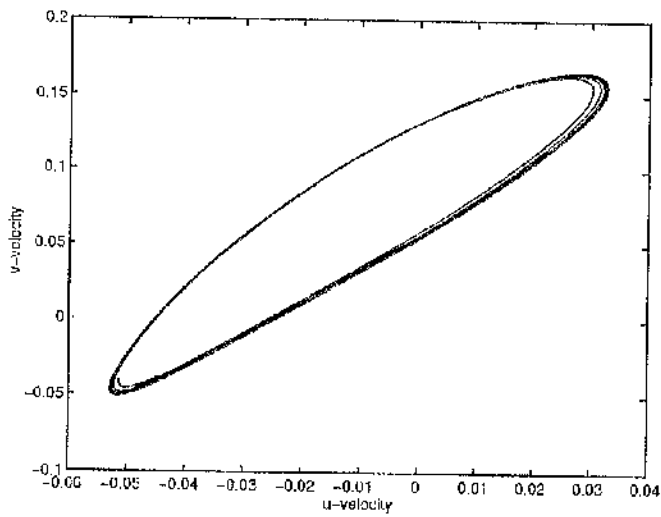


Figure 4.7: Velocity limit cycle during shedding

The power spectral density, calculated from a 512 point Hanning window of these velocity signals is shown in figure 4.8. The signal is seen to contain one dominant frequency (the vortex shedding mode) and perhaps two or three higher significant harmonics. The frequency content of the wake allows calculation of the flow Strouhal number, which is used as a measure of the accuracy of the numerical simulation[2].

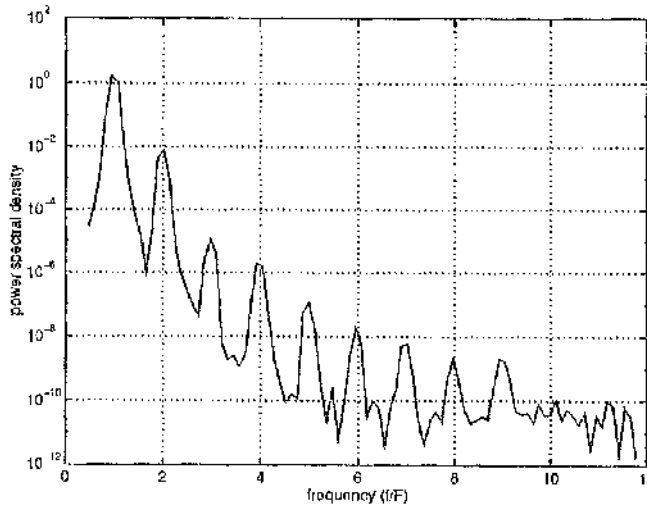


Figure 4.8: Power spectral density of velocity signal

| Reference | Strouhal number |
|-------------|-----------------|
| ref [50] | 0.147 |
| FLUENT | 0.153 |
| ref [51] | 0.155 |
| ref [52] | 0.161 |
| ref [53][2] | 0.163-0.167 |
| ref [2] | 0.179 |

Table 4.2: Comparison of Strouhal numbers for FLUENT, other routines and experiment

Experimentally, the Strouhal number is a function of the Reynolds number [2][54], and, for a Reynolds number of 100, a Strouhal number of 0.167 is expected from empirical evidence[54]. Numerical solution of the cylinder wake using spectral element methods results in a slightly higher value of 0.179 [2](spectral element calculations involve very little numerical dissipation and are thus judged quite accurate [2]). The discrepancy between experimentally observed Strouhal numbers and those calculated numerically may be due to the fact that Strouhal numbers generally decrease as the cylinder aspect ratio (length/diameter) decreases [55]. Experimental measurements of *three-dimensional* flows are therefore likely to differ from Strouhal numbers calculated numerically, in *two-dimensions*. The Strouhal number calculated by the FLUENT method compares well with those calculated by other authors, as is apparent in table 4.2. The lower than average calculated value of St is possibly because of artificial dissipation in the FLUENT solution algorithm. The streamlines and velocity vectors obtained in the solution are also qualitatively similar to those obtained by other authors [52][51]. Typical realizations of the velocity vectors and streamlines are shown in figures 4.9 and 4.10. The artificial dissipation of the vortex street caused by the outlet Neumann boundary condition is highlighted in figure 4.11. The Neumann outlet condition is, however, the only outlet condition available in FLUENT v4.10.

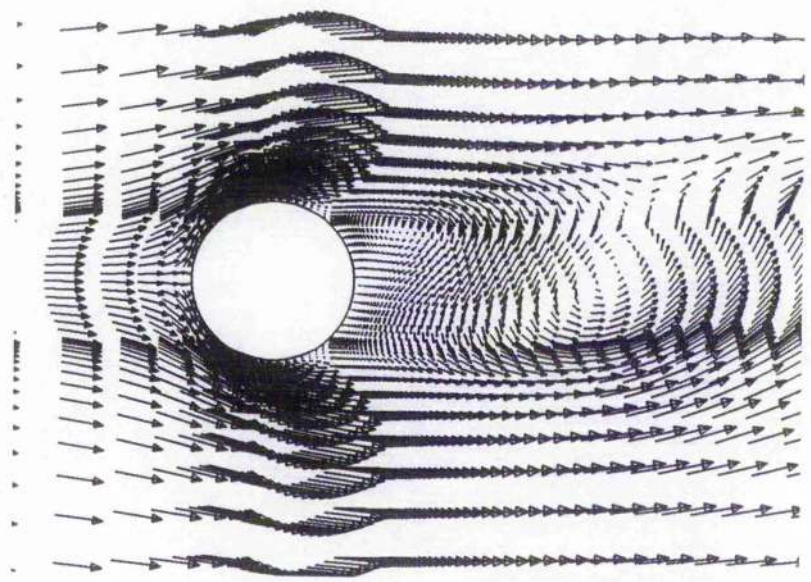


Figure 4.9: Typical flow velocity vectors

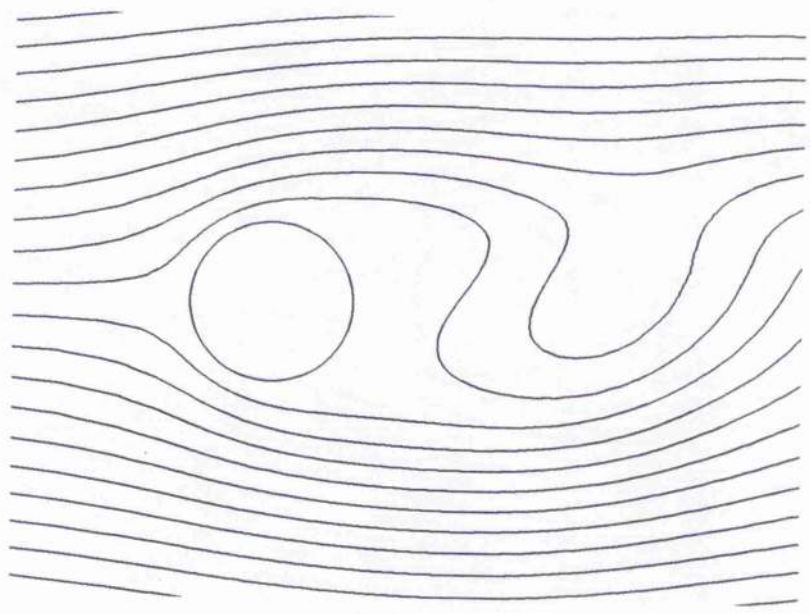


Figure 4.10: Typical flow streamlines

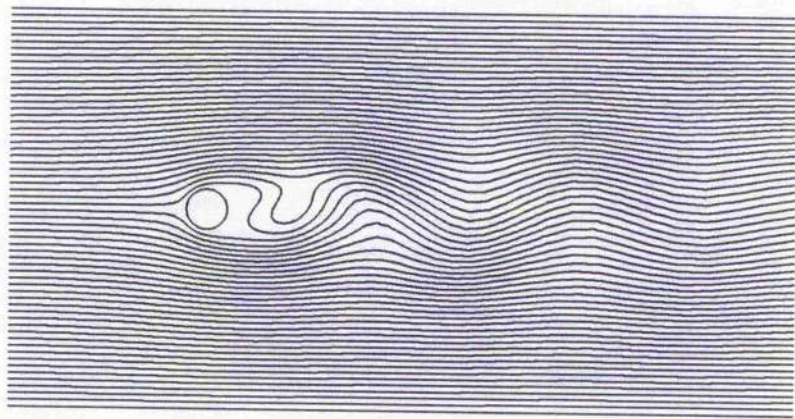


Figure 4.11: Artificial dissipation of wake: streamlines

4.3 Simulation of a Forced Cylinder Flow

The numerical (CFD) solution of the cylinder wake forms an ensemble of discrete velocity fields, that can be characterized by a finite set of POD modes. Ideally, the cylinder wake should be forced by an external control input, at various frequencies and amplitudes, so that the data ensemble is representative of any destabilized global modes and flow features that are likely to occur during a control run. Experimentation is also required to ascertain what type of control (for example: cylinder rotation, vibration, alternate suction and blowing at the separation points, acoustic excitation or vibrating wire excitation etc.), and what position of control device, would meet with success. To circumvent the high computational cost of large amplitude, periodic or aperiodic forcing of the discretized solution, a simpler prototype flow model, which has the purpose of testing the feasibility of the control scheme, is introduced. The essential properties of the prototype model are that it retains the important absolute instability features of the cylinder flow, produces qualitatively correct flow responses to forcing, and produces qualitatively correct spatial velocity fields, while remaining simple and easy to integrate.

4.3.1 Generation of a Prototype Cylinder Flow

A non-linear flow model that approximates the spatial wake features and retains some of the wake stability characteristics is presented in the appendix, but is outlined here. *A first approximation to modelling the forced flow is obtained by using a model of the unforced flow.*

A small transient of the wake is available from the unforced CFD solution. Velocity field data collected during the growth of wake oscillations, from the steady state, encapsulates a neighbourhood of the unforced limit cycle. An example of a section of the transient is shown, for one point in the velocity field in figure 4.4.

Twenty velocity fields from two flow cycles approaching the attractor are collected. This number of snapshots is appropriate for such a temporally simple, laminar, unforced wake—for example: 20 snapshots are used in reference [39] for the $Re = 100, 150$ and 200 cylinder wake and are shown to provide adequate representation of the unsteady velocity field.

The ensemble average of all of the velocity fields, which approximates the time average velocity field is calculated and subtracted from each velocity field to form twenty flow ‘snapshots’. The collection of snapshots is used to generate a reduced correlation matrix, with relation (2.22). The eigenvectors of the symmetric, non-negative reduced (20×20) correlation matrix are readily calculated via Householder reduction and the QL algorithm. The first eight eigenvalues are shown in table 4.3. A bar chart representing the eigenvalues is shown in figure 4.12: almost all of the flow

| | |
|---|---------------|
| 1 | 5.1525888e-01 |
| 2 | 4.6617187e-01 |
| 3 | 8.1370641e-03 |
| 4 | 7.7949658e-03 |
| 5 | 1.2503575e-03 |
| 6 | 1.2433327e-03 |
| 7 | 6.5438928e-05 |
| 8 | 6.5262895e-05 |

Table 4.3: First eight eigenvalues of the unforced velocity field correlation

energy is contained in the high energy modes. Pictures of the first four eigenvectors of the reduced correlation matrix, which are the only eigenvectors with significant eigenvalues, are shown in figure 4.13. The figure shows that the first four eigenvectors are not contaminated by noise. These eigenvectors are used in conjunction with the unforced flow snapshots to generate the POD modes. Only, the first four POD modes capture significant flow energy and so the higher modes are neglected. A higher Reynolds number flow, a turbulent flow, or a time-forced flow would exhibit much richer mode composition. The spatial structure of the first four POD modes,

developed from the CFD data are shown in figure 4.14. The modes are normalized, so as to be orthonormal. Modes developed from double the number of snapshots (40) are similar in appearance. The first eight eigenvalues for the 20 snapshot case and the 40 snapshot case are almost identical. The smaller eigenvalues show slight differences between the 20 and 40 snapshot cases.

A Galerkin approximation of the Navier-Stokes equations provides a succinct description of the *unforced* flow dynamics, but is difficult to establish because the Galerkin method involves spatial differentiation of the modes and mean flow and calculation of their vorticities. Numerical differentiation of the modes is difficult, and introduces error, because the modes are formed from a spatially discrete, irregular grid. The structure of the Galerkin model is, however, known—the Galerkin model is a quadratic ordinary differential equation for each mode amplitude. A transient set of velocity fields (obtained from the CFD solution during the growth of oscillations), from which the POD mode amplitudes and time derivatives at each time point are measured, can be used to fit the unknown coefficients of the quadratic equations by least squares (as outlined in Appendix A). Fitting of the coefficients by least squares requires that a large enough section of transient data is available (transient measurements of the unforced flow are obtained during the growth of vortex shedding oscillations from a steady state initial condition). The complete resolution of the coefficients becomes progressively more difficult as the mode index increases (while the mode energy decreases).

The cylinder flow, represented by the CFD data is adequately approximated by just four modes. The higher modes and their time derivatives are corrupted by noise. Least squares solution of the Galerkin approximation is performed using four retained modes, resulting in four quadratic differential equations for the mode amplitudes with twenty eight coefficients each. Models constructed from a larger number of modes are not resolved accurately by the least squares identification method and available transient data.

It is known that a single cubic equation is able to capture the instability of the mean flow and the stable limit cycle oscillations and so cubic terms are added to the prototype mode equations of the empirical Galerkin quadratic model and the coefficients again fitted to the transient by a least squares, empirical approach. Cubic terms may appear in a *non-linear* Galerkin model and are introduced here to avoid adding extra modes to the four mode prototype model.

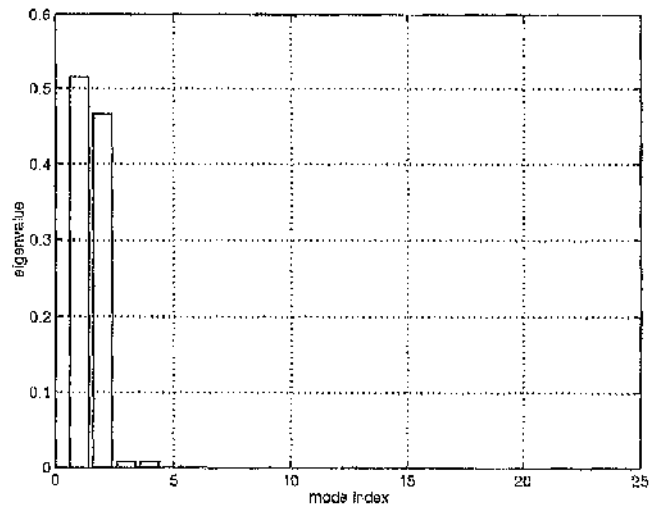


Figure 4.12: Eigenvalues of the POD modes

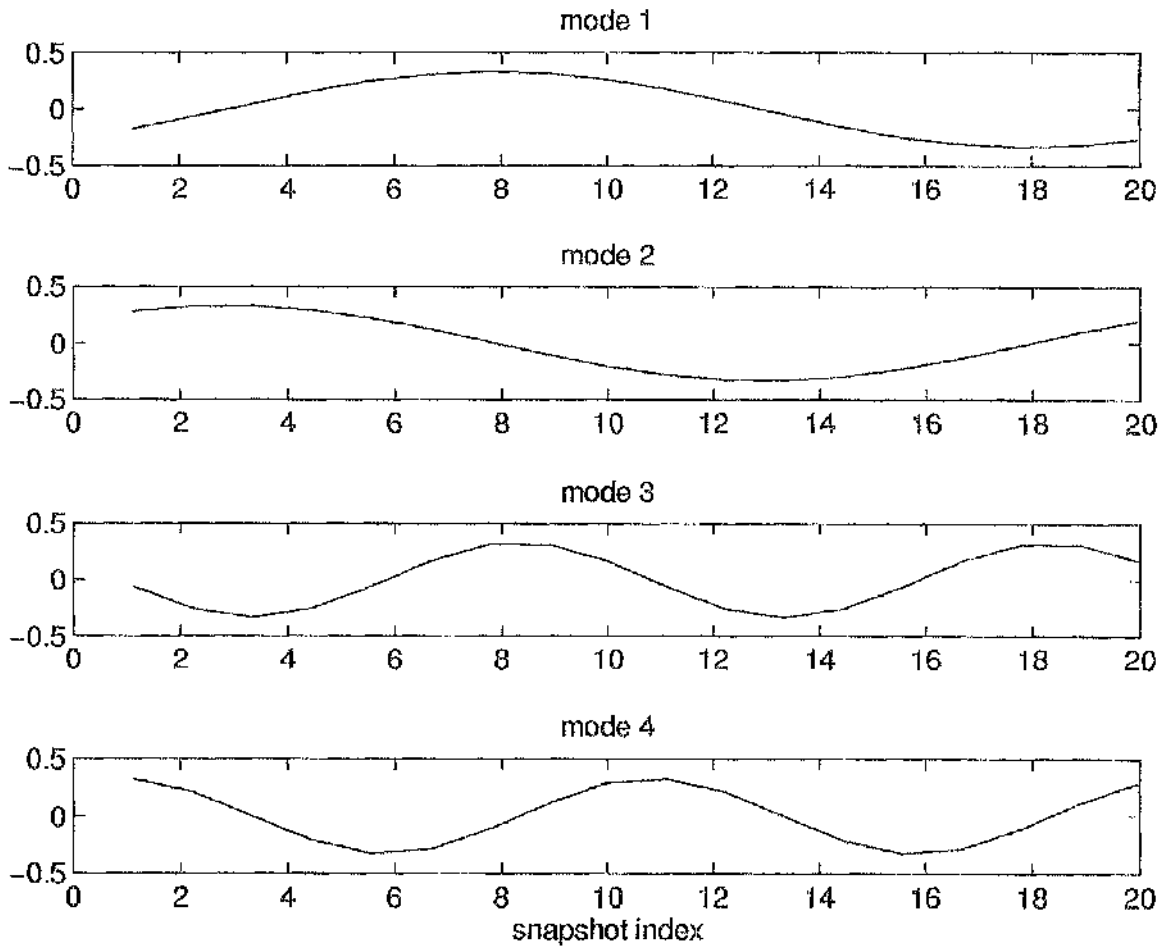


Figure 4.13: Eigenvectors of the reduced correlation matrix, used to construct first four POD modes

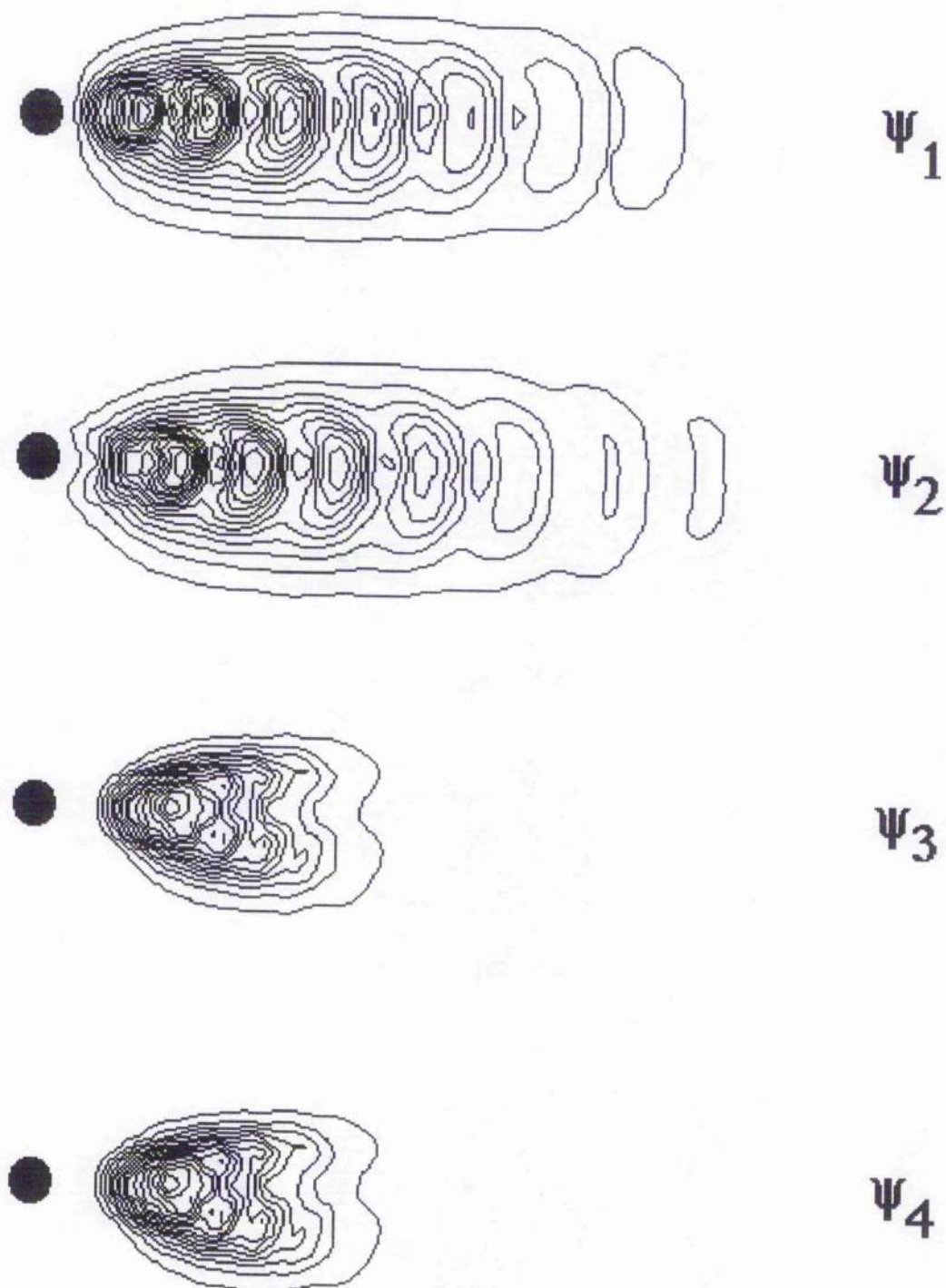


Figure 4.14: Spatial structure of the first four POD modes of the cylinder wake: shown are contours of velocity magnitude

The form of the prototype model with added cubic terms is, for each mode $k = 1, \dots, 4$,

$$\frac{dA_k}{dt} = c_o^k + \sum_{i=1}^4 c_{1,i}^k A_i + \sum_{i=1}^4 \sum_{j=1, j \geq i}^4 c_{2,i,j}^k A_i A_j + \sum_{i=1}^4 \sum_{j=1, j \geq i}^4 \sum_{l=1, l \geq j}^4 c_{3,i,j,l}^k A_i A_j A_l \quad (4.2)$$

When cubic terms are calculated for the two largest mode amplitudes (A_1 and A_2), the prototype model captures the growth of instability accurately, and captures the behaviour of unforced vortex shedding behind the cylinder as described by the CFD data. Cubic coefficients for the smaller two modes are not calculated. The validity of the unforced prototype flow model (with respect to the original CFD data) is discussed in section 4.3.2.

The rational addition of control terms into the Galerkin approximation is difficult; however, the addition of *ad hoc* terms to dynamical models of the cylinder dynamics is known to produce qualitative agreement with experiment [11]. For example, the addition of an interior sinusoidal forcing term to a low order, cubic model of the $Re = 114$ flow past a circular cylinder produces qualitatively correct time histories and qualitatively correct regions of entrainment [11]. Simple addition of forcing terms to the least squares developed model should also produce qualitatively correct results, and mimic the response of the flow to excitation. Obviously, a control input will affect each of the prototype mode equations by a different amount as the interaction of the control with each prototype mode depends on the spatial structure of each mode. In the Galerkin approximation outlined in Appendix A, addition of a source term to the Navier-Stokes equations results in an extra forcing term for each mode equation, $(\psi_k \cdot f_a \mathbf{f}_x)$, where f_a is the control amplitude and \mathbf{f}_x is the spatial distribution of the control in the flow field. An amplitude and spatial distribution of a localised interior control input at a coordinate (a, b) in the wake is obtained from [2]

$$F(x, y, t) = f_a(t) \exp\left(-D((x-a)^2 + (y-b)^2)\right) \quad (4.3)$$

where D is the rate at which the contribution of the force decays with distance from

the source. This position of the localised control input and the value for the decay rate is chosen such that the forcing is small at the domain boundaries and significant only in the near wake (which is necessary for control of the global modes) [2][7]. The spatial distribution of the control is shown, relative to the cylinder, in figure 4.15. This form of control simulates an interior forcing provided by an active control device such as a vibrating wire [2]. The fluid adjacent to the control device acquires an acceleration equal to the vibrating source—further from the source the acceleration decays. This distribution of control provides forcing of the near wake consistent with the boundary conditions as the amplitude of the control at the domain boundaries is very small. Vibrations of the cylinder (which are known to be suitable for control of global flow oscillations [6]) give rise to a similar forcing [2]. The complete form of the prototype flow model is, for $k = 1, \dots, 4$,

$$\frac{dA_k}{dt} = c_0^k + \sum_{i=1}^4 c_1^k A_i + \sum_{i=1}^4 \sum_{j=1, j \neq i}^4 c_{2,ij}^k A_i A_j + \sum_{i=1}^4 \sum_{j=1, j \neq i}^4 \sum_{l=1, l \neq i, j}^4 c_{3,ijl}^k A_i A_j A_l + c_4^k f_a \quad (4.4a)$$

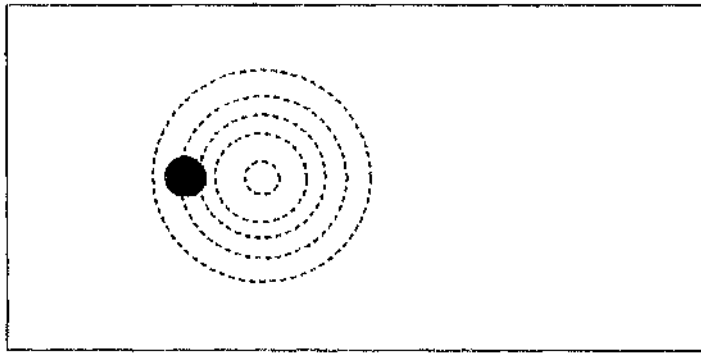
$$\mathbf{V}(t) = \bar{\mathbf{V}} + \sum_{i=1}^4 A_i(t) \boldsymbol{\psi}_i \quad (4.4b)$$

where the $A_k(t)$ are time varying amplitudes of the first four POD modes, $\boldsymbol{\psi}_k$, of the entire cylinder wake, established from the CFD velocity field ensemble.

The control input, although introduced somewhat artificially to the unforced prototype model, is useful because it produces temporal flow responses that are in qualitative agreement with experimental observations of forced cylinder wakes. This qualitative agreement is discussed in the next subsection. Similar models for forced wake flows are cited in the literature [11]. Explicit representation of the model, and its development, is presented in the appendix.

4.3.2 Validity of the Prototype Flow Model

The validity of the prototype flow model is important: the model must approximate the unforced cylinder wake (this can be verified quantitatively, with comparison to



The control input is on the wake centre-line, two cylinder diameters downstream of the cylinder position. The force decay rate is 20 and so the magnitude of control at the domain side walls is less than 0.007 times the value in the near wake.

Figure 4.15: Contours of force contribution

the CFD solution) and also retain some of the qualitative features of the forced wake. In this subsection, the prototype model is compared to the unforced flow, and then compared to experimental, forced wakes.

The prototype flow model (4.4) consists of a spatial part (4.4b), which describes the spatial structure of the velocity field given a set of mode amplitudes, and a temporal part, which determines the dynamical behaviour of the amplitudes. The ability of (4.4b) to reconstruct the velocity field of the unforced cylinder wake is therefore important, and is established by comparison of the fraction of kinetic energy present in the actual and reconstructed velocity fields [32]. For any fluctuating velocity field, $\mathbf{V}'(t)$, a measure of instantaneous kinetic energy is given by,

$$E = \mathbf{V}' \cdot \mathbf{V}' \quad (4.5)$$

The normalized instantaneous energy difference between the actual velocity fields and those reconstructed by (4.4b) is,

$$e = \frac{|\mathbf{V}' \cdot \mathbf{V}' - \sum_{i=1}^4 (\mathbf{V}' \cdot \boldsymbol{\psi}_i) \boldsymbol{\psi}_i|}{(\mathbf{V}' \cdot \mathbf{V}')} \quad (4.6)$$

The average normalized kinetic energy error over one period of the four mode reconstruction is low ($\bar{\epsilon} = 0.03$). The spatial structure of the unforced cylinder wake is therefore described adequately by the prototype flow model (4.4b), as long as the correct modal amplitudes are specified by (4.4a). Only four POD modes are necessary for the reconstruction because the wake is low Reynolds number, and thus laminar, and because the unforced CFD wake is statistically stationary.

Given that (4.4b) adequately reconstructs the unforced velocity fields which constitute the unforced data ensemble, the validity of the temporal part of the unforced prototype flow, (4.4a), is of interest. Starting integration of the model with the mean flow, or zero mode amplitudes, as an initial condition for the velocity field should (with reference to experimental cylinder wakes) result in temporal growth of the von Kármán vortex shedding mode. The growth of oscillations is observed, in experiment, to be exponential in its linear stages; leading to limit cycle oscillations. The growth of oscillations is accurately modelled by a Landau equation and the oscillations predicted by the prototype flow are, indeed, comparable to those determined by a Landau equation and those observed in experiment [11]. The oscillations resulting from integration of (4.4a) are depicted in figure 4.16, which can be compared to figure 1.4. Velocity oscillations at two points in the wake, calculated using (4.4) and shown in figure 4.17, is also characteristic of the growth of experimental cylinder wake oscillations [11] and of the small transient observed in the CFD data, in figure 4.4. Only the qualitative nature of the instability is important for testing the feasibility of the control scheme, and the growth of instability, from the mean flow, is adequately represented by the flow prototype. The spatial structure of the velocity fields, observed during the growth of flow oscillations, is presented in figure 4.18. The velocity fields compare well to those of other numerical solutions [2][51].

A quantitative comparison between the temporal behaviour of the unforced prototype flow and the unforced numerical solution of the Navier-Stokes equations for

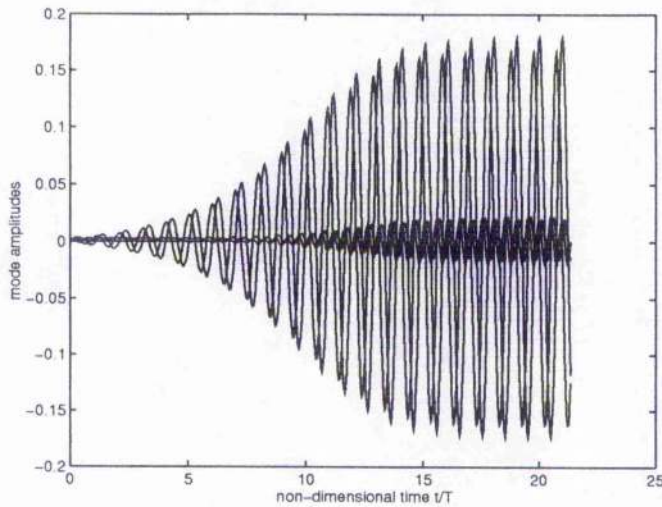


Figure 4.16: Temporal growth of unforced prototype modes

the cylinder wake is determined by examination of the limit cycle amplitudes predicted by the unforced prototype and those evident from the CFD data ensemble. The time histories of the measured mode amplitudes and those calculated by integration of the prototype are shown in figure 4.19. The solid lines are the mode amplitudes predicted by the unforced prototype, and the dotted lines are those measured directly from the CFD data ensemble. The frequency of oscillations is predicted reasonably well—the model predicts a Strouhal number just 2% greater than that observed from the CFD integration of the wake. The maximum mode amplitudes are also predicted accurately, for unforced limit cycle oscillations; projections of the limit cycle are shown in figures 4.20 and 4.21—the solid lines are the stable limit cycle predicted by the flow prototype and the dotted lines are observed from the CFD data. The figures show that the shape of the limit cycle is predicted adequately by the unforced prototype, and that the prototype oscillations are stable, as in the actual unforced cylinder wake—the error in maximum mode amplitudes of the prototype model is +0.68% for mode one, -1.68% for mode two, -6.20% for mode three and +4.24% for mode four. The higher error values for mode amplitudes three and four are not important, because of the relatively small magnitude of these

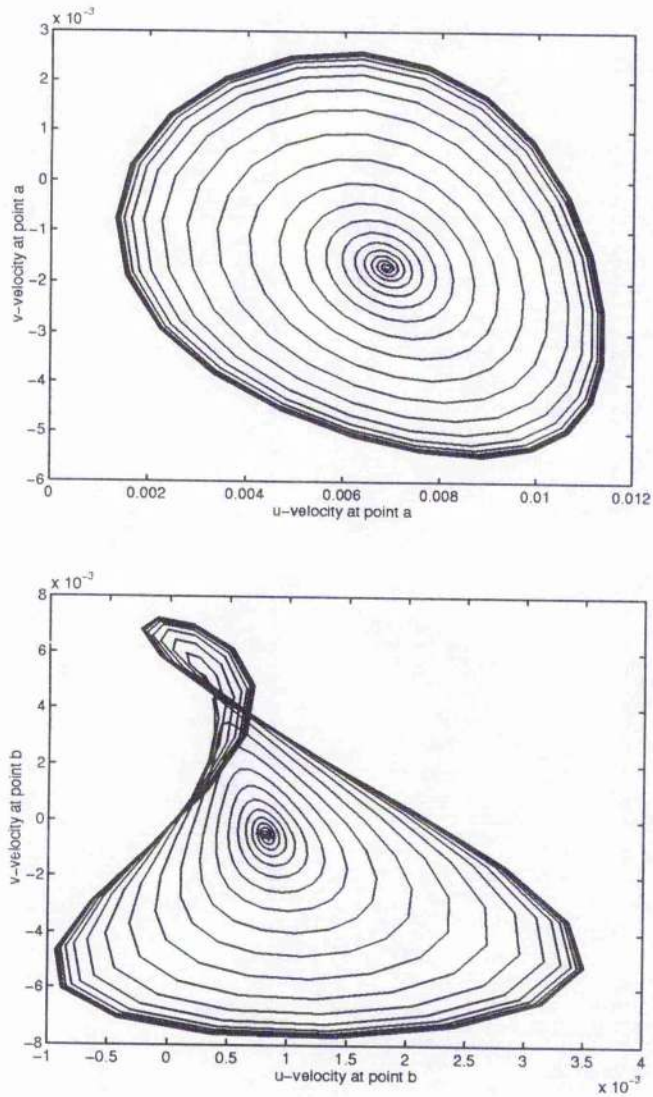


Figure 4.17: Temporal growth of unforced prototype velocities at point a and point b

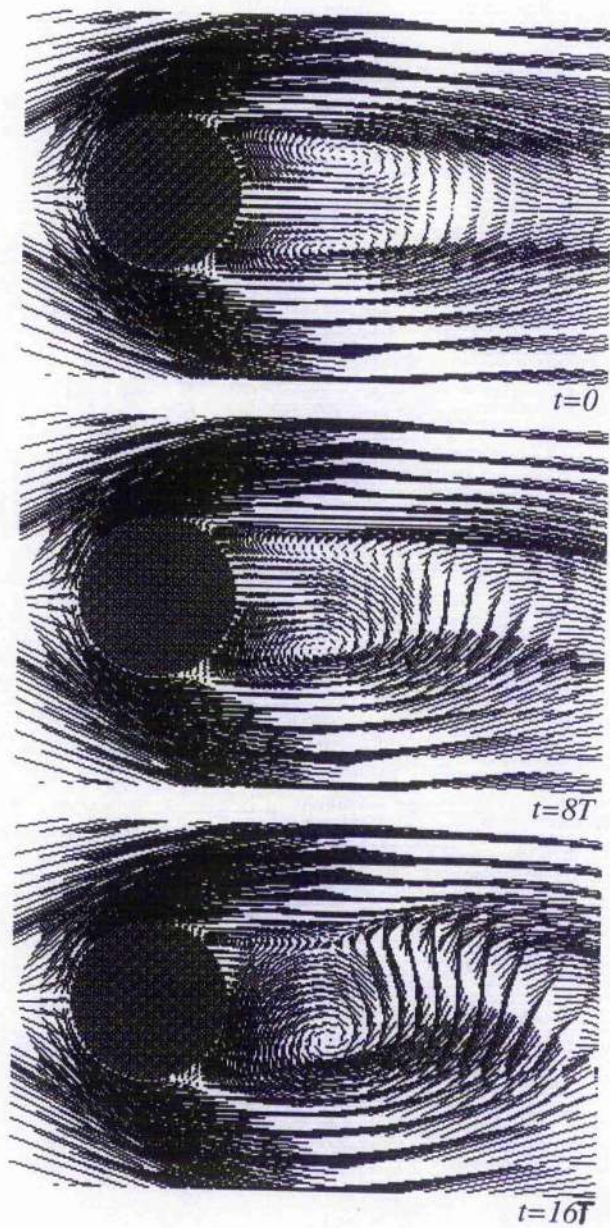


Figure 4.18: Simulated flow fields during growth of oscillations

modes. A reconstructed time series for a velocity signal at two different points in the unforced cylinder wake is shown in figures 4.22 and 4.23; the behaviour of the velocity at these two points, which were chosen arbitrarily, is predicted adequately. An idea of how the flow prototype predicts the velocity field of the cylinder wake is given by the velocity error averaged over one cycle of prototype oscillations. Figure 4.24 shows this average error for a section of the cylinder wake; the errors are relatively small (compared to the velocity vectors of figure 4.18) and so it is asserted that the unforced prototype flow model is a reasonable quantitative model of the cylinder wake during unforced limit cycle oscillations. The power spectral density of a 512 point Hanning windowed time series of the velocity signals, calculated from the flow prototype, is shown in figure 4.25. The figure shows the predicted natural shedding frequency and three higher harmonics of the prototype flow. The frequencies are normalized by the natural shedding frequency of the CFD cylinder wake and thus the figure can be compared with the spectrum obtained from the CFD data ensemble, in figure 4.8. The frequency content of the unforced prototype and the actual unforced wake is similar. Both the growth of instability from the absolutely unstable mean flow, and the resulting limit cycle oscillations of von Kármán vortex shedding for the unforced cylinder flow are therefore modelled adequately by the prototype model. Integration of the prototype model is performed using a variable step size, 4-5th order Runge-Kutta routine coded in the commercially available package MATLAB v4.1 and implemented on a SUN SPARC Station 10. The MATLAB environment also provides access to spectrum analysis routines. A 4-5th order Runge-Kutta integration routine is also coded in C and compiled on a Silicon Graphics Indigo² Extreme. The integration time of the compiled C prototype model is of the order of 30,000 times faster than the original CFD integration. The Silicon Graphics workstation environment is used to generate animated pictures of the prototype model velocity fields.

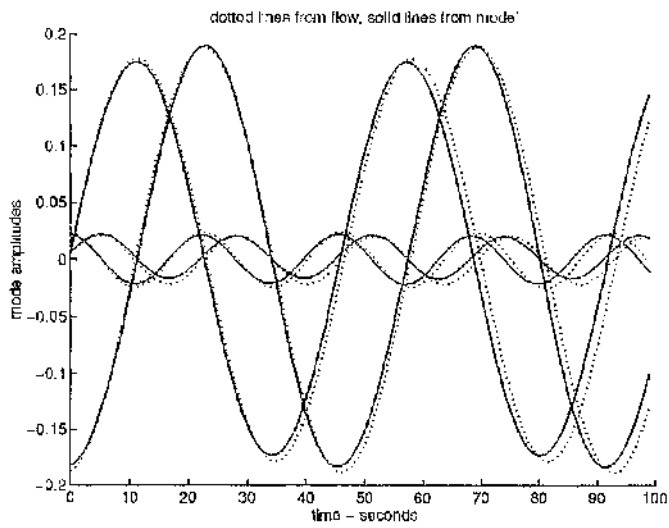


Figure 4.19: Comparison between CFD flow and prototype model: mode amplitudes on limit cycle

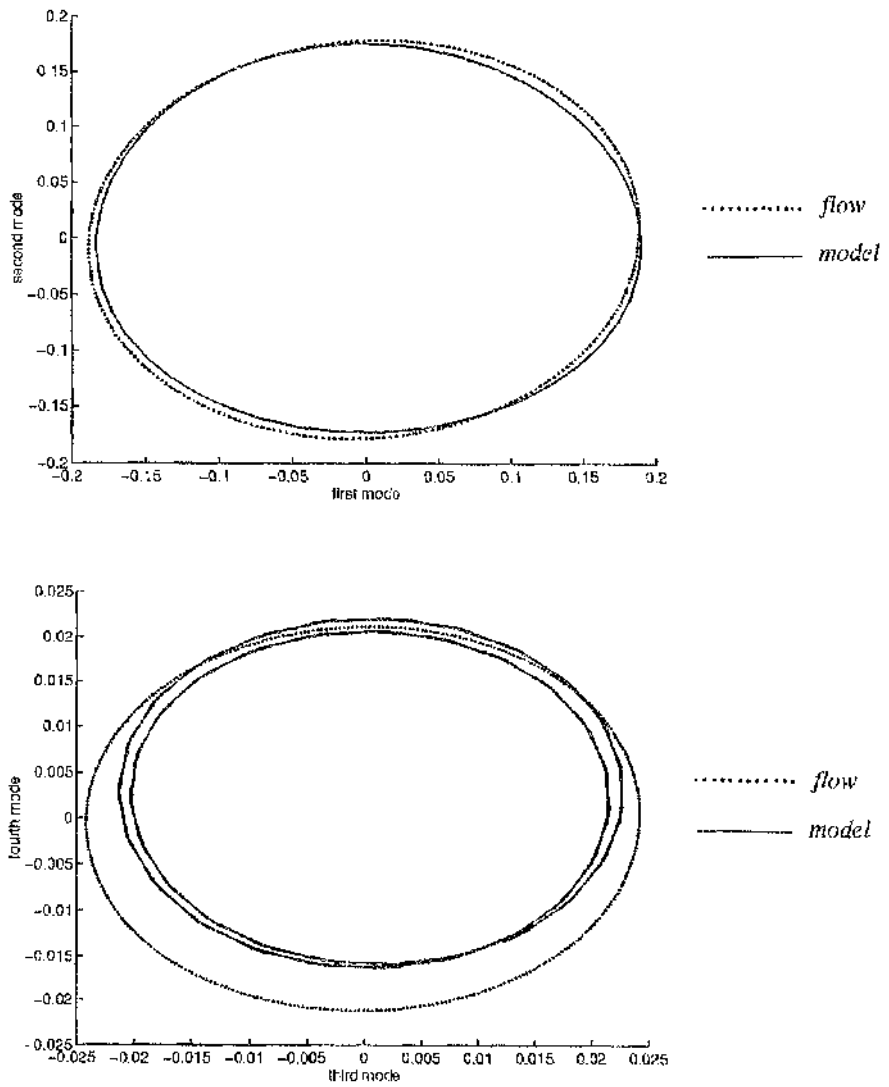


Figure 4.20: Comparison between CFD flow and prototype model: projections of limit cycle

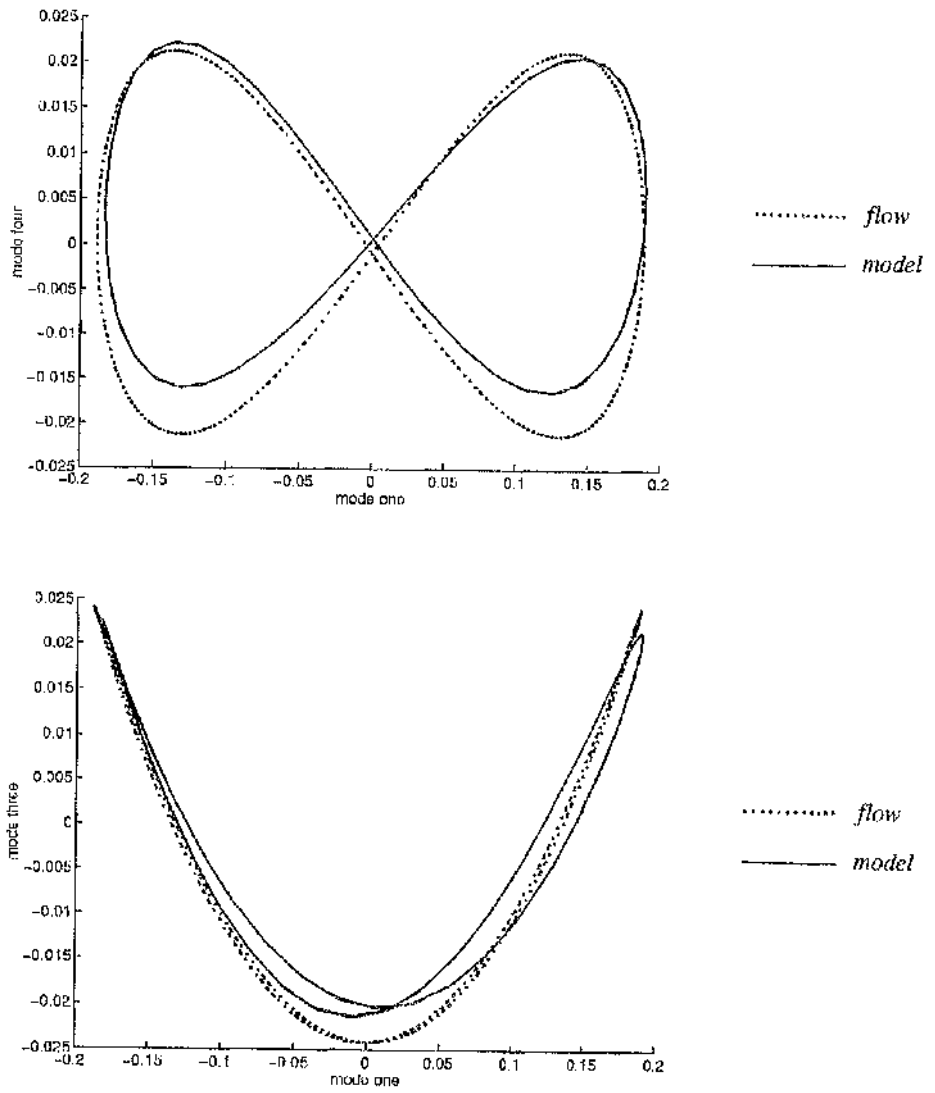


Figure 4.21: Comparison between CFD flow and prototype model: projections of limit cycle

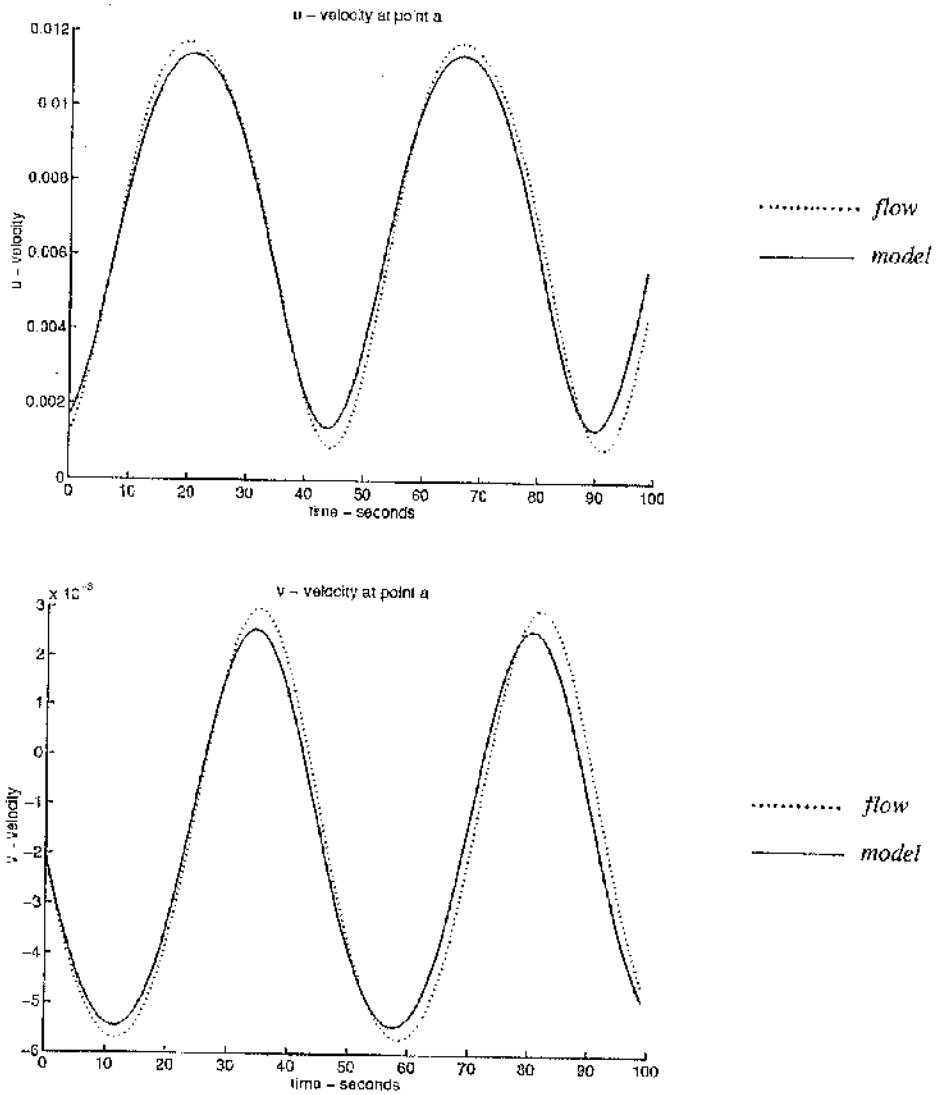


Figure 4.22: Comparison between CFD flow and prototype model: velocity at point a

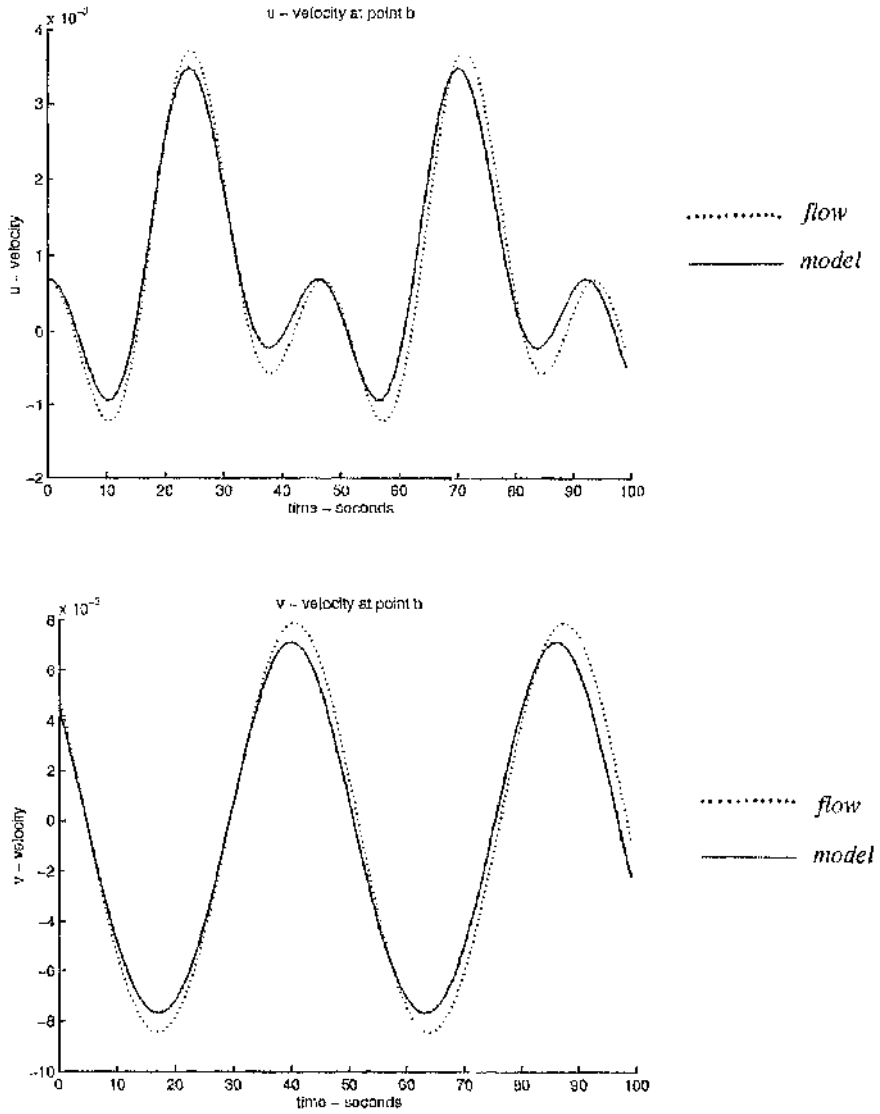


Figure 4.23: Comparison between CFD flow and prototype model: velocity at point b

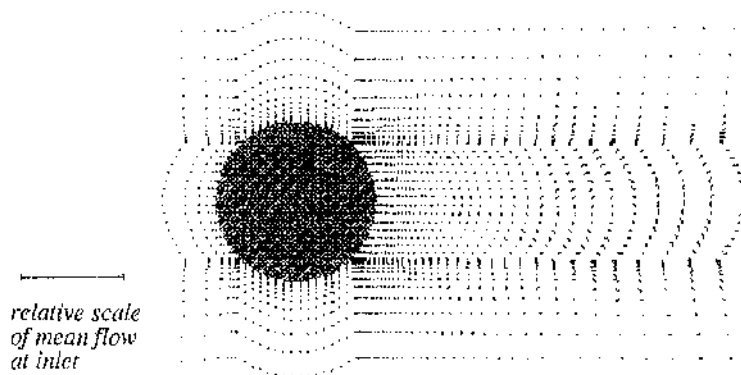


Figure 4.24: Typical section of prototype velocity field error from model

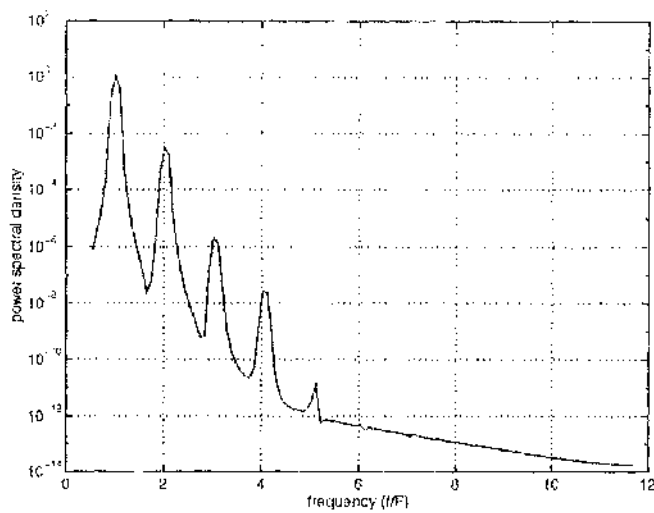


Figure 4.25: Frequency content of limit cycle prototype model oscillations

For the prototype model to be of use in testing the feasibility of the control scheme, however, the response of the prototype to external control forcing has to be correct, at least qualitatively. After integration of the prototype, with harmonic control inputs, qualitative agreement with some of the aspects of experimental cylinder wakes is found. During periodic forcing, the behaviour of the prototype flow is characterized by two states--- lock-in states where the frequency of oscillations shifts to the applied forcing frequency, and non-lock-in states where the frequency of oscillations is a mixture of the applied and natural frequencies, resulting in beating oscillations. These two states are the same kind of states that are observed in actual cylinder wakes [2][9]. Figure 4.26 shows points on the boundary between lock-in and non-lock-in states for the prototype flow model. The points on the figure are the points in control frequency and amplitude phase space where the wake oscillations cease to have a single set of peaks in the power spectrum of velocity signals. The frequency axis is normalized by the natural shedding frequency. The figure therefore represents a lock-in region, or region of entrainment, for periodic forcing of the prototype flow and is in qualitative agreement with the entrainment regions observed in experimental, forced cylinder wakes [23], high order numerical simulations of forced cylinder wakes [2] and entrainment regions predicted by other low-dimensional wake models [11]. The entrainment region obtained via integration of the forced prototype can be compared to figure 4.27 which shows a qualitatively similar entrainment region observed during acoustic excitation of an experimental cylinder wake and also the response of a semi-empirical cubic low-dimensional model of the flow with a simple additive sinusoidal forcing term [11]. The entrainment regions, which are some of the most significant features of the forced cylinder wake [23], are modelled adequately by the prototype (only a qualitative agreement is necessary for initial testing of the control strategy). Figures 4.28 and 4.29 show spectral densities and time histories and phase portraits of velocity signals obtained from integration of the harmonically forced prototype during lock-in and figures 4.30 and 4.31 show the

same portraits of velocity signals obtained during a non-lock-in example. The figures compare very well to similar measurements of an actual cylinder wake [2]. The velocities obtained during lock-in (at an amplitude of 1.0 and normalized frequency of 1.16 in figure 4.26) are similar in character to oscillations during natural shedding (figure 4.28 can be compared with figure 4.22) but have a different amplitude and frequency. The power spectral density during lock-in has well defined peaks and is similar to a shifted spectrum of natural shedding [2]. The dashed line on the power spectrum is the natural shedding frequency; the shedding oscillation frequency is shifted during lock-in. The phase portraits of velocity signals (the same projections that are depicted in figure 4.17) show well defined limit cycles, characteristic of lock-in [2]. Alternatively, the power spectrum obtained during non-lock-in (at an amplitude of 1.0 and frequency of 1.45) is less well defined and shows a multitude of peaks [2]. The time history of a velocity signal shows beating oscillations characteristic of experimental observations of non-lock-in [2]. The phase portraits of velocity signals of the prototype wake do not show simple limit cycles and are dissimilar from the natural shedding phase portraits. The temporal behaviour of the forced prototype flow is therefore also in agreement with experiment.

The spatial structure of the forced prototype is less representative of an actual cylinder wake because the prototype consists of only four spatial modes—many more modes are necessary for the spatial characterization of all of the flow features resulting from external perturbation of the wake. The ability of the prototype model to encapsulate the forced spatial structures of the flow, rather than just the temporal features, is of interest. The stationary POD basis encapsulates a small region of the forced phase space (ie. the region corresponding to the growth of von Kármán shedding). The POD modes satisfy the flow boundary conditions (the control input is significant in the near wake but is almost zero on the domain boundaries. The control input is therefore consistent with the boundary conditions) and the POD modes are orthonormal and satisfy incompressibility. The stationary POD basis can

therefore be expected to provide a useful basis for the approximation of other flow features outwith the characterization ensemble [33] (for example, features of forced flow). However, in the literature, a POD basis consisting of only six modes was deficient at representing a cylinder wake flow at off reference Reynolds numbers [39] (mainly because of the differences in mean flow between different Reynolds number wakes). The four mode, stationary POD basis can thus be expected to provide a rough, qualitative approximation to the velocity fields of forced, non-stationary flows. The four mode description does contain one very important characteristic of actual forced cylinder wakes—the oscillations in the flow are the result of more than one pair of POD modes. The prototype flow therefore retains the feature, of real cylinder wakes, that single sensor measurements do not, in general, contain enough information about all of the modes, unlike multiple sensor measurements. The inferiority of single sensor measurements, compared to spatially distributed sensing is presented in the next section.

In the ideal situation, where non-stationary POD modes are available, the POD modes would incorporate the effects of a control. The control amplitude in a real flow must be limited so that the control does not excite a higher dynamical state (turbulence for example). The control amplitude is also such that the mean flow is not modified significantly by the action of the control. Consequently, the velocity field fluctuations resulting from the control are assumed to be much smaller than the velocity fluctuations resulting from variation of the prototype POD modes. The contribution of the control input to the velocity field is therefore neglected in the velocity field expansion (4.4b).

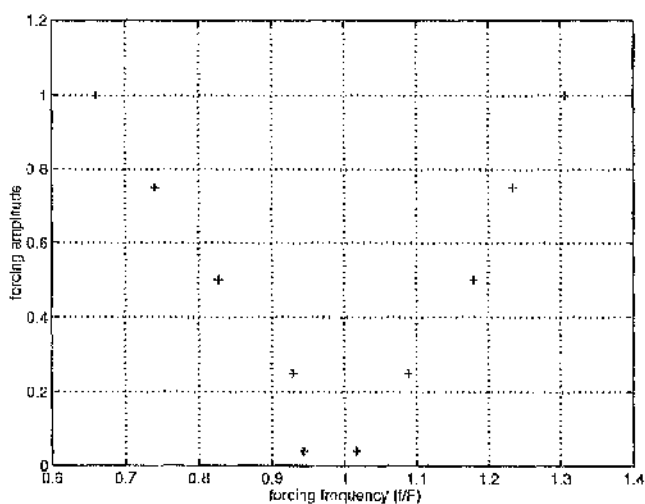
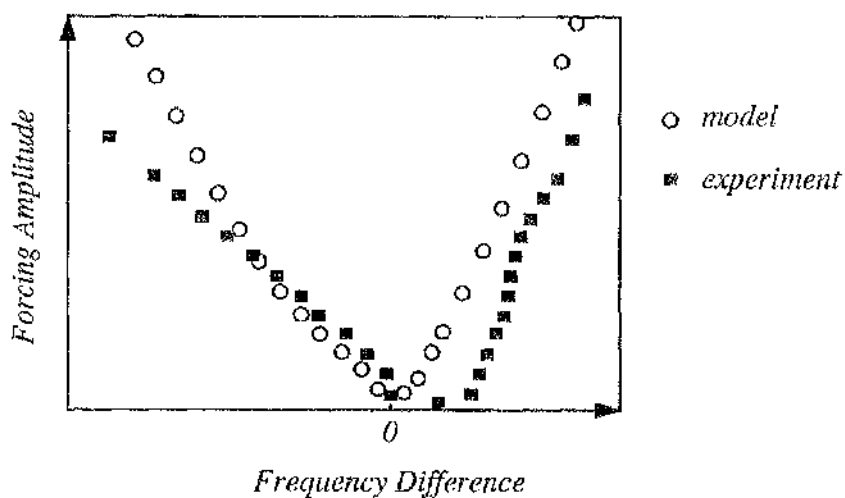


Figure 4.26: Example of prototype forcing entrainment region



Experimental cylinder wake is forced acoustically at $Re = 114$.
 Cylinder model is a semi-empirical ODE with cubic non-linearity and
 an ad hoc additive sinusoidal forcing term. Both results are adapted from [11]

Figure 4.27: Experimental forcing entrainment region

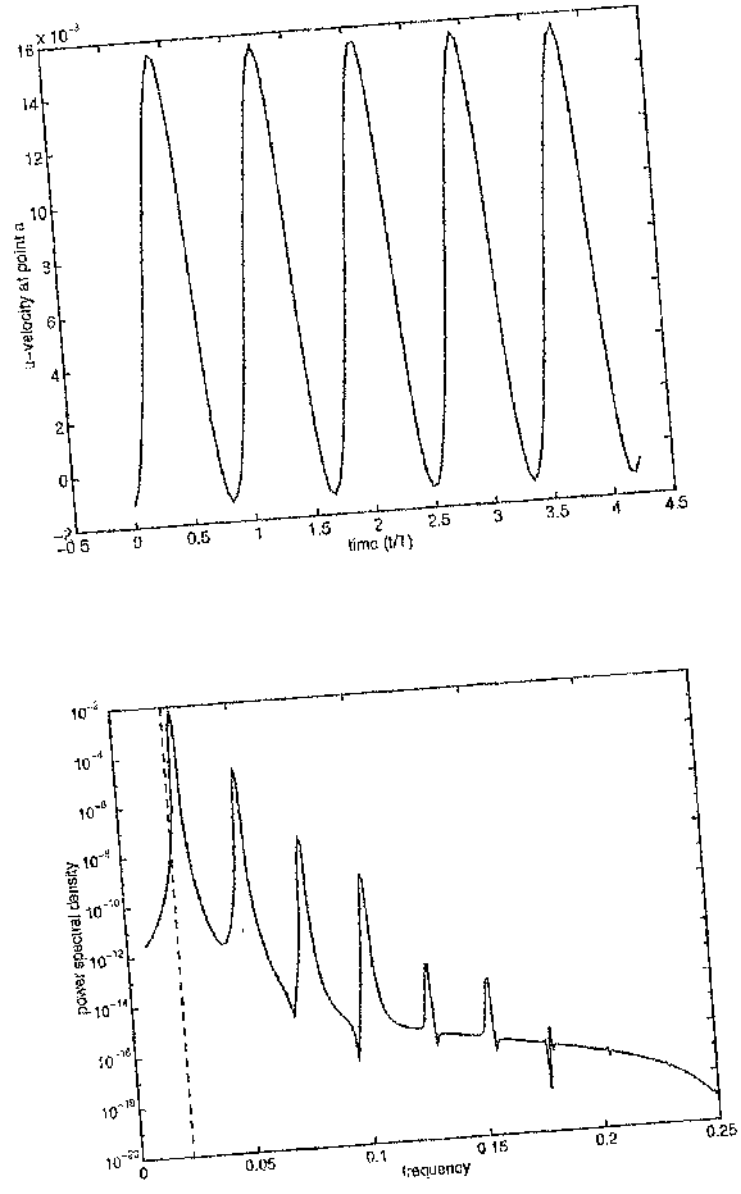


Figure 4.28: Time history and frequency content of velocity signal in prototype model wake during lock-in. Dashed line is natural shedding frequency.

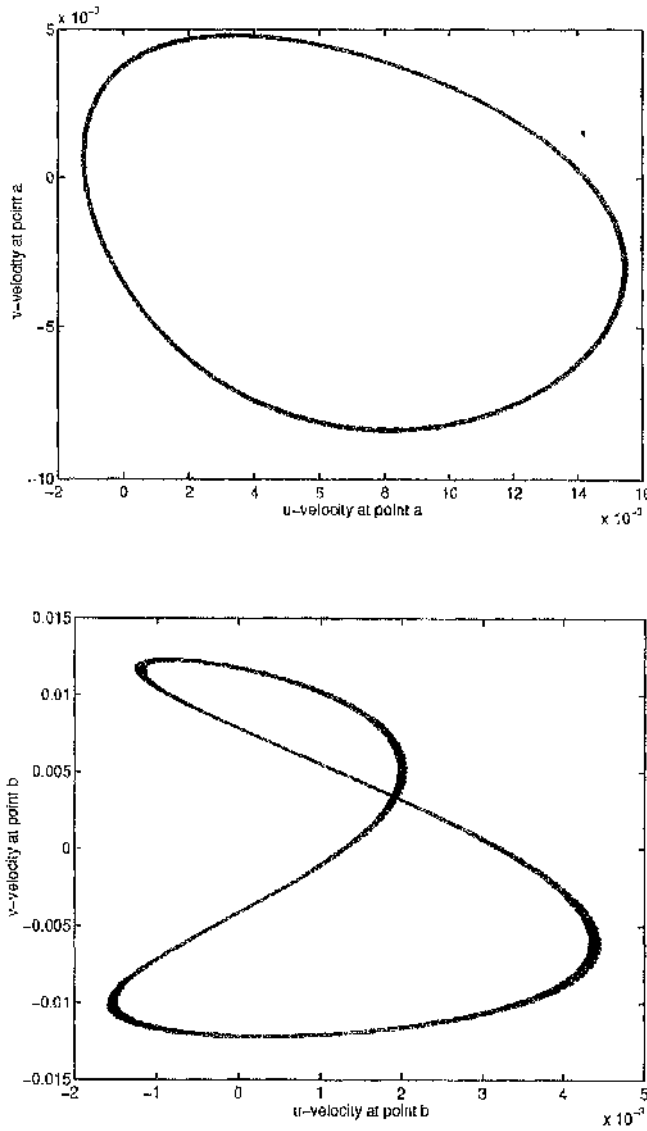


Figure 4.29: Prototype phase portraits of velocity signals during lock-in

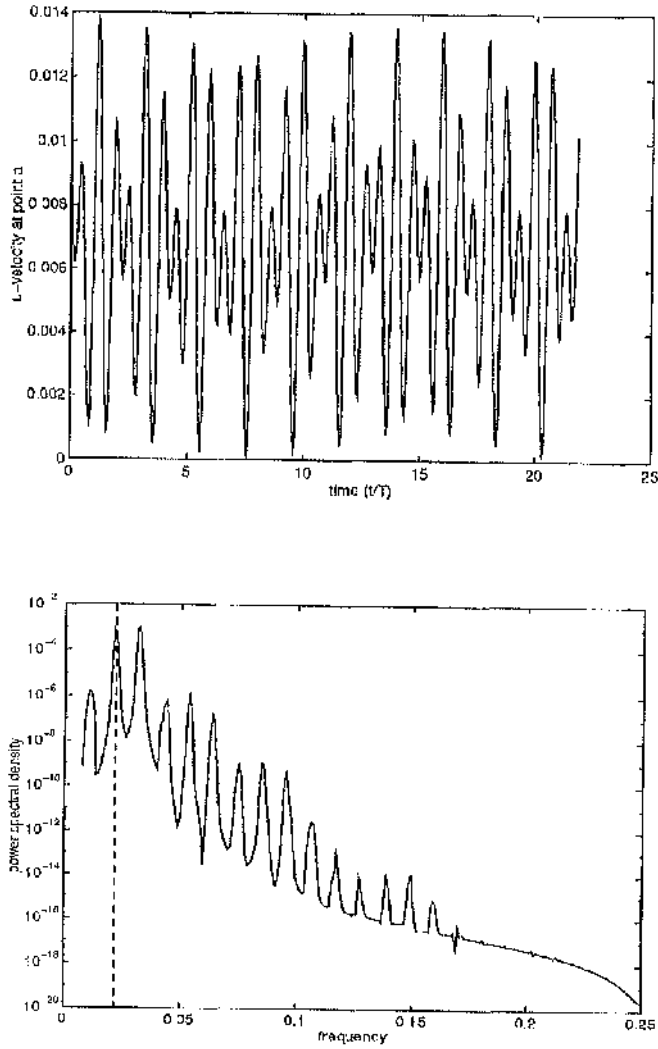


Figure 4.30: Time history and frequency content of velocity signal in prototype model wake during non-lock-in oscillations

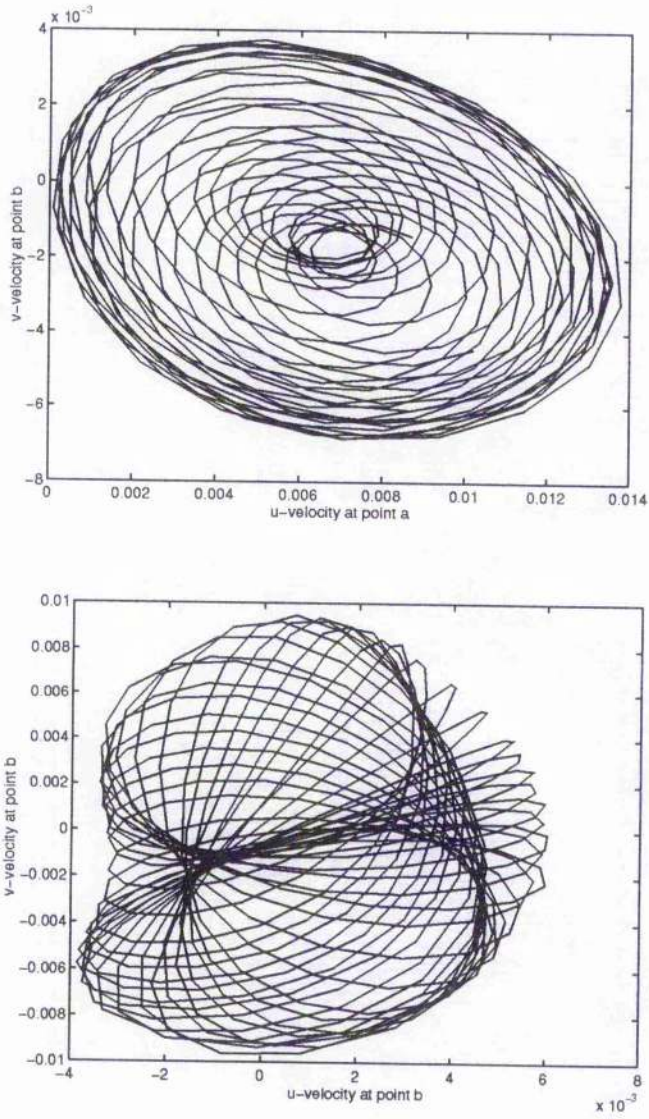


Figure 4.31: Prototype phase portraits of velocity signals during non-lock-in

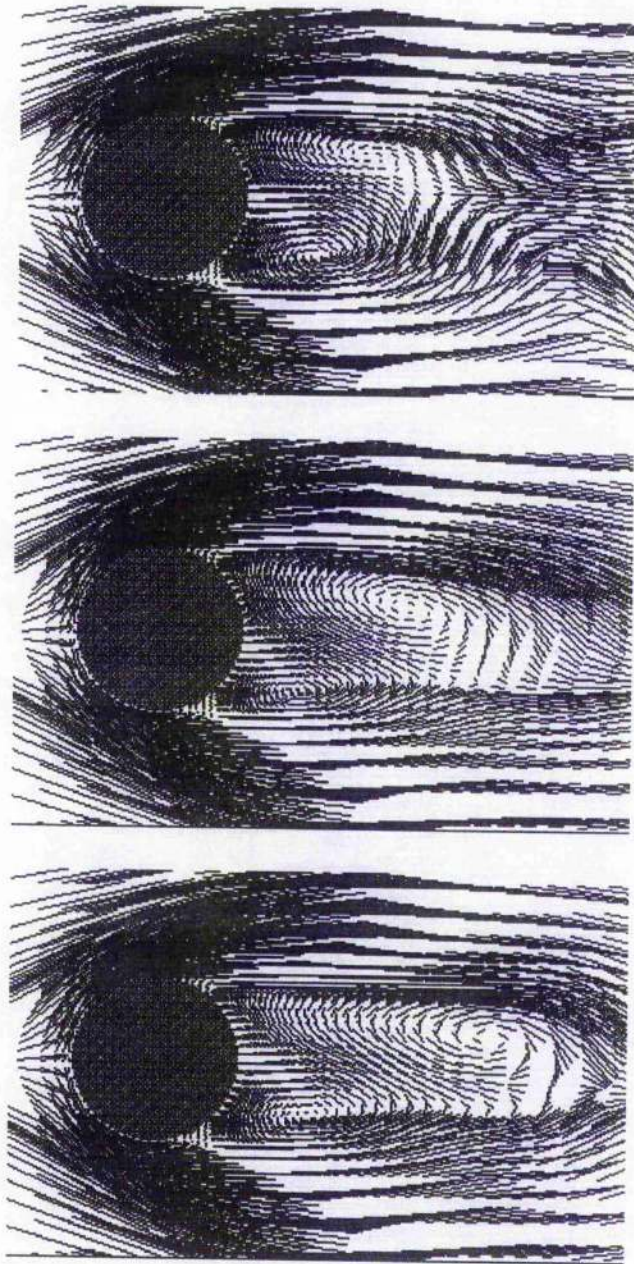


Figure 4.32: Examples of different spatial structure that occur periodically in beating oscillations of the prototype

In summary, the prototype flow model produces, with little computational effort, velocity fields that predict, quantitatively, the spatio-temporal growth of von Kármán vortex shedding behind the cylinder; predict, quantitatively, the spatio-temporal behaviour of the cylinder wake during natural limit cycle oscillations; and predict, qualitatively, the temporal response of the cylinder wake to excitation. The predictions are in agreement with experimental observations of cylinder wakes and with higher order simulations [2][11][10][23][43] [39].

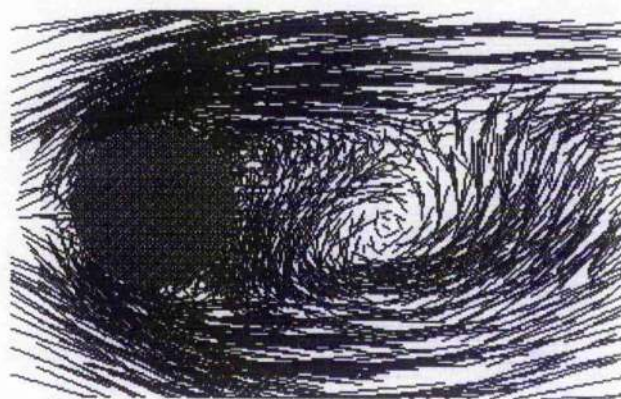
4.4 Control of the Prototype Cylinder Wake

4.4.1 Controller Mode Extraction

The first step in the control strategy is determination of the principal POD modes of the non-stationary prototype velocity fields (obtained from the forced prototype) with a linear neural network. The velocity fields of the prototype flow are sampled at a lower spatial resolution than that of the prototype and random, uniformly distributed, noise is added to the measured velocity fields, to simulate experimental uncertainty. The network data ensemble therefore consists of a series of noisy, low resolution, velocity fields of the forced prototype flow, from which the first two non-stationary modes are extracted for use by the control scheme. These non-stationary modes are termed *controller modes*. The mode extraction is performed on a section of the near wake of the cylinder using a 40×15 regular, Cartesian grid, rather than the 110×60 irregular grid of the entire CFD wake— the mode extraction network is therefore presented with only limited information of the CFD wake, as would be the case in an experiment. As mentioned in Chapter Two, the POD modes are not dependent on the spatial resolution of the flow field, but become progressively coarser as the resolution decreases [36].

The spatial noise field added to the prototype flow field is normally distributed,

and mode extraction is performed on several sets of noisy flow field ensembles, with different noise variances, to determine the effect of random uncertainty on the mode extraction network. Figure 4.33 shows a section of noisy velocity field with a medium level of variance. This corruption of the velocity field is used to introduce some uncertainty, which is likely to exist (in some form) in an experiment, into the flow field measurements. The random corruption is not meant to be representative of any particular fluid mechanical noise (turbulence for example is not random) but is introduced to check the robustness of the characterization and control strategy. (The actual sources of noise in an experimental flow derive from environmental, acoustic noise, electrical noise in measurement apparatus, transition to turbulence and if, for example, smoke flow is used to visualize the flow, then uncertainty is introduced because the smoke particles do not follow the flow exactly.) The mean (training ensemble average) flow field is subtracted from each member of the ensemble, which is then presented to the network. The learning rate is necessarily small, ($\eta = 0.001$), for stability.



velocity field with medium noise level
(normalized variance = 0.0685)

Figure 4.33: Typical noise corrupted velocity field

The structure of the velocity field is affected adversely by addition of the noise, but the first two modes developed for velocity fields that are noise-free, or have

a medium or high noise variance *show no significant differences*: the lower energy modes are neglected and so the mode extraction network acts as a *noise filter* and extracts only large scale coherent structure, neglecting the noise which has low energy and is uncorrelated. Contours of velocity magnitudes in the first two controller modes are shown in figures 4.34 and 4.36. Surface plots of velocity magnitude of these two modes are shown, relative to the cylinder position, in figures 4.35 and 4.37. The modes consist only of large scale structure.

The time varying mode amplitudes are output by the mode extraction network on input of a time dependent velocity field. Time histories of the two controller mode amplitudes are shown in figure 4.38 for time varying velocity fields measured with varying degrees of uncertainty. The addition of noise is seen to have only a small effect on the calculation of the mode amplitudes.

An important advantage of a control algorithm that is based on a distributed measurement over a control algorithm that is based on a single point measurement of the prototype flow is seen in figure 4.40, parts (i) and (ii). The position of this measurement point is shown relative to the cylinder in figure 4.39. The first time history, in part (i) of the figure, shows the natural oscillations of the prototype modes. The next two time histories of part (i) of the figure show, respectively, the measured controller modes and a particular point velocity measurement (point c in figure 4.39) of the prototype flow during these natural oscillations. It could be conceived (from figure 4.40(i)) that feedback of the single velocity measurement would be able to suppress the prototype oscillations. However, the prototype modes contain several points at which one of their velocity components is zero (or very close to zero). A single velocity measurement at one of these points will *not* be able to detect any oscillations of that prototype mode. The point velocity measurement, in figure 4.40 part (ii), is chosen to illustrate this lack of complete information— at this point the u-velocity contributions of both the third and fourth prototype modes are very small ($< 10^{-6} \times$ the mean flow value). Oscillations, consisting purely of

prototype modes three and four, are shown in the first time history of figure 4.40 part (ii). These oscillations are detected by the oscillations of the controller modes (shown in the second time series of figure 4.40 part (ii)) but are not detected using the single point measurement (shown in the third time series of figure 4.40 part (ii)). A control algorithm based on a single point measurement of the prototype flow is unable, in general, to completely control the prototype wake oscillations (as is the case in a real absolutely unstable flow).

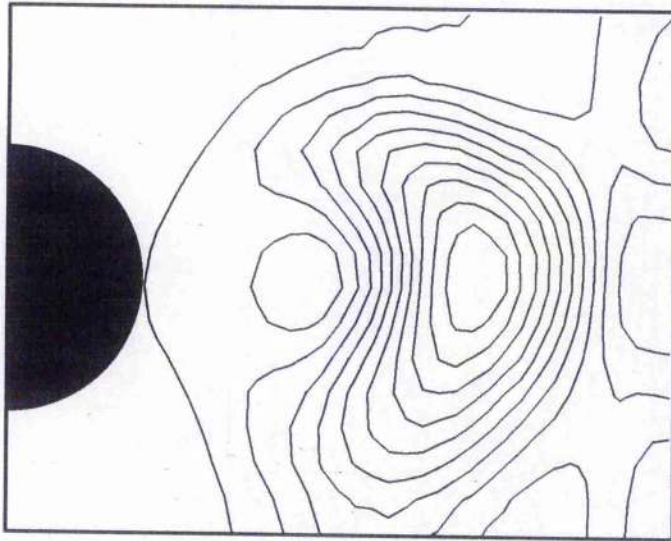


Figure 4.34: First controller mode: contour of velocity magnitudes

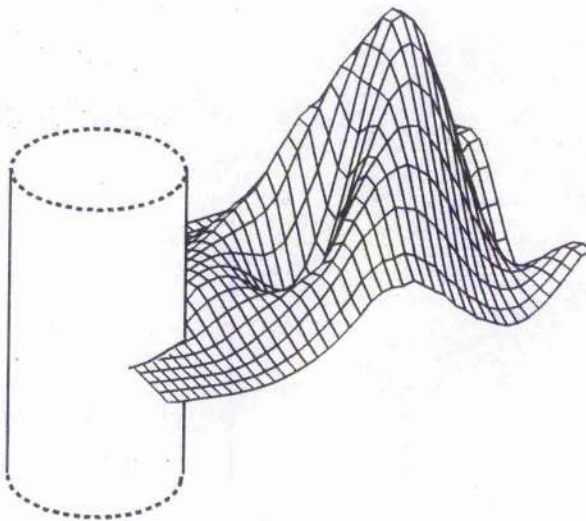


Figure 4.35: First controller mode: surface of velocity magnitudes

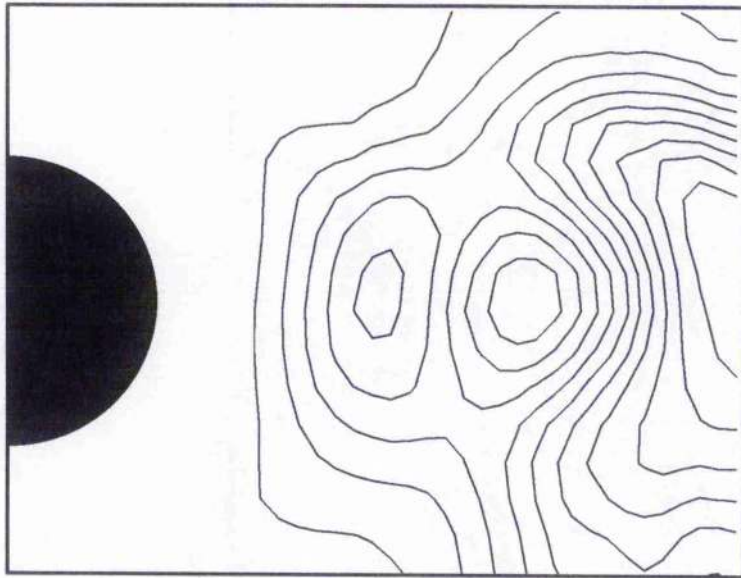


Figure 4.36: Second controller mode: contour of velocity magnitudes

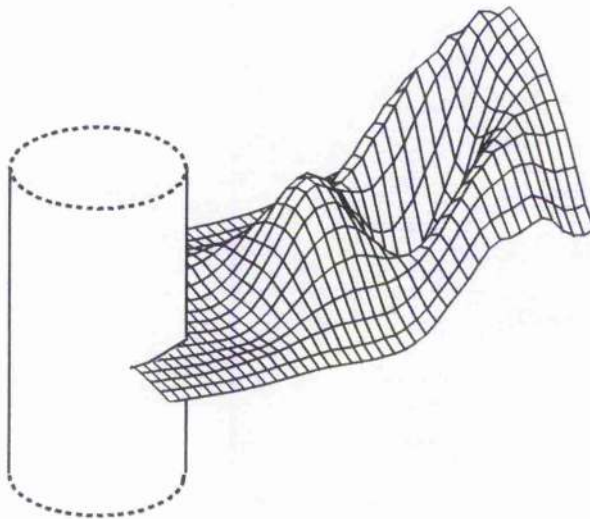


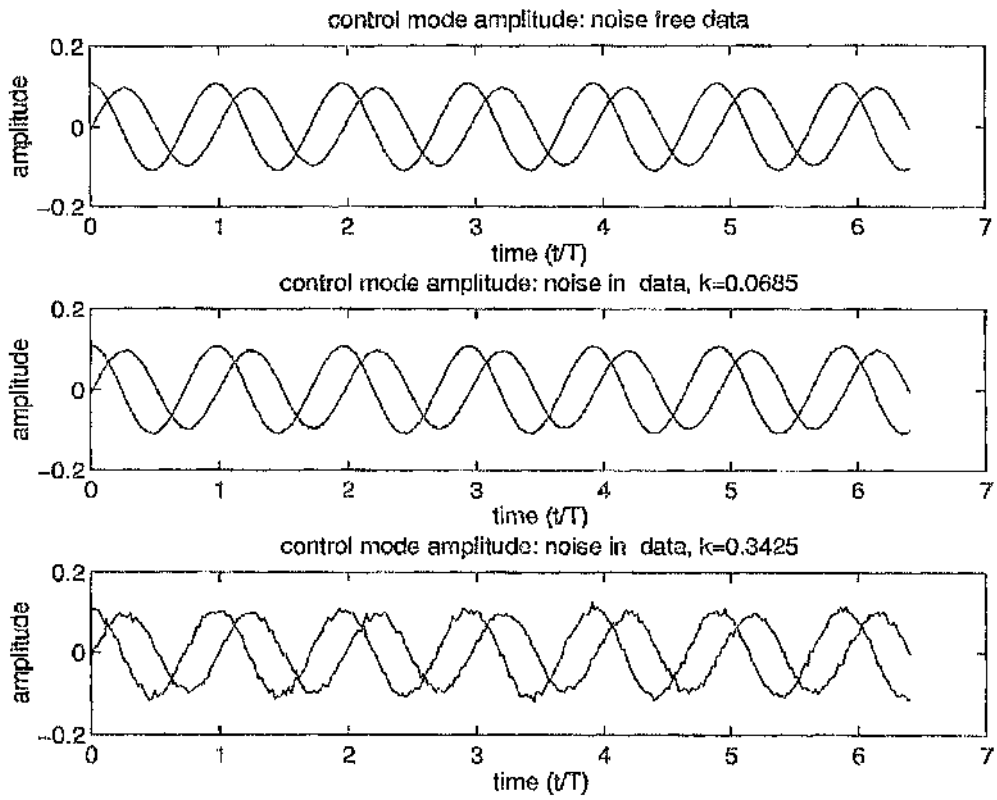
Figure 4.37: Second controller mode: surface of velocity magnitudes

4.4.2 Non-linear Prediction of the Prototype Flow Response

The observed response of the controller modes to excitation of the prototype flow is used to train a non-linear neural network emulator that forms the core of the control strategy. The prototype flow is subjected to uniformly distributed, random bursts of control input at various amplitudes. The control input is discrete, and each control input lasts for a tenth of a flow period. After the addition of the control the prototype flow is integrated for one tenth of a flow period and the flow field is measured and input, along with random uncertainty, to the mode extraction network. The mode extraction network supplies the controller mode values after the addition of the control input. The training ensemble for the neural emulator consists of a time series of present controller mode amplitudes (measured from a velocity field ensemble with a medium noise level), the value of the present control, and the future controller mode amplitude after one tenth of a flow period. The emulator time-step, of one tenth of a flow period, is chosen to be reasonably small to provide accuracy but large enough so that a linear model of the flow would not suffice. It is preferable that the time-step is reasonably large (a real controller requires a finite time within the time-step value to perform computations and actuate the control mechanism). The random control bursts used to excite the prototype flow are shown in figure 4.41. The bursts are of differing maximum amplitude, as it is not known, prior to a control simulation, what amplitude range is necessary for control of the flow. The amplitude range of the control input is, however, limited to a small finite value as would be the case in a real flow. In a real flow the control amplitude is limited so that the unstable global modes are stabilized without modification of the mean flow and so that a higher dimension dynamical state (turbulence for example) is not excited.

Several different sizes of multi-layer perceptron are tested for emulation of the controller mode response. The least restrictive network architecture is a three layer

multi-layer perceptron with a linear output layer, as the network output range is not limited and two non-linear layers are adequate for modelling the non linear mapping between the present and future states of the controller modes. The smallest, and therefore best, network that produces results consistent with the training data is a 4/12/2 network. For comparison, an 8/24/2 network and a 16/48/2 network are also trained to emulate the training data. The larger networks, however, take significantly longer to train. While the generalization of the 4/12/2 network is quite good, the generalization of the 8/24/2 network and the 16/48/2 network is poor (ie. only the 4/12/2 network performs well on data outwith the training set). Because the chosen 4/12/2 network contains relatively few weights, and only predicts the system state at the next time-step, network training is quite fast. The network achieves a specified error goal, such that the sum of the squared output error is less than 0.001, after 267 cycles, starting from small, random weights, through the 1000 member training ensemble. The network is trained using an adaptive learning rate, which changes to provide fast, but stable, learning, and a momentum term of 0.95 which speeds up convergence. The training record for the emulator network is shown in figure 4.42. The network error is still decreasing when learning is stopped— the network could therefore fit the training data better, but learning is stopped prematurely so that the network does not learn any noise in the training data. The prediction of the controller mode amplitude response, compared to the actual response is shown, for velocity fields that are not training ensemble members, in figures 4.43 and 4.44. The prediction of the response of the randomly forced prototype flow is seen to be quite good, and has little error.



$$k = \text{noise variance}/\text{mean flow value}$$

Figure 4.38: Time history of controller mode amplitudes for low, medium and high noise levels

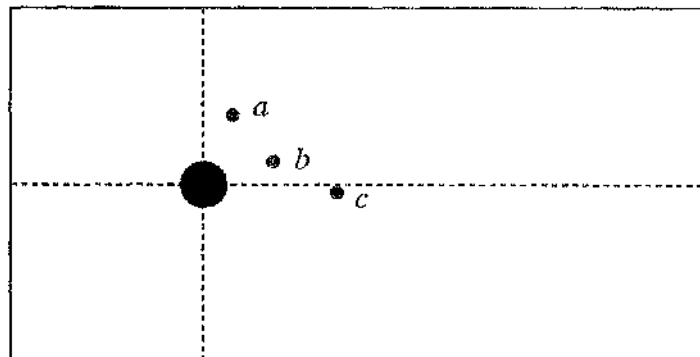


Figure 4.39: Points a,b and c used for single point measurements of the prototype flow

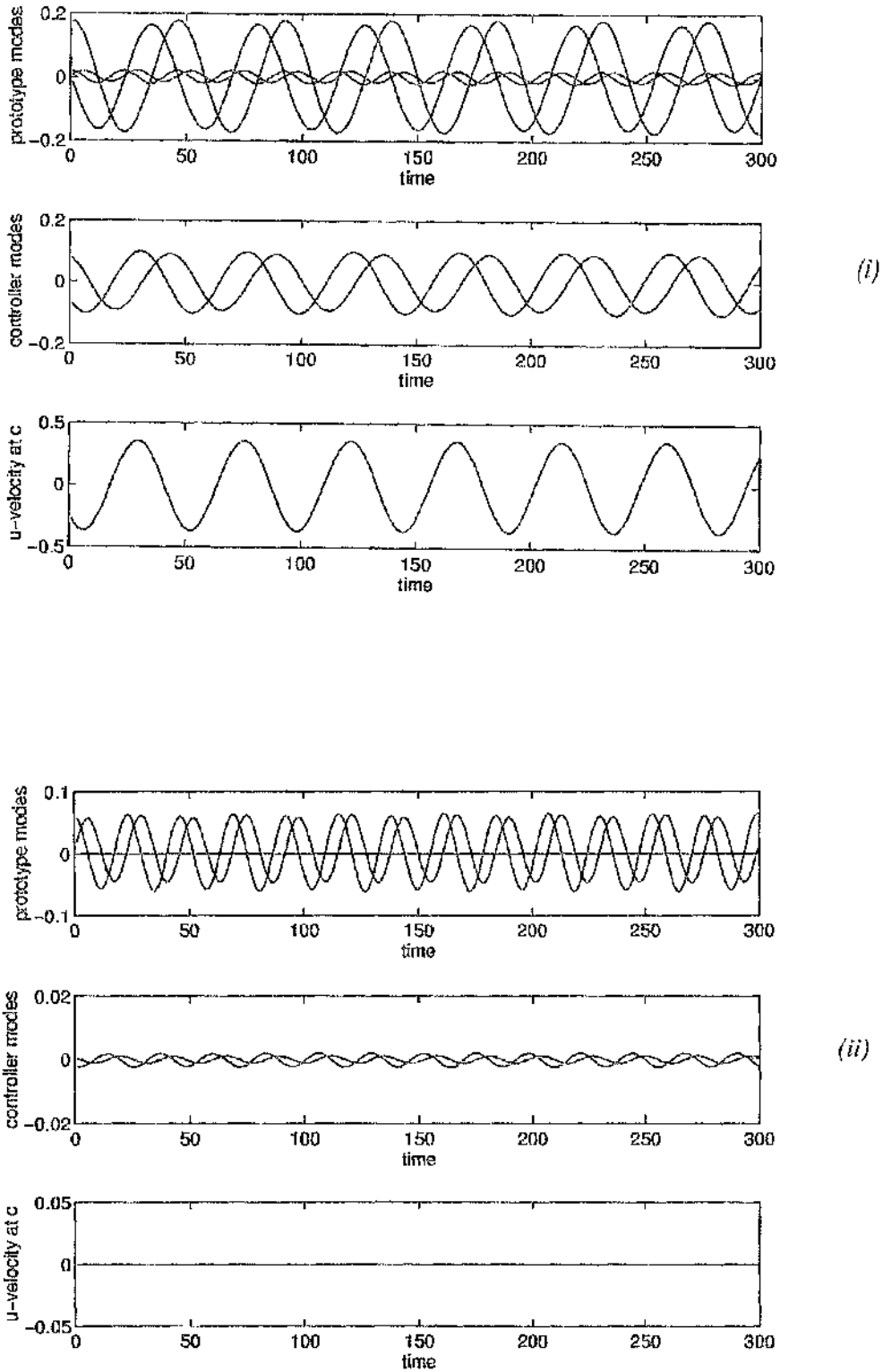


Figure 4.40: Comparison between single and mode amplitude measurements of the prototype wake

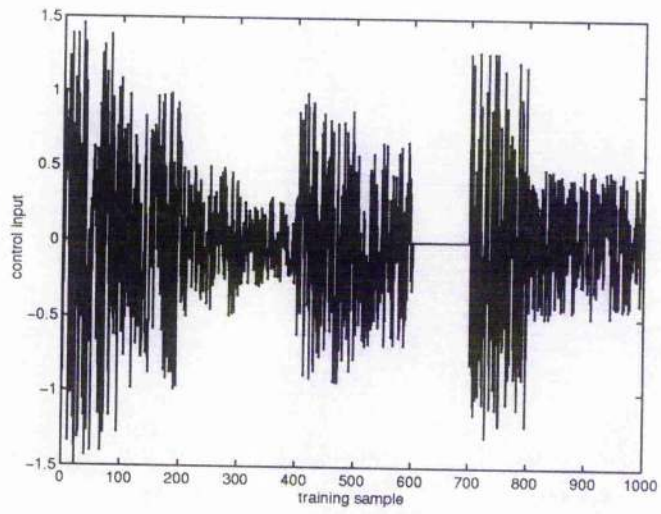
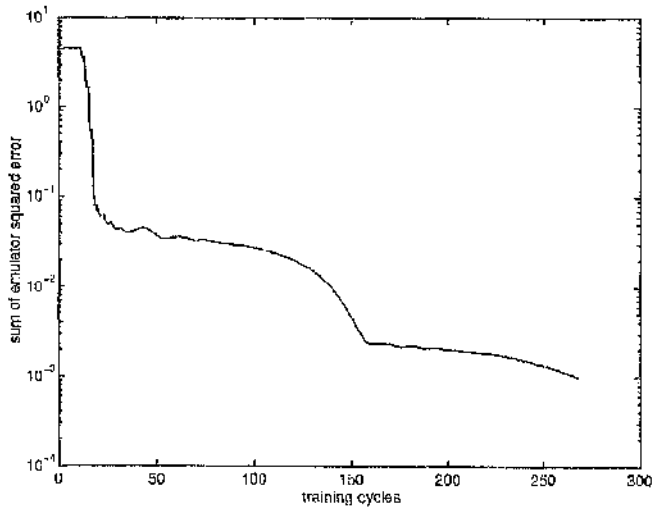
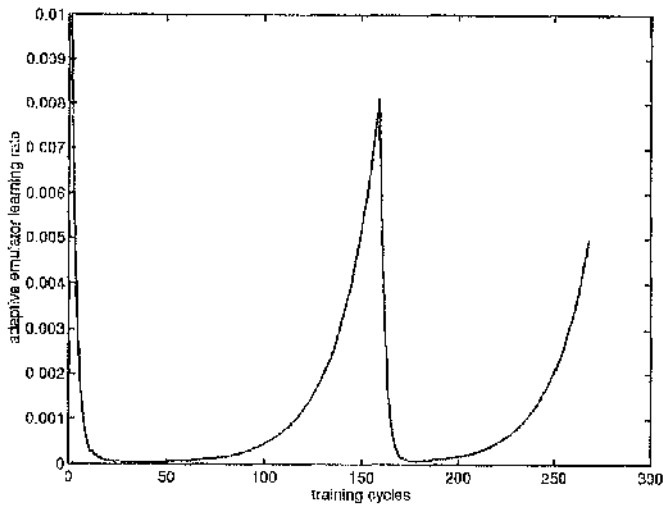


Figure 4.41: Control input for emulator training



neural emulator error



emulator learning rate

Figure 4.42: Neural emulator training error and adaptive learning rate

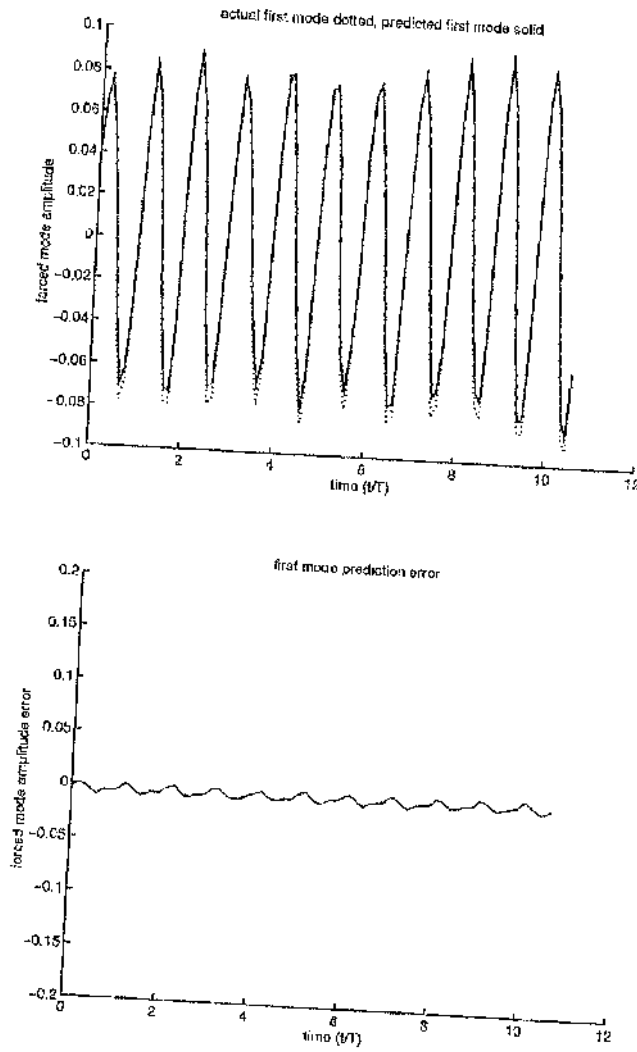


Figure 4.43: Neural emulator prediction of first controller mode amplitude response

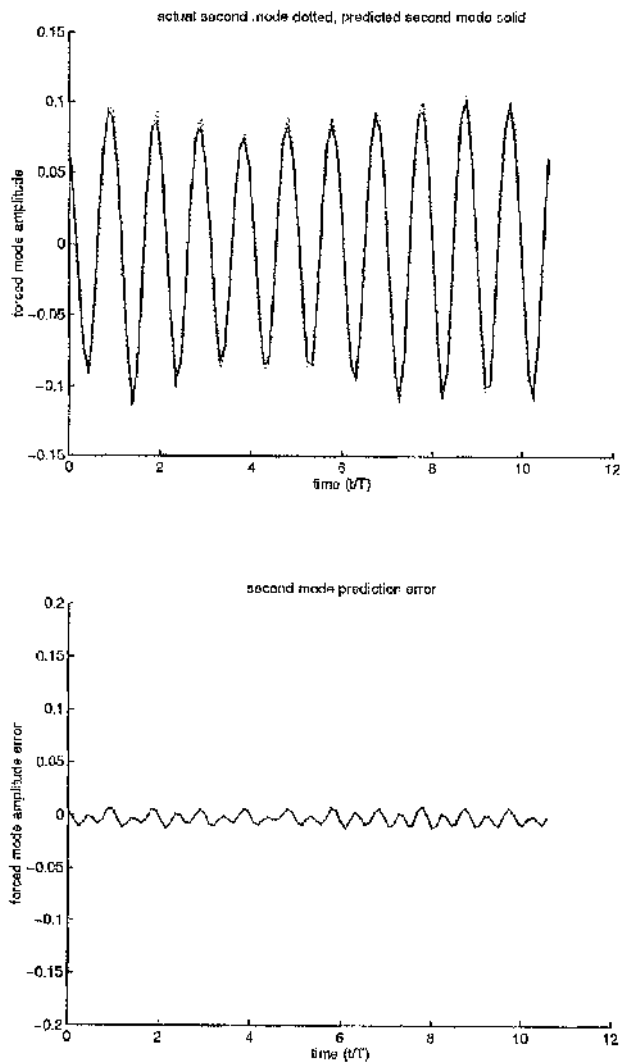


Figure 4.44: Neural emulator prediction of second controller mode amplitude response

4.4.3 Non-linear Adaptive Control of the Prototype Flow

Adaptive control of the flow is performed by construction of the non-linear control scheme in figure 3.8. A small, two layer (and hence easy to train) non-linear network is used to provide the control input to the prototype flow and to the emulator, given the present amplitudes and a measure of the error in the applied control. The controller, being a non-linear network, has a maximum output amplitude of ± 1 . The initial controller weights are selected randomly but are set small so that the initial control guess does not adversely affect the flow. The learning rate of the controller is set relatively large so that the control adapts quickly. The difference between the predicted mode amplitudes and the desired zero state is backpropagated through the emulator, with its weights held fixed, and then backpropagated through the controller, whose weights are updated in order to provide a better control. The control is input to the prototype flow and the control simulation proceeds to the next time step. The controller therefore learns adaptively to provide a control that is a function of the present controller mode amplitudes and the backpropagated error between the modes and a desired state.

A typical control simulation, incorporating measurement uncertainty, is shown in figure 4.45. The control simulation is implemented within the MATLAB framework which has a built in 4-5th order Runge Kutta integration routine. Emulator and controller training is performed using a combination of compiled C routines and the MATLAB Neural Network Toolbox. After time-histories of the mode amplitudes are obtained from MATLAB, animated velocity fields of the control run are generated using a Silicon Graphics workstation. Figure 4.45 shows the four modes of the prototype flow (which represent the cylinder wake). Control is switched on after six limit cycle oscillations (delimited by the first large tick mark on the time axis). After a further thirty periods of oscillation the flow oscillations in the flow field are very small and vortex shedding is suppressed. After stabilization of the vortex shedding

the control input necessary to maintain stability is only enough to stabilize disturbances due to the background noise in the flow. The qualitative nature of the control input can be compared to the experimental flow control results of [7]. The control is switched off after the second tick mark on the time axis (after approximately six hundred controller steps, or a further sixty four flow periods). The oscillations grow exponentially after switching off the control. Phase portraits of the prototype modes during a control run are shown in figure 4.49. The prototype flow field that results from the control scheme is seen to be almost indistinguishable from the mean flow (figure 4.50). The control time history is shown in figure 4.46, and the control system error is shown in figure 4.47. The control input is markedly non-linear at the start of the control run, when the mode amplitudes are large (shown in figure 4.48), but is almost harmonic towards the end of the run, when the mode amplitudes are small (also shown in figure 4.48). The initial non-linear control suggests that a linear control method would take much longer to control the flow. Indeed a similar control strategy based on a linear emulator and linear controller takes significantly longer to suppress the flow than the non-linear scheme. The performance of an adaptive *linear* control scheme is shown in figure 4.51. The linear control strategy is similar to the non-linear scheme except that the emulator is a single linear layer of neurons, and the controller is a single linear neuron. The linear emulator provides only a linear approximation of the non-linear response of the flow to control forcing. For large time-step values, a linear prediction of the mode amplitude response is inaccurate. The linear controller output is therefore deficient in controlling the flow when the mode amplitude response is significantly non-linear (ie. when the mode amplitudes are large).

4.5 Summary

A non-linear, low-dimensional model with an artificial forcing term is used as a prototype absolutely unstable flow. The prototype flow achieves good agreement with unforced cylinder flow solutions obtained by high order numerical simulation. The prototype also captures some of the qualitative features of experimental, forced cylinder wakes. The prototype is used to produce artificial, or simulated, non-stationary velocity fields for characterization by the controller. The controller is assumed to have only limited information about the flow (ie. it is given lower resolution, noisy data and only two controller modes, rather than four modes, are extracted). Nevertheless, the non-linear emulator predicts the flow dynamics successfully and the non-linear controller suppresses the oscillations representative of vortex shedding. The controller is seen to be superior to linear control and superior to single sensor control.

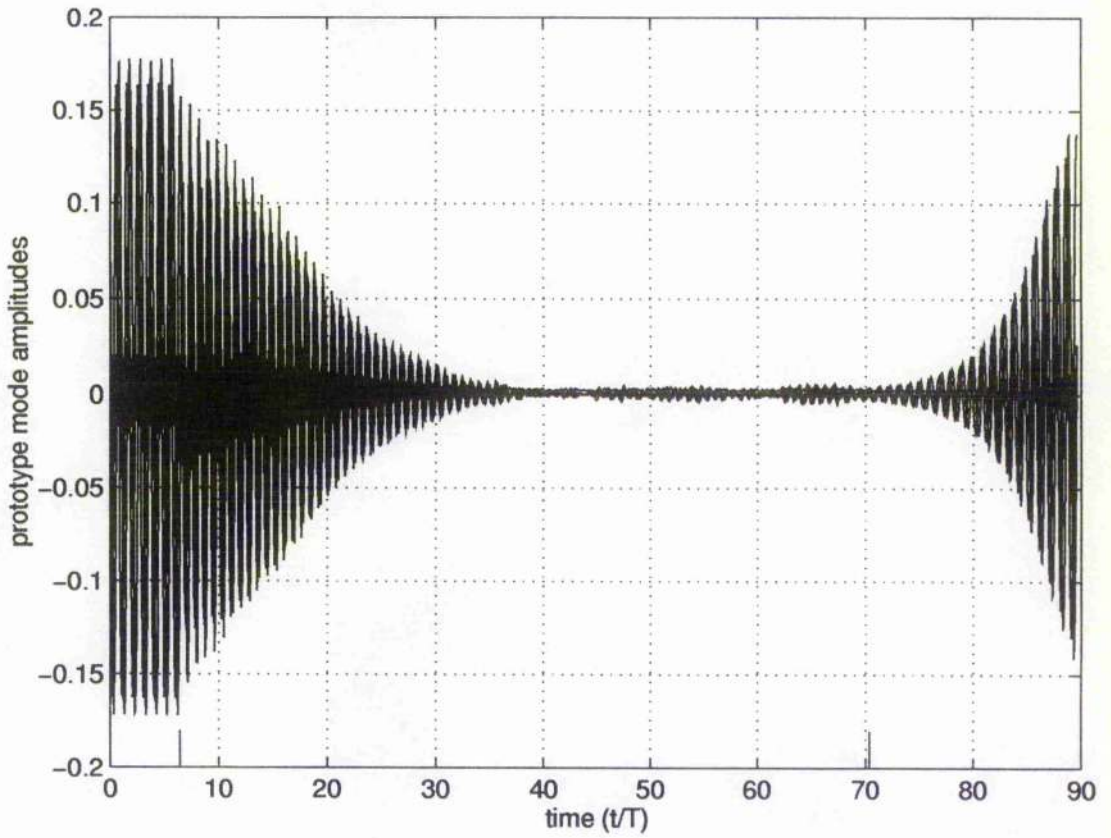


Figure 4.45: Prototype flow response during a control run: control switched on after six limit cycle oscillations

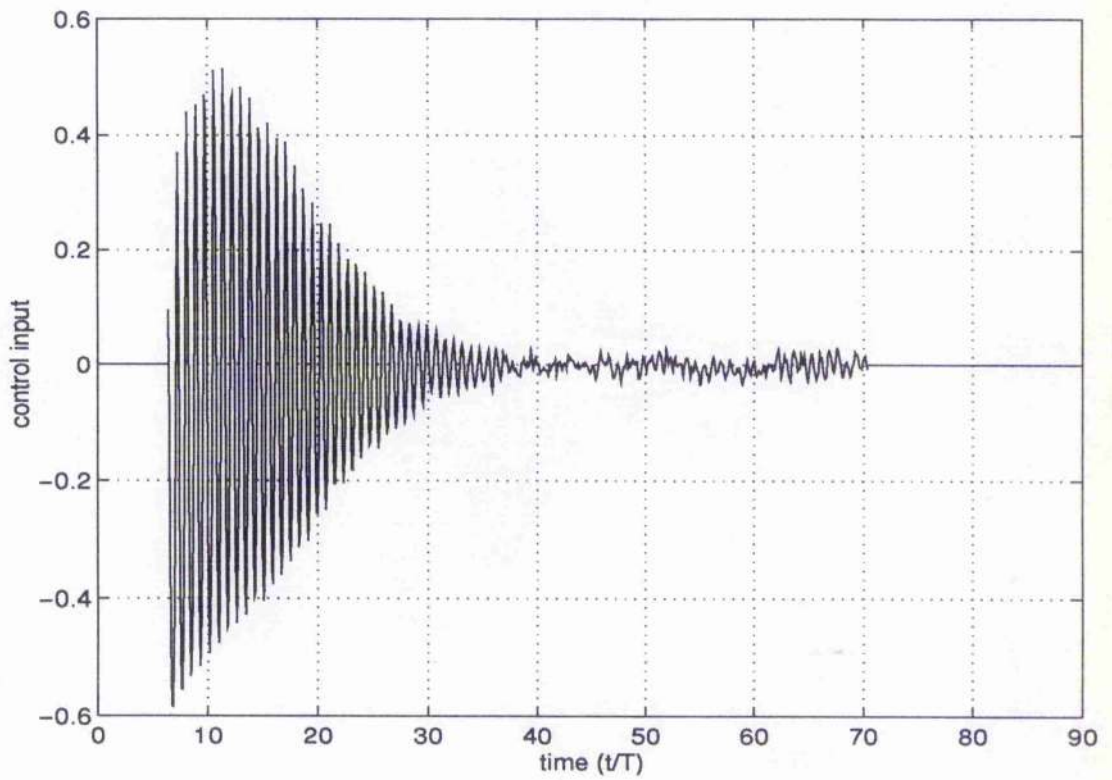


Figure 4.46: Control input during a control run: control switched on after six limit cycle oscillations

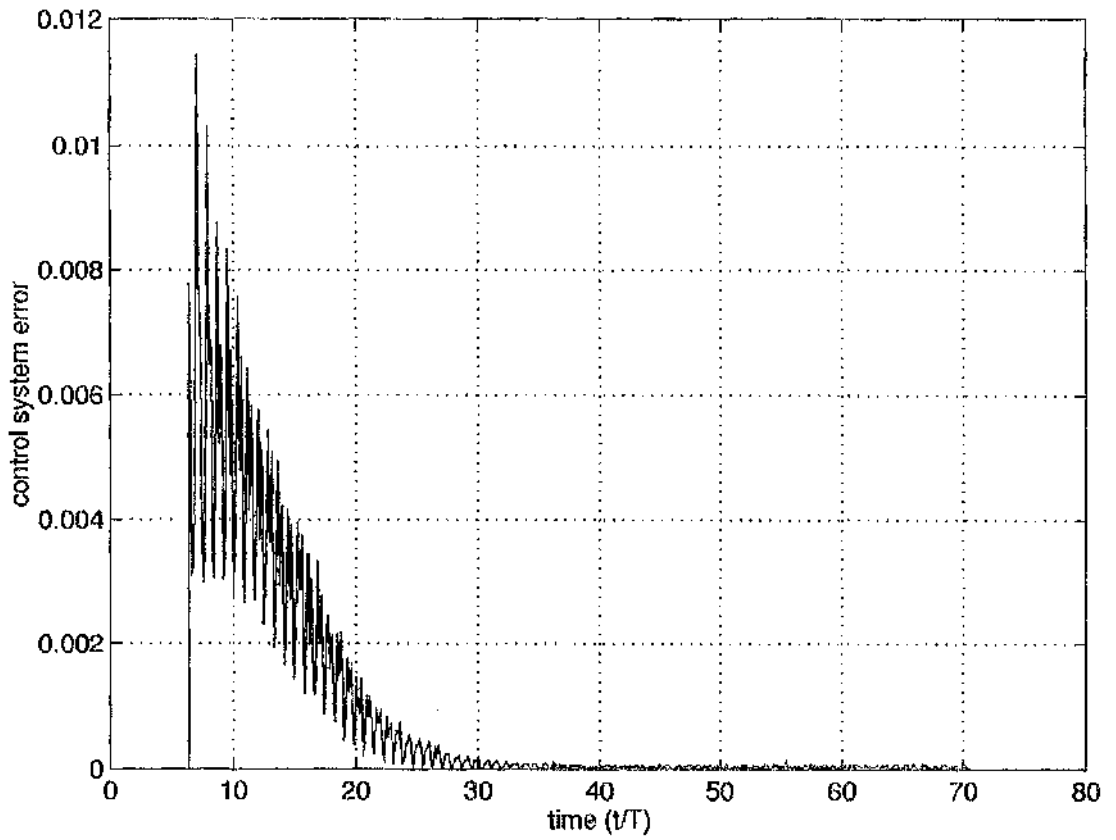


Figure 4.47: Control system error during a control run: control switched on after six limit cycle oscillations

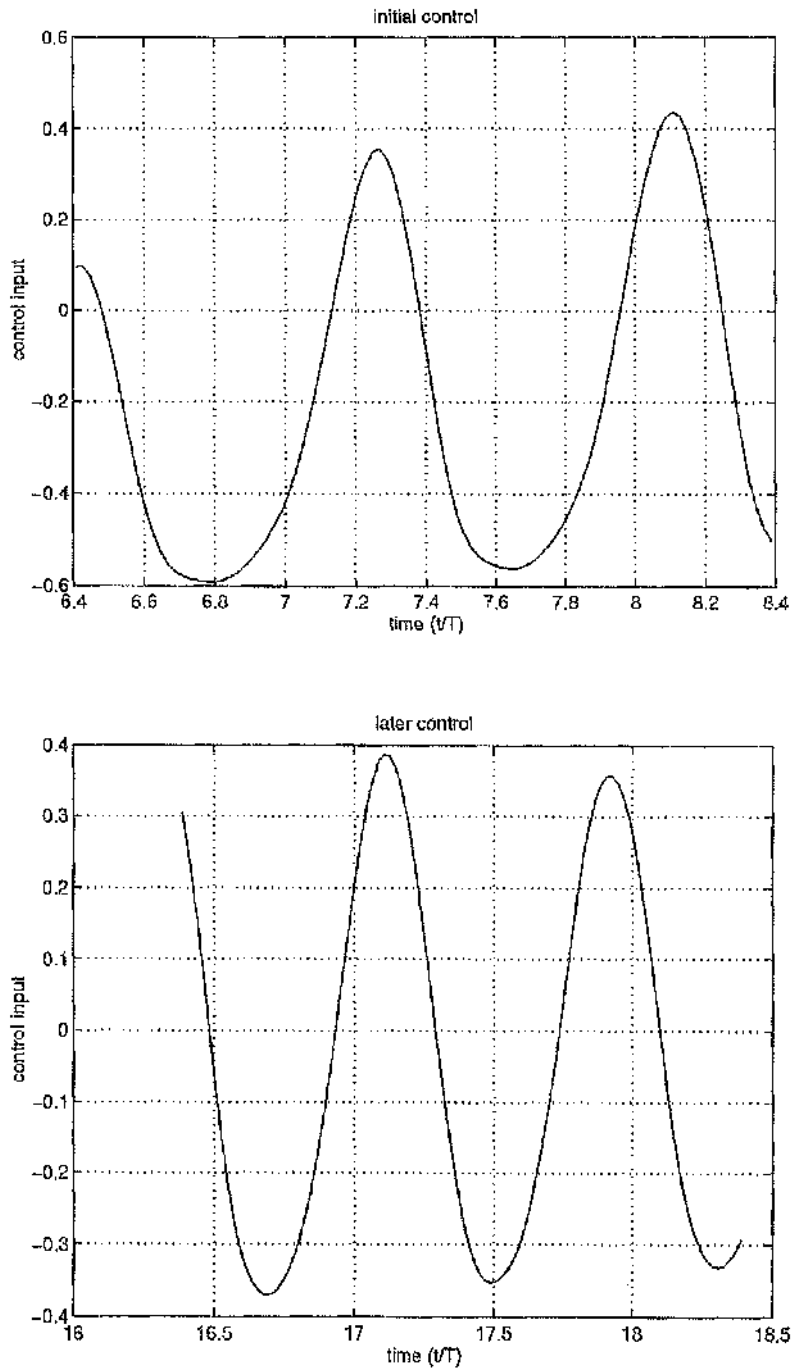


Figure 4.48: Close-up of non-linear controller history

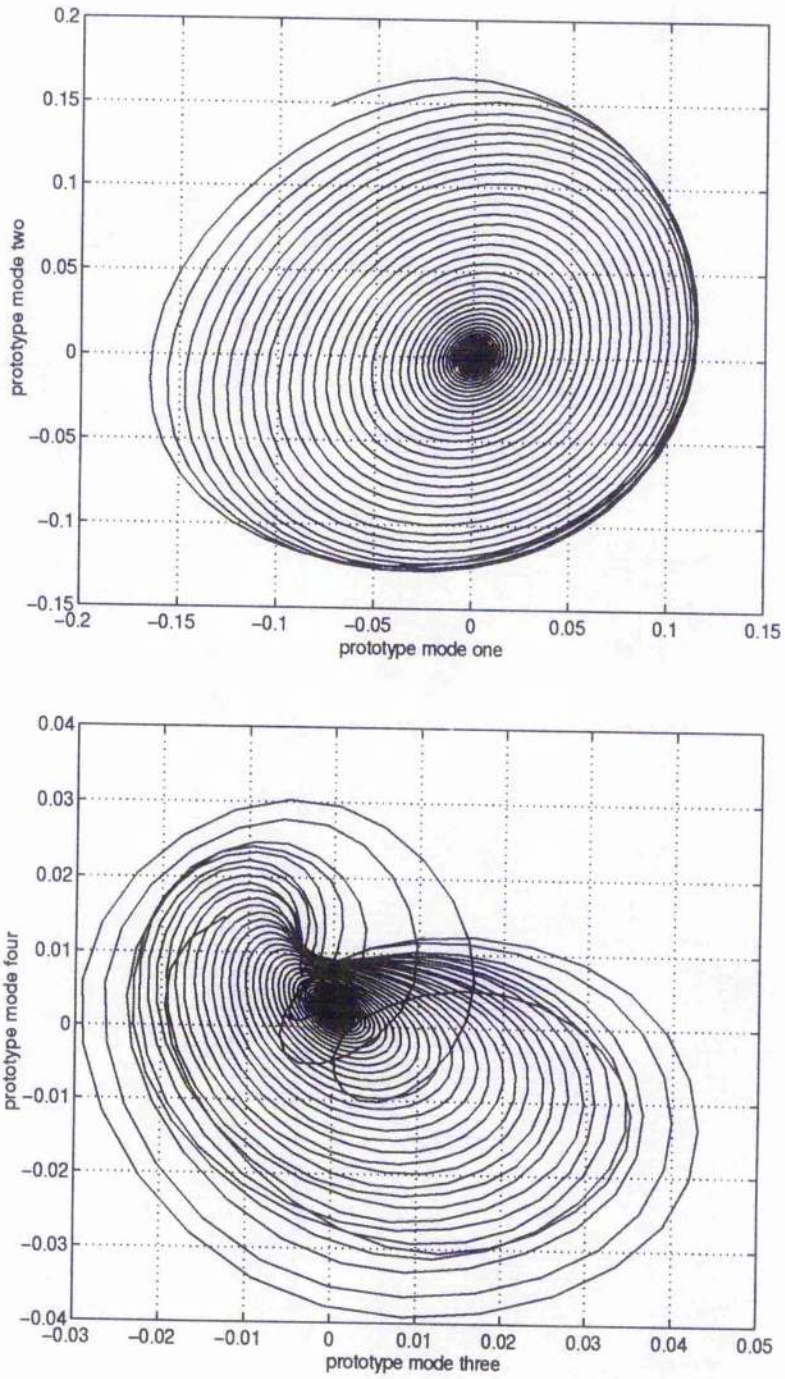


Figure 4.49: Phase portraits of prototype flow during a control run

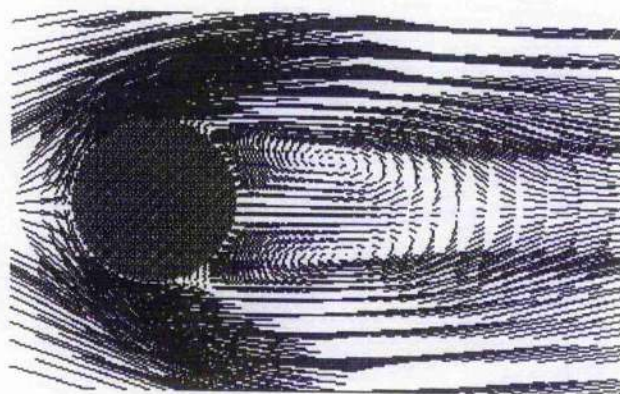


Figure 4.50: Velocity vectors of prototype flow after successful suppression of oscillations

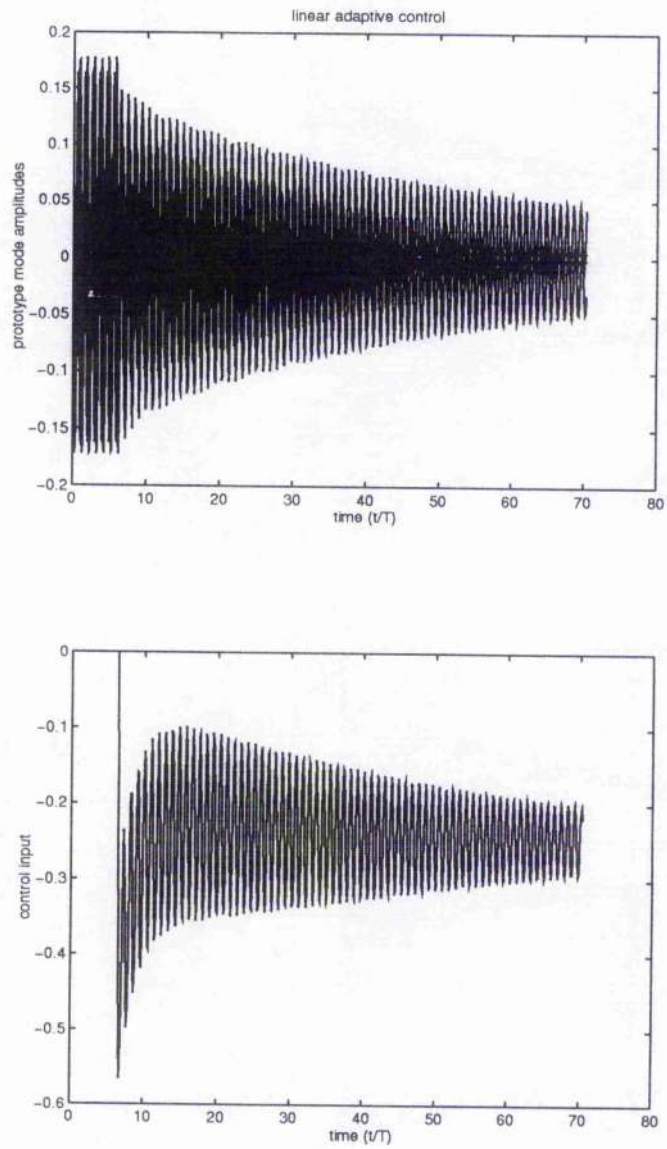


Figure 4.51: Linear adaptive control strategy

Chapter 5

Conclusions and Future Work

5.1 Conclusions

Active control of self-excited wake oscillations that are the result of global instability is not, in general, possible via single sensor linear feedback. The inability of single sensor feedback to control such absolutely unstable wakes is exemplified by numerical and experimental results of single sensor control schemes: oscillations may be stabilized at the sensor location but exacerbated elsewhere by the destabilization of further global modes. Typically, a linear stability analysis of the mean wake flow predicts the existence of multiple global modes, with closely spaced frequencies—for unforced wake flows the most unstable mode saturates to the von Kármán vortex street. The single sensor feedback control input necessary to stabilize the most unstable global mode is, in general, enough to destabilize the next most unstable mode—the oscillations at various points in the wake may not be the result of a single global mode and are therefore not connected by a simple phase shift, so single sensor control cannot stabilize all of the global modes. Multiple sensor control of such absolutely unstable flows is appropriate. The temporal behaviour of the natural and forced oscillations of absolutely unstable wakes is non-linear. Therefore, non-linear control of such flows is more suitable than linear control. However, a

non-linear control strategy based on the feedback of multiple (spatially distributed) measurements of the oscillating wake would be complex and computationally slow. It is reasonable to assert that a non-linear control strategy which is based on a low-dimensional description of the flow features would be simpler and therefore computationally feasible.

Inertial forms of the Navier-Stokes equations are appropriate for wake flows with suitable boundary conditions. Even when the analytic form of an inertial manifold is not known, approximate low-dimensional descriptions of wake flows often furnish reasonable predictions of the flow dynamics. Approximate, low-dimensional inertial forms of the flow equations for forced, non-stationary flow are valid as long as some mild restrictions are placed on the type and character of the forcing. The validity of low-dimensional descriptions of forced non-stationary wake flows is also suggested by experimental evidence. Given that a low-dimensional description of the spatio-temporal dynamics of a forced wake flow is appropriate, a simple characterization method, such as proper orthogonal decomposition, can be used to select a low-dimensional subspace which encapsulates a local region of the inertial manifold of the flow. Proper orthogonal decomposition provides an efficient means of characterizing the large scale spatial structures of the flow by a finite set of orthogonal modes. Modifications to the flow boundary conditions and non-stationary flow features, caused by the addition of a control, are accounted for by decomposition of a correlation matrix which is the average of a set of distinct correlations developed from flow transients during different forcing regimes. The set of sub-optimal POD modes developed from the non-stationary data is able to provide a succinct description of the spatial features occurring in wake flow oscillations in the presence of a control input. The finite description of the flow features with POD modes is of use in a non-linear wake control strategy.

Classically, a dynamical model of the POD mode amplitudes is determined via a Galerkin approximation— this type of dynamical model is inappropriate for control

purposes because there is no easy method for the rational integration of control inputs to the Galerkin model. An empirical method of predicting the mode amplitudes, from an initial control input and mode condition, is able to mimic the response of the wake to external perturbation. The dynamics of modes calculated by Galerkin approximation assumes a flat, linear inertial manifold; whereas the empirical prediction makes no assumptions about the geometry of the manifold.

Neural networks are readily applicable to systems where the analytical determination of the system model is difficult or impractical. A non-linear neural network, exposed to appropriate experimental data sets of control input and mode amplitude histories can be trained to emulate the required input-output relationship between a control and the wake (represented by the POD mode amplitudes). The non-linear prediction of the POD mode states can be used in a robust neural network control scheme, which takes advantage of the neural prediction of the POD dynamics. Training of an adaptive neural network controller is only possible because the one-step flow dynamics are predicted by another neural network.

The control strategy used for self-excited, oscillating wakes provides a non-linear control which is a function of the overall wake oscillations as detected by the oscillation of a finite number of POD modes. The utility of the control scheme is shown by control of a non linear, spatially complex prototype wake flow. The non-linear control is robust to external perturbation. The time history of the control, which suppresses the wake oscillations, is significantly non-linear in its early stages, when the amplitudes of wake oscillation are high. The non-linear controller thus performs better than a similar linear controller. The control scheme, which is based on POD modes (and therefore contains information about oscillations throughout the wake), is also seen to be, in general, superior to controllers based on single point measurements of the prototype flow.

Active control of a prototype wake flow is demonstrated. The demonstration of successful control of the prototype wake is useful because the control algorithm

is tested quickly and controller parameters such as network size and learning rate, activation function and time delay etc. are studied easily. Although a full simulation is preferable for accuracy, the large computational cost of time-forcing the numerical wake flow precludes initial testing of the controller parameters. The prototype wake contains some of the stability features of the actual cylinder wake flow and exhibits some spatial complexity. Hence, only minor changes in the control strategy are anticipated before application of the controller to a full numerical simulation.

5.2 Recommendations for Future Work

The feasibility of the non-linear POD mode control strategy for self-excited wake flows has been tested on a prototype wake flow that models the non-linear growth of instability and the behaviour of spatial structures seen during natural shedding oscillations and qualitatively models the response of the flow to external forcing. The model used for testing the construction and operation of the controller is, however, only an approximation of the full Navier-Stokes equations with forcing: further testing, which is based on a more accurate flow, is necessary. The controller developed for the prototype is expected to need only minor modification for application to a higher order CFD simulation. The advantage of further testing of the controller on a numerical CFD model (rather than an experimental wake) is that the whole velocity field (and hence all of the quantities required for feedback) are available. It is therefore expected that immediate further research will concentrate on application of the control strategy to higher order numerical simulations. Also, because the CFD model and controller operate on virtual, computer time there are no difficulties involved in the speed of controller signal processing, or computation, or controller activation--- all of which may pose problems in an experiment (the use of neural networks to perform controller computations, however, guarantees that the controller will operate quite quickly). Finally, future research may undertake to control a real

flow in an experiment.

Experimental implementation of the control strategy is not straightforward. Apart from determination of a suitable control device an experimental flow presents other difficulties—the flow would be affected adversely by a large number of spatially distributed probes so the flow field measurement should be non-intrusive. Future research may therefore involve particle image velocimetry or simple grey scale characterization of smoke flow patterns in a wake seeded with smoke (because of the empirical emulation of the POD mode dynamics the POD modes do not have to be of velocity).

It is also important to determine what constitutes a valid characterization ensemble for a time-forced experimental flow (ie. how many sub-optimal POD modes are required). Performing experimental characterizations of higher Reynolds number, turbulent wakes is important as most experimental wake flows are turbulent. The POD modes of turbulent wakes have a more widespread energy distribution than those of laminar wakes and hence more modes are necessary for adequate characterization of turbulent flows.

For successful implementation of the controller in either a higher order simulation or in an experimental flow a suitable control actuation device has to be constructed. The control input must be such that the mean flow is not significantly modified by application of the control input and that the control produces useful transients and flow structures (for example, the control must be able to excite sub-critical vortex shedding). Examples of control devices which satisfy all of the criteria for stabilization of the global instability modes are (amongst others) acoustic excitation of the near wake and small amplitude lateral vibration of the body.

Appendix A

Identification of the Prototype Wake Model

A.1 Galerkin Approximation of the Navier-Stokes Equations

The incompressible wake flow can be represented by a finite set of orthogonal spatial POD modes. Evolution equations for the mode amplitudes can be developed via a Galerkin approximation of the Navier-Stokes equations: the inner product of each mode is taken in turn with the residual of the Navier-Stokes equations (in which the velocity field is approximated by the mode expansion). The Galerkin approximation produces an autonomous differential equation for each mode amplitude. The approximation of the Navier-Stokes equations (with an added source term) by the truncated velocity field expansion afforded by the M POD modes is

$$\frac{\partial \mathbf{V}_M}{\partial t} = -(\mathbf{V}_M \cdot \nabla) \mathbf{V}_M - \nabla \Pi + \nu \nabla^2 \mathbf{V}_M + \mathbf{F} \quad (A.1)$$

The truncated velocity field is $\mathbf{V}_M = \bar{\mathbf{V}} + \mathbf{V}'$, where $\mathbf{V}' = \sum_{i=1}^M A_i \boldsymbol{\psi}_i$ and where \mathbf{F} is a source term. Substitution of the finite velocity field approximation into the

Navier-Stokes equations results in

$$\begin{aligned} \psi_i \frac{dA_i}{dt} + [(\bar{\mathbf{V}} \cdot \nabla) \bar{\mathbf{V}} + A_i (\psi_i \cdot \nabla) \bar{\mathbf{V}} + A_i (\bar{\mathbf{V}} \cdot \nabla) \psi_i + A_i A_j (\psi_i \cdot \nabla) \psi_j] \\ + \nabla \Pi - \nu \nabla^2 (\bar{\mathbf{V}} + A_i \psi_i) = \mathbf{F} \end{aligned}$$

$$i, j = 1, \dots, M \quad (A.2)$$

with implied summation over i and j . The inner product of each mode with equation (A.2) results in,

$$\begin{aligned} \left(\psi_k, \psi_i \frac{dA_i}{dt} \right) + \left(\psi_k, (\bar{\mathbf{V}} \cdot \nabla) \bar{\mathbf{V}} \right) + \left(\psi_k, [(\psi_i \cdot \nabla) \bar{\mathbf{V}} + (\bar{\mathbf{V}} \cdot \nabla) \psi_i] A_i \right) \\ + \left(\psi_k, (\psi_i \cdot \nabla) \psi_j A_i A_j \right) + \left(\psi_k, \nabla \Pi \right) - \left(\nu \psi_k, (\nabla^2 \bar{\mathbf{V}} + \nabla^2 \psi_i A_i) \right) = (\psi \cdot \mathbf{F}) \end{aligned}$$

$$i, j, k = 1, \dots, M \quad (A.3)$$

which becomes

$$\frac{dA_k}{dt} = \gamma_0^k + \gamma_{1i}^k A_i + \gamma_{2ij}^k A_i A_j + \nu (\gamma_3^k + \gamma_{4i}^k A_i) + \gamma_5^k + (\psi \cdot \mathbf{F}) \quad i, j, k = 1, \dots, M \quad (A.4)$$

for each mode k , where there is implied summation over i and j . The coefficients in A.3 represent the various internal inner products of A.3. The source term can be ignored for unforced flows $(\psi \cdot \mathbf{F}) = 0$.

The pressure term, $(\psi_k, \nabla \Pi)$ which contributes to γ_5^k , can be simplified using Green's first identity [39],

$$\int_{\Omega} \psi_k \cdot \nabla \Pi = \int_{\Omega} (\nabla \cdot \psi_k) \Pi - \int_{\Gamma} \Pi (\mathbf{n} \cdot \psi_k) \quad (A.5)$$

The first term of the RHS of A.5 is zero due to the incompressibility of the POD modes. The second term has a contribution from the pressure and from the velocity gradient: the pressure is zero at the outlet; while at the outflow and side walls, the POD modes are zero (because of the CFD boundary conditions). Therefore, there is no contribution to the Galerkin model from the pressure or velocity gradient terms (this is only true because the whole velocity field is considered [39]). Coefficient γ_5^k is thus zero.

Calculation of the vorticities of the mean flow and of the vorticities of each of the POD modes is implicit in the determination of the other coefficients in the Galerkin model. Coefficients γ_0 depend on the vorticity of the mean flow ($\nabla \times \bar{\mathbf{V}}$); coefficients γ_2 depend on the vorticities of each of the POD modes ($\nabla \times \psi_i$); and coefficients γ_1 depend on a combination of the vorticities of the modes and of the mean flow. Coefficients γ_3 and γ_4 depend on the Laplacian of the mean flow and each of the modes respectively. Determination of the first order spatial derivatives, inherent in the vorticity calculations, and determination of the second order spatial derivatives, inherent in the Laplacian terms, is prone to error: the modes are generated from an irregular, discrete grid and are therefore not directly amenable for numerical differentiation. The Laplacian terms are especially prone to numerical error— however, the viscosity of the flow is very small and so the Laplacian terms are much smaller than the other model coefficients and can be neglected. Neglecting the Laplacian terms introduces some small errors to the Galerkin approximation, but avoids the large errors inherent in the double spatial differentiation of the spatially discrete modes and mean flow vectors. The vorticities of the modes and mean flow can be estimated by fitting bi-cubic spline surfaces to the modes and mean flow and then differentiating the bi-cubic spline. The fitting process, however, still introduces significant numerical errors in the model identification; especially when the modes are spiky. A Galerkin model, which was developed using bi-cubic spline differentiation of the modes and the mean flow, failed to predict the long term behaviour of the mode amplitudes accurately. The direct use of Galerkin approximation for discretely measured flows is therefore limited.

A.2 Least Squares Identification of the Reduced Order Model

The functional form of the Galerkin model is known: the model is, at most, a quadratic polynomial of the retained mode amplitudes. The model can be re-expressed in a simpler form;

$$\frac{dA_k}{dt} = c_0^k + c_{1,i}^k A_i + c_{2,i,j}^k A_i A_j \quad (A.6)$$

for each of the M retained modes, with implied summation over i and j . The model is arranged so that there are no repeated coefficients. The coefficients remain to be calculated either by the inner products of the Galerkin approximation, with their associated numerical differentiation, or by some other means. There are $Q = 1 + 2M + \frac{1}{2}M(M - 1)$ unknown coefficients in the model. The unknown coefficients can be estimated empirically, without recourse to numerical differentiation. The flow is measured at a sequence of time-points, and the mode amplitudes are calculated using the simple inner product (3.25). The measured data forms M times series for each of the mode amplitudes. Because low, energy modes and their associated noise are neglected in the POD expansion, the mode amplitude time series are generally smooth and noise free. The modal decomposition *acts as a noise filter*. A cubic spline is easily fitted to the smooth mode amplitude series and the time-derivatives of the mode amplitudes are easily estimated with little error. A knowledge of the mode amplitudes (measured from the flow) and the mode amplitude time derivatives at each time point allows transformation of equation (A.6) into an algebraic equation for the unknown coefficients of each mode amplitude equation.

$$\mathbf{d}_k = \mathbf{S}\mathbf{c}_k \quad (A.7)$$

where the vectors,

$$\mathbf{d}_k = \begin{bmatrix} \frac{dA_k(t_1)}{dt} \\ \frac{dA_k(t_2)}{dt} \\ \vdots \\ \frac{dA_k(t_m)}{dt} \end{bmatrix} \quad (\text{A.8})$$

$$\mathbf{c}_k = \begin{bmatrix} c_0^k \\ c_{11}^k \\ c_{12}^k \\ \vdots \\ c_{1M}^k \\ c_{211}^k \\ c_{212}^k \\ \vdots \\ c_{2MM}^k \end{bmatrix} = \begin{bmatrix} C_1 \\ C_2 \\ \vdots \\ C_Q \end{bmatrix} \quad (\text{A.9})$$

and where the matrix,

$$\mathbf{S} = \begin{bmatrix} 1 & A_1(t_1) & A_2(t_1) & \cdots & A_M(t_1) & A_1(t_1)A_1(t_1) & \cdots & A_M(t_1)A_M(t_1) \\ 1 & A_1(t_2) & A_2(t_2) & \cdots & A_M(t_2) & A_1(t_2)A_1(t_2) & \cdots & A_M(t_2)A_M(t_2) \\ \vdots & \vdots & \vdots & \ddots & \vdots & \vdots & \ddots & \vdots \\ 1 & A_1(t_m) & A_2(t_m) & \cdots & A_M(t_m) & A_1(t_m)A_1(t_m) & \cdots & A_M(t_m)A_M(t_m) \end{bmatrix} \quad (\text{A.10})$$

Equation (A.7) thus represents a system of m equations in $Q = 1 + 2M + \frac{1}{2}M(M-1)$ unknowns. The number of equations is selected to be more than the number of coefficients so that a large enough region of the attractor is visited and hence all of the model coefficients can be determined. The equality of (A.7) will not hold because of measurement noise and because the system is over-determined. The system is therefore best solved by least squares minimization of the error with respect to the coefficients, C_i ,

$$e^2(C_i) = \frac{1}{M} \sum_{m=1}^M \left(d_m^k - \sum_{i=1}^Q s_{mi} C_i \right)^2 \quad (\text{A.11})$$

where s_{ij} is the i, j 'th element of \mathbf{S} . Transients of a dynamic system contain much more information about the underlying dynamical model than post transients or steady states. In general, a large collection of transient data is necessary for the resolution of all of the coefficients of the unknown model [10]. It is difficult to obtain all of the model coefficients by least squares minimization of (A.11) if the transient part of the considered time series is small, because the Gram matrix $\mathbf{S}^T \mathbf{S}$ becomes nearly singular. Models derived purely from post-transient time series often result in unstable limit cycles [10]. Therefore, a weighting function is introduced to the mode time series and derivative data such that transient points are given high importance, whereas post-transients are given less importance in the least squares minimization. A time point is considered transient if a measure of the distance between the mode amplitudes, at that time point, and the limit cycle mode amplitudes is greater than some finite value. The distance (in M dimensional space) between the measured mode amplitudes at each time point and the limit cycle is calculated. Every time point where this distance is greater than a small error value is considered transient. Positive weights are then introduced to the least squares minimization [10],

$$e_w^2(C_i^k) = \frac{1}{M} \sum_{m=1}^M w_m \left(d_m^k - \sum_{i=1}^Q s_{mi} C_i^k \right)^2 \quad (\text{A.12})$$

with

$$w_M = 1 + (w_{lc} - 1) \exp \left(1 - \frac{r_M^2}{e^2} \right) \quad (\text{A.13})$$

where r_M is the distance to the limit cycle of the state at time t_M , e is the minimum distance to be labelled transient, and w_{lc} is the weight given to transient points, $w_{lc} = N_t/N_{lc}$. N_t and N_{lc} are the number of transient points and number of points on the limit cycle respectively. This weighting function results in a similar importance of the transient part of the time series and the non-transient part. Minimization of the error in (A.13) requires least squares solution of

$$\mathbf{S}_w^T \mathbf{S}_w \mathbf{C} = \mathbf{S}_w^T \mathbf{d}_w \quad (\text{A.14})$$

for each mode, where $s_{i,w} = \sqrt{w_i} s_{ij}$ and $d_{j,w} = \sqrt{w_j} d_j$.

The least squares solution of (A.14) is badly scaled because the maxima of A_1 and $A_2 \gg A_3$ and $A_4 \gg \dots A_M$. Matrix \mathbf{S} therefore has elements of widely differing magnitude. Accordingly, the columns of \mathbf{S} are further weighted so as to have approximately equal magnitudes. As a result the smaller modes, together with their associated measurement noise, are multiplied by large numbers—this magnification means that the columns in \mathbf{S} representing the small modes are disproportionately noisy. The least squares method is therefore best suited to problems when only a few modes are considered. Also, the more modes retained in the approximation, the more coefficients, and therefore more transients, are needed for the solution [10].

To avoid adding further modes to the model it is reasonable to include some higher order terms (for example cubic terms) in the quadratic model— the modes corresponding to small spatial scales are approximate algebraic functions of the large scales. Terms higher than quadratics may therefore appear in a *non-linear* Galerkin model. It is known that a cubic Landau equation is capable of capturing the temporal growth of the instability, the addition of cubic terms therefore improves the model when only a few modes are available. The form of the model with added cubic terms is, for each mode k ,

$$\frac{dA_k}{dt} = c_0^k + c_{1,i}^k A_i + c_{2,i,j}^k A_i A_j + c_{3,i,j,l}^k A_i A_j A_l \quad i, j, k, l = 1, \dots, M \quad (\text{A.15})$$

with implied summation over i, j and l .

The numerical values of the coefficients of the complete, four mode prototype model used in Chapter Four are,

$$\begin{aligned} \frac{dA_1}{dt} = & -9.8797771e-08 + 6.4667931e-03A_1 \\ & + 1.4467036e-01A_2 + 2.9163621e-06A_1A_1 \\ & + 1.3516793e-05A_1A_2 - 9.1836959e-07A_2A_2 \\ & - 1.8453033e-01A_1A_1A_1 - 8.1531231e-03A_1A_1A_2 \end{aligned}$$

APPENDIX A. IDENTIFICATION OF THE PROTOTYPE WAKE MODEL 161

$$\begin{aligned}
 & -2.0695105e - 01A_1A_2A_2 - 7.3155167e - 03A_2A_2A_2 \\
 & +5.18359463e - 02A_3 - 2.58162018e - 02A_4 \\
 & -2.67112058e - 02A_1A_3 - 8.70818833e - 02A_1A_4 \\
 & -8.42083454e - 02A_2A_3 + 1.57876233e - 02A_2A_4 \\
 & +1.26628945e - 02A_3A_3 + 2.42933636e - 02A_3A_4 \\
 & +1.58450628e - 02A_4A_4 + 9.998e - 03f_a
 \end{aligned}$$

(A.16)

$$\begin{aligned}
 \frac{dA_2}{dt} = & 3.1562296e - 07 - 1.2929619e - 01A_1 \\
 & +6.4664067e - 03A_2 - 1.1359681e - 05A_1A_1 \\
 & +1.1564135e - 05A_1A_2 - 8.0340231e - 06A_2A_2 \\
 & +5.7244511e - 03A_1A_1A_1 - 1.8504683e - 01A_1A_1A_2 \\
 & +7.8211773e - 03A_1A_2A_2 - 2.0645473e - 01A_2A_2A_2 \\
 & +6.02492351e - 03A_3 + 3.63752811e - 02A_4 \\
 & +5.86899819e - 02A_1A_3 + 3.70566031e - 02A_1A_4 \\
 & +2.42364347e - 02A_2A_3 - 9.81767262e - 02A_2A_4 \\
 & -7.09051882e - 03A_3A_3 - 1.29932356e - 02A_3A_4 \\
 & +5.18047642e - 03A_4A_4 + 9.866e - 03f_a
 \end{aligned}$$

(A.17)

$$\begin{aligned}
 \frac{dA_3}{dt} = & 7.85160994e - 04 - 8.40895701e - 04A_1 \\
 & -5.52677989e - 06A_2 - 3.47421084e - 02A_3 \\
 & -3.15618142e - 01A_4 + 2.29766347e - 02A_1A_1 \\
 & +6.70135725e - 04A_1A_2 + 2.52875366e - 03A_1A_3 \\
 & -3.00029222e - 02A_1A_4 - 2.42665864e - 02A_2A_2
 \end{aligned}$$

$$\begin{aligned}
& -8.54086958e - 03A_2A_3 - 3.55181276e - 02A_2A_4 \\
& -9.76471889e - 03A_3A_3 - 3.76874519e - 02A_3A_4 \\
& +3.24691326e - 03A_4A_4 + 6.0577e - 03f_c
\end{aligned}$$

(A.18)

$$\begin{aligned}
\frac{dA_4}{dt} = & 5.53803810e - 05 + 2.65916998e - 04A_1 \\
& +7.16616167e - 04A_2 + 2.43268601e - 01A_3 \\
& -2.92261771e - 02A_4 - 5.46440118e - 03A_1A_1 \\
& -3.81723387e - 02A_1A_2 + 9.67050500e - 03A_1A_3 \\
& +2.17240367e - 02A_1A_4 - 3.27980557e - 03A_2A_2 \\
& +5.05461587e - 02A_2A_3 + 3.35363453e - 03A_2A_4 \\
& +2.94750410e - 02A_3A_3 - 1.51851997e - 02A_3A_4 \\
& -8.30075377e - 03A_4A_4 + 6.632e - 03f_c
\end{aligned}$$

(A.19)

Bibliography

- [1] P. Huerre and P. A. Monkewitz. Local and global instabilities in spatially developing flows. *Annu. Rev. Fluid Mech.*, pages 473–537, 1990.
- [2] G. E. Karniadakis and G. S. Triantafyllou. Frequency selection and asymptotic states in laminar wakes. *Journal of Fluid Mechanics*, pages 441–469, 1989.
- [3] J. M. Chomaz, P. Huerre, and L. G. Redekopp. Bifurcations to local and global modes in spatially developing flows. *Physical Review Letters*, 60(1):25–28, 1988.
- [4] P. A. Monkewitz. Feedback control of global oscillations in fluid systems. *AIAA 89-0991*, 1989.
- [5] P. A. Monkewitz. The absolute and convective nature of instability in two-dimensional wakes at low Re. *Physics of Fluids*, 31(5):999, May 1988.
- [6] M. Schumm, E. Berger, and P. A. Monkewitz. Self-excited oscillations in the wake of two-dimensional bluff bodies and their control. *Journal of Fluid Mechanics*, 271:17–53, 1994.
- [7] K. Roussopoulos. Feedback control of vortex shedding at low Reynolds numbers. *Journal of Fluid Mechanics*, pages 267–296, 1993.
- [8] B. R. Noak and H. Eckelmann. A global stability analysis of the steady and periodic cylinder wake. *Journal of Fluid Mechanics*, 270:297–330, 1994.

- [9] E. Detemple-Laake and H. Eckelmann. Phenomenology of Karman vortex streets in oscillatory flow. *Experiments in Fluids*, pages 217–227, 1989.
- [10] B. R. Noack, F. Ohle, and H. Eckelmann. Construction and analysis of differential equations from experimental time series of oscillatory systems. *Physica D*, 56:389–405, 1992.
- [11] F. Ohle and H. Eckelmann. Modelling of a von Karman vortex street at low Reynolds numbers. *Physics of Fluids A*, 4(8):1707–1714, August 1992.
- [12] R. W. Metcalfe, C. J. Rutland, J. H. Duncan, and J. J. Riley. Numerical simulations of active stabilization of laminar boundary layers. *AIAA J*, pages 1494–1501, 1986.
- [13] E. Laurien and L. Kleiser. Numerical simulation of boundary layer transition and transition control. *Journal of Fluids and Structures*, pages 403–440, 1989.
- [14] S. A. Jacobson and W. C. Reynolds. Active control of boundary layer wall shear stress using self-learning neural networks. *AIAA 93-3272*, 1993.
- [15] R. W. Milling. Tollmein Schlichting wave cancellation. *Physics of Fluids*, pages 979–981, 1981.
- [16] H. W. Leipmann and D. M. Nosenchuck. Active control of laminar-turbulent transition. *Journal of Fluid Mechanics*, pages 201–204, 1982.
- [17] P. J. Strykowski and K. R. Sreenivasan. The control of transitional flows. *AIAA 85-0559*, 1985.
- [18] San-Yih Lin and Tsuen-Muh Wu. Flow control simulations around a circular cylinder by a finite volume scheme. *AIAA 93-3278*, 1993.

- [19] R. Gopalkrishnan, M. S. Triantafyllou, G. S. Triantafyllou, and D. Barret. Active vorticity control in a shear flow using a flapping foil. *Journal of Fluid Mechanics*, 274:1–21, 1994.
- [20] D. S. Park, D. M. Ladd, and E. W. Hendricks. Feedback control of von Karman vortex shedding behind a cylinder at low Reynolds numbers. *Journal of Fluid Mechanics*, 6(7):2390–2405, July 1994.
- [21] P. T. Tokumar and P. E. Dimotakis. Rotary oscillation control of a cylinder wake. *J. Fluid Mech.*, 224:77–90, 1991.
- [22] M. Lewit. Active control of dipole sound from cylinders. In *Proceedings DAGA 1992, Berlin Germany*, 1992.
- [23] D. J. Olinger and K. R. Sreenivasan. Non-linear dynamics in the wake of an oscillating cylinder. *Physical Review Letters*, 60(9):797–800, February 1988.
- [24] J. E. Ffowcs-Williams and B. C. Zhao. The active control of vortex shedding. *Journal of Fluids and Structures*, pages 115–122, 1989.
- [25] C. T. Shaw and G. P. King. Using cluster analysis to classify time series. *Physica D*, 58:288–298, 1992.
- [26] G. Lightbody, Q. H. Wu, and G. W. Irwin. Control applications for feedforward neural networks. In *Neural Networks for control and systems*. Peregrinus, 1992.
- [27] E. S. Titi. On approximate inertial manifolds to the Navier-Stokes equations. *Journal of Mathematical Analysis and Applications*, 149:540–557, 1990.
- [28] D. A. Jones and E. S. Titi. A remark on quasi-stationary approximate inertial manifolds for the Navier-Stokes equations. *SIAM Journal of Mathematical Analysis*, 25(3):894–914, May 1994.

- [29] D. S. Broomhead, R. Indik, A. C. Newell, and D. A. Rand. Local adaptive Galerkin bases for large dimension dynamical systems. *Nonlinearity*, pages 159–197, 1991.
- [30] C. Foias, G. R. Sell, and R. Temam. Inertial manifolds for non-linear evolutionary equations. *Journal of Differential Equations*, pages 309–353, 1988.
- [31] A. Glezer, Z. Kadioglu, and A. J. Pearlstein. Development of an extended proper orthogonal decomposition to a time periodically forced plane mixing layer. *Physics of Fluids A*, 1(8):1363–1373, August 1989.
- [32] J. L. Lumley. *Stochastic tools in turbulence*. Academic Press, 1970.
- [33] L. Sirovich. Turbulence and the dynamics of coherent structures. *Quarterly of Applied Mathematics*, XLV(3):561–590, October 1987.
- [34] L. Sirovich and M. Kirby. Low-dimensional procedure for the characterization of human faces. *J. Opt. Soc. Am. A*, 4(3):519–524, March 1987.
- [35] J. L. Lumley. Coherent structures in turbulence. In *Transition and turbulence*. Academic Press, 1981.
- [36] L. Sirovich, M. Kirby, and M. Winter. An eigenfunction approach to large scale transitional structures in jet flow. *Physics of Fluids A*, 2(2):127–135, February 1990.
- [37] G. Berkooz, P. Holmes, and J. L. Lumley. The proper orthogonal decomposition in the analysis of turbulent flows. *Annu. Rev. Fluid Mech.*, pages 539–575, 1993.
- [38] N. Aubrey, P. Holmes, J. L. Lumley, and E. Stone. The dynamics of coherent structures in the wall region of a turbulent boundary layer. *Journal of Fluid Mechanics*, pages 115–173, 1988.

- [39] A. E. Deane, I. G. Kevrekidis, G. E. Karniadakis, and S. A. Orszag. Low-dimensional models for complex geometry flows. *Physics of Fluids A*, 3(10):2337–2354, October 1991.
- [40] A. E. Deane and C. Mavriplis. Low-dimensional description of the dynamics in separated flow past thick aerofoils. *AIAA-91-1622-GP*, 1991.
- [41] D. H. Nguyen and B. Widrow. Neural networks for self-learning control systems. *IEEE Control Systems Magazine*, April 1990.
- [42] S. Haykin. *Neural networks: a comprehensive foundation*. Macmillan, 1994.
- [43] B. R. Noack and H. Eckelmann. On chaos on wakes. *Physica D*, 56:151–164, 1992.
- [44] D. S. Broomhead and G. P. King. On the qualitative analysis of experimental dynamical systems. In *Non-linear phenomena and chaos*. Adam Hilger, 1986.
- [45] J. M. T. Thompson and H. B. Stewart. *Nonlinear Dynamics and Chaos*. John Wiley, 1986.
- [46] L. Sirovich, B. W. Knight, and J. D. Rodriguez. Optimal low-dimensional dynamical approximations. *Quarterly of Applied Mathematics*, XLVIII(3), April 1990.
- [47] R. P. Lippmann. An introduction to computing with neural networks. *IEEE ASSP Magazine*, April 1987.
- [48] D. R. Hush and B. G. Horne. Progress in supervised neural networks. *IEEE Signal Processing Magazine*, January 1993.
- [49] Creare.x. *FLUENT v4.10 user guide*, 1991.
- [50] B. E. Eaton. Analysis of vortex shedding behind circular cylinders. *Journal of Fluid Mechanics*, 180(117), 1987.

- [51] S. W. Kim and T. J. Benson. Comparison of the SMAC,PISO and iterative time-advancing schemes for unsteady flows. *Journal of Computers in Fluids*, 21(3), 1992.
- [52] C. Taylor and K. Morgan. *Recent advances in numerical methods in fluids*. Pineridge Press, Swansea, 1980.
- [53] D. J. Tritton. The flow past a circular cylinder at low Reynolds number. *Journal of Fluid Mechanics*, 6, 1959.
- [54] D. J. Tritton. *Physical Fluid Dynamics*. Clarendon Press, Oxford, 1988.
- [55] C. A. Friehe. Vortex shedding from cylinders at low Reynolds numbers. *Journal of Fluid Mechanics*, 100, 1989.

